Technical Report

TR-04-24

Inspection of copper canisters for spent nuclear fuel by means of ultrasound

Phased arrays, ultrasonic imaging and nonlinear acoustics

Tadeusz Stepinski (editor)
Ping Wu and Erik Wennerström
Uppsala University, Signals and Systems,
Department of Technical Science

September 2004

Svensk Kärnbränslehantering AB
Swedish Nuclear Fuel
and Waste Management Co
Box 5864
SE-102 40 Stockholm Sweden
Tel 08-459 84 00
+46 8 459 84 00
Fax 08-661 57 19
+46 8 661 57 19

Inspection of copper canisters for spent nuclear fuel by means of ultrasound

Phased arrays, ultrasonic imaging and nonlinear acoustics

Tadeusz Stepinski (editor)
Ping Wu and Erik Wennerström
Uppsala University, Signals and Systems,
Department of Technical Science

September 2004

SKB Report 2004

Tadeusz Stepinski (editor) Ping Wu Erik Wennerström

September 28, 2004

Abstract

This report contains the research results concerning advanced ultrasound for the inspection of copper canisters for spent nuclear fuel obtained at Signals and Systems, Uppsala University in years 2003/2004.

After a short introduction a review of beamforming fundamentals required for proper understanding phased array operation is included. The factors that determine lateral resolution during ultrasonic imaging of flaws in solids are analyzed and results of simulations modelling contact inspection of copper are presented.

In the second chapter an improved synthetic aperture imaging (SAI) technique is introduced. The proposed SAI technique is characterized by an enhanced lateral resolution compared with the previously proposed extended synthetic aperture focusing technique (ESAFT). The enhancement of imaging performance is achieved due to more realistic assumption concerning the probability density function of scatterers in the region of interest. The proposed technique takes the form of a two-step algorithm using the result obtained in the first step as a prior for the second step.

Final chapter contains summary of our recent experimental and theoretical research on nonlinear ultrasonics of unbounded interfaces. A new theoretical model for rough interfaces is developed, and the experimental results from the copper specimens that mimic contact cracks of different types are presented. Derivation of the theory and selected measurement results are given in appendix.

Contents

Chapter 1

Introduction

1.1 Outline of the Report

Reliable detecting and sizing natural defects in EB and friction stir welds that will be used for sealing copper canisters for spent nuclear fuel requires applying advanced ultrasonic imaging techniques. In this report we are presenting our recent results concerning inspection of copper canisters for spent nuclear fuel by means of ultrasound.

Our research activity in this project in year 2003/2004 was split in four separate tasks:

- Resolution of phased arrays
- Synthetic aperture imaging
- Nonlinear ultrasonic NDE of copper welds, and
- NDE of grain size in copper

The first task, presented in Chapter 2 is an tutorial on ultrasonic phased arrays. After a short review of beamforming fundamentals required for proper understanding phased array operation we analyze factors that determine lateral resolution during ultrasonic imaging of flaws in solids. We consider such parameters as, array geometry, its center frequency and bandwidth, and the applied focusing laws. The analysis is performed using extensive simulations of imaging systems. The study is concluded with a set of practical rules aimed as an aid for operators performing imaging using phased arrays.

The second task, which is a continuation of our experimental and theoretical research concerning synthetic aperture imaging and its NDE applications is reported in Chapter 3. We propose an improved synthetic aperture imaging technique with increased lateral resolution compared with ESAFT that was proposed in our previous report. ESAFT is based on the assumption that probability density of the imaged targets (so called prior) is Gaussian, which is the simplest case for the analysis. The increase of performance is obtained due to more realistic assumption concerning the prior. The proposed technique results in a two-step algorithm using the result obtained in the first step as a prior for the second step. The algorithm has been developed using simulated data and verified on data acquired using our array system.

The third task, concerning nonlinear ultrasonic NDE of copper welds is reported in Chapter 4. Theoretical and experimental results on nonlinear ultrasonics of unbounded interfaces are presented. A theoretical model of rough interfaces is developed, and selected results of the experiments conducted on copper specimens that mimic contact cracks of different types are presented. Detailed derivation of the theory and selected measurement results are given in appendix.

The final task, concerned with nondestructive characterization of copper material used for canisters has not been completed and will be reported in our next report.

Chapter 2

Array Resolution

by Tadeusz Stepinski

2.1 Resolution of Phased Arrays

2.1.1 Introduction

Phased arrays are relatively new tool that has been introduced to NDE in the recent decennium. Recent developments of the ultrasonic phased array hardware for NDE have enabled a wide use of this technology in industrial applications. One of the most important advantages of phased arrays is their ability to modify beam patterns in an electronic way, that is, the capacity of electronic beam steering and focusing without moving the array or changing its physical components. This feature creates a considerable flexibility that accelerates inspecting parts with complex geometry and facilitates the use of UT in many practical applications.

Despite the unquestionable advantages, successful application of phased arrays requires more insight in the mechanism of waves propagation than the conventional ultrasound. Most of the references available in the field are concerned with medical applications of phased arrays, which means that they apply to liquid medium only. NDE deals with the detection of hard scatterers in solids and therefore it has different needs from those related to imaging soft scatterers in water.

In this report we will analyze factors that determine the lateral and temporal resolution during ultrasonic imaging of defects in solids using arrays. First, we preset a short review of beamforming fundamentals required for proper understanding phased array operation. In the second part, we explain the importance of different array parameters that determine spatial resolution. We will consider such parameters as, array geometry, its center frequency and bandwidth, and the applied focusing laws. The analysis will be performed using extensive simulations of both artificial and real arrays. Finally, we will formulate a set of practical rules that should help user to optimize imaging using phased arrays.

2.1.2 Beamforming

A beam is formed using an ultrasonic array by steering its beam pattern in a desired direction, thus enhancing this particular spatial direction and attenuating the other directions. An ultrasonic image of the region of interest defined in terms of range (time) and bearing (direction) can be then composed from different beams. Beamforming that is normally applied both in the transmission and reception modes, is the process of combining the outputs of a phased array in such a way as to achieve spatial selectivity. Modern beamforming process is typically implemented using digital processors and associated electronic hardware, resulting in low maintenance costs and high scan rates. Beamforming in the reception mode is a method of observing signals from a desired direction while attenuating the response of the array to signals from other directions. Beamforming can permit a multi-dimensional view of a medium using an appropriate array of sensors, and thus has many applications, including medicine, astronomy and military devices [1], [2], [3]. Below, we will present an introduction to time-domain beamforming using a simple 2-dimensional case as an illustration.

Let us consider the reception mode where the reflections from the objects located at the array's far field are received. This means that the distance from the array to the objects is large enough, so that the wave fronts reaching the targets are parallel to the array. Further, we assume that the received waves take the form of a sinusoidal modulated signal with spatial information inscribed by the reflections from the objects to be detected. The signal propagates through the medium with speed c as a plane wave of angular frequency ω and the associated wave number is $k = \omega/c$. Denote position of the individual element m as $\mathbf{r}_m$ and define the orientation of the plane wave using the directional (column) vector $\mathbf{u}$ (see Figure 2.1). Then the

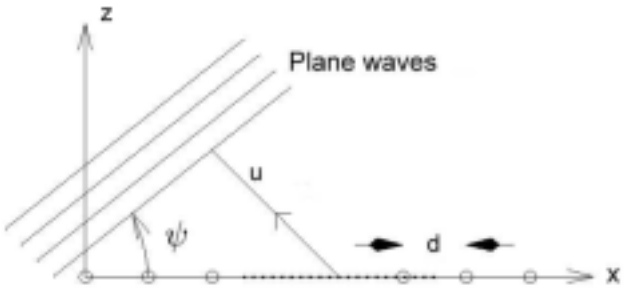

Figure 2.1: Linear array consisting of M elements separated with a distance d along x-axis receives plane waves incident with an angle ψ.

signal received at mth sensor is

$$x_m(t) = e^{j(\omega t + k\cdot \mathbf{r}_m \cdot \mathbf{u})} = x(t) \cdot e^{(jkr_m)} \quad \text{for } m = 0, \ldots, M\text{-}1 \tag{2.1}$$

where $x(t) = e^{j\omega t}$, and $r_m = \mathbf{r}_m^T \mathbf{u} = \sum_{i=0}^{M-1} r_i \cdot u_i$ is the projection of $\mathbf{r}_m$ on $\mathbf{u}$, which defines an additional relative distance that a wave coming from the direction $\mathbf{u}$ propagates to reach an array element located at $\mathbf{r}_m$.

If the outputs of M sensors in the array are summed the array will act as a spatial filter that enhances the direction normal to the array. In such case the array output *y(t)* will be described by the *beamforming equation* (see for [2] details), that is

$$y(t) = \mathbf{a} \cdot \mathbf{X}(t) = x(t) \cdot \mathbf{a} \cdot e^{jk\mathbf{r}} \tag{2.2}$$

where $\mathbf{a}$ denotes a window function, $\mathbf{X}$(t) denotes all sensor outputs, and $\mathbf{r}$ denotes respective phase delays of individual sensors, such that

$$\mathbf{a} = [a_0 \ldots a_{M-1}] \quad \mathbf{X}(t) = [x_0(t) \ldots x_{M-1}(t)]^T = x(t) \cdot e^{jk\cdot\mathbf{r}} \quad \mathbf{r} = [r_0 \ldots r_{M-1}]^T \tag{2.3}$$

The window function $\mathbf{a}$ defines apodization, i.e., gains applied to individual elements of the array in order to modify its beam pattern. The main function of the window function is suppressing side lobes that appear on both sides of the main lobe. This can be observed in Figure 2.2 where the beam patterns obtained for a rectangular window (no apodization) can be compared with those obtained for the apodization using Hamming window. The beam patterns presented in Figure 2.2 are calculated for the 16-, respective 32-element array with point-like elements spaced with $d = 1mm$ for a continuous wave (CW) with frequency 3MHz in copper (longitudinal wave velocity 4660m/s, $\lambda = 1.55mm$). Those arrays, referred to, respectively as $A32EL$ and $A32EL$ will be used below in examples illustrating the presented theory. From Figure 2.2 can be seen that apodization reduces side lobe level at the price of decreased resolution (broader main lobe).

2.1.3 Beam steering

Steering or spatial filtering in a particular direction, $\mathbf{u}_0$, is achieved by coherent summation of the array outputs, $\mathbf{X}(t)$, for this direction. This is achieved by introducing time delays varying linearly with element number so that a planar wave is sent in the desired direction. This leads to the *general beamforming equation*

$$y(t, \mathbf{u}_0) = x(t) \cdot \mathbf{a} \cdot e^{jk(\mathbf{r}-\mathbf{r}_0)} = x(t) \cdot b(\omega, \mathbf{u}_0) \tag{2.4}$$

where the *beam pattern*, $b(\omega, \mathbf{u}_0)$ is given by

$$b(\omega, \mathbf{u}_0) = \mathbf{a} \cdot e^{jk(\mathbf{r}-\mathbf{r}_0)} \tag{2.5}$$

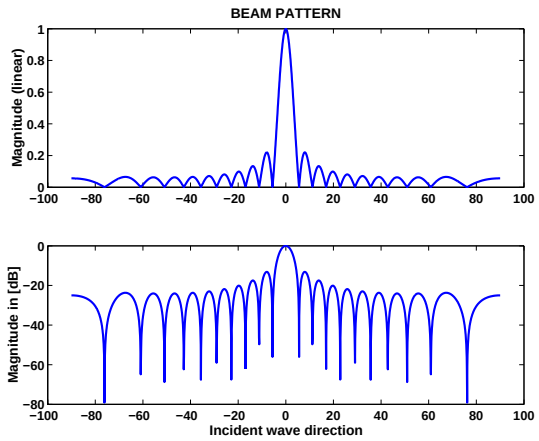

(a) 16 elements without apodization

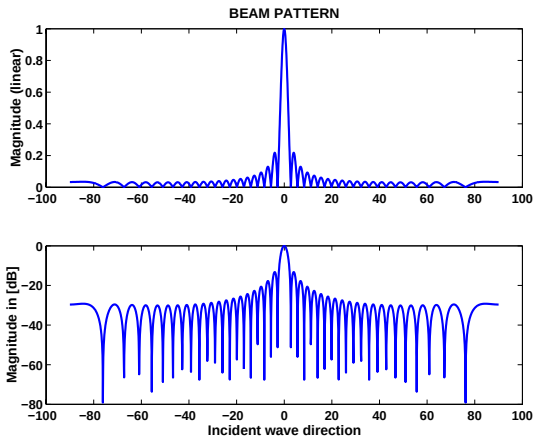

(b) 32 elements without apodization

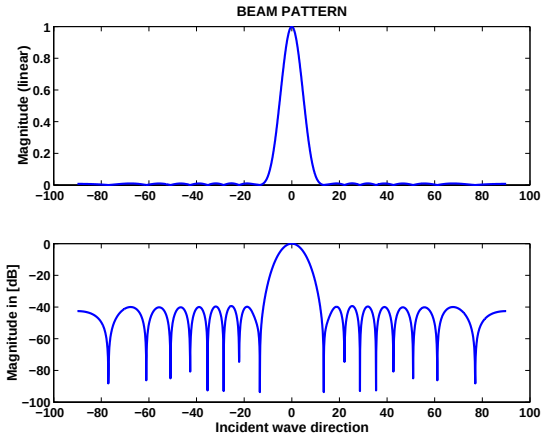

(c) 16 elements with apodization

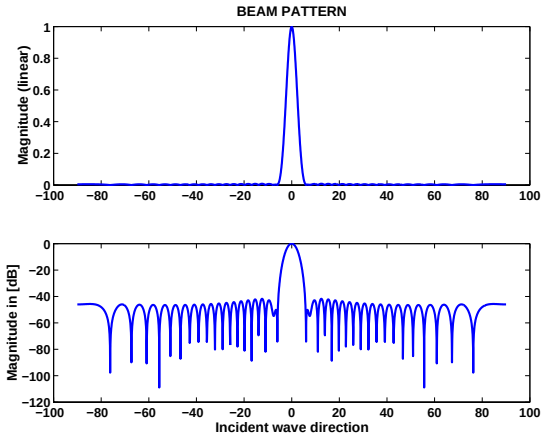

(d) 32 elements with apodization

Figure 2.2: Theoretical beam patterns in far field for ultrasonic arrays with respective, 16 and 32 elements in copper, respective with and without apodization

For a linear array consisting of M elements the beamforming equation takes the form

$$b(\omega, \psi_0) = \mathbf{a} \cdot e^{jkd \cdot \mathbf{m} \cdot \sin \psi_0} \tag{2.6}$$

where $\mathbf{m} = [0, 1, \ldots, M-1]^T$, d is element spacing (pitch), and ψ_0 denotes the desired bearing (steering direction). Beam steering is illustrated by the beam patterns presented in Figures 2.3

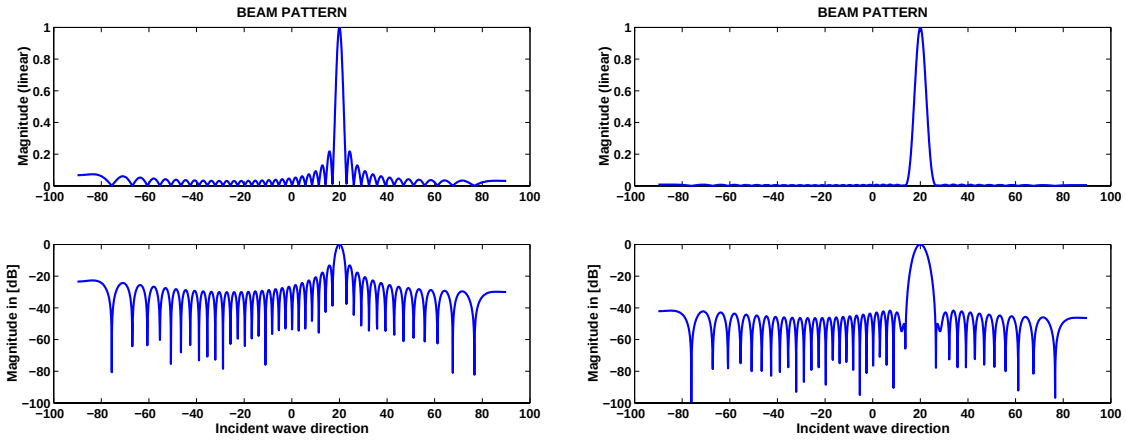

(a) Array without apodization

(b) Array with Hamming apodization

Figure 2.3: Theoretical beam patterns in far field for the 32-element ultrasonic array steered with 20° in copper, respective without and with apodization.

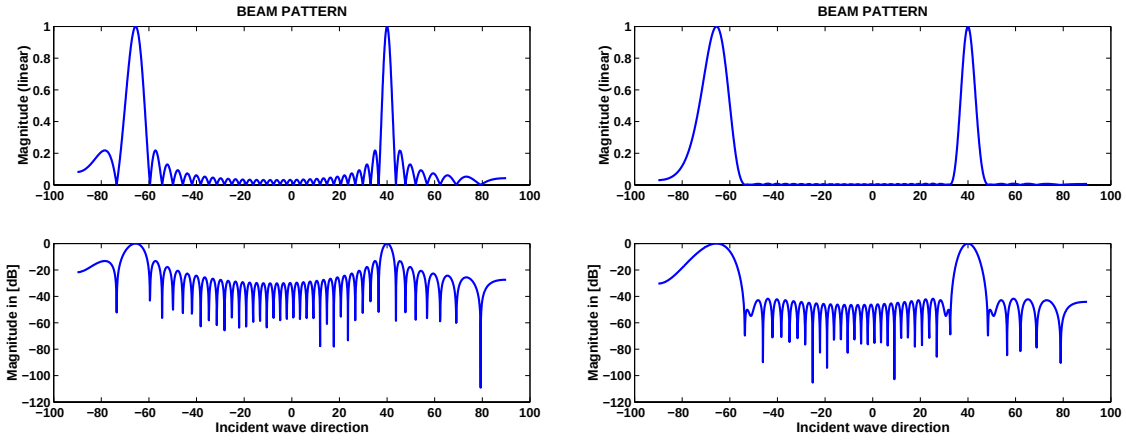

(a) Array without apodization

(b) Array with Hamming apodization

Figure 2.4: Theoretical beam patterns in far field for the 32-element ultrasonic array steered with 40° in copper, respective without and with apodization.

and 2.4 obtained for a 32-element array, respectively, without apodization and with apodization using Hamming window. The simulation was performed for CW with frequency 3MHz in copper for the array *A32EL*. From Figures 2.3 and 2.4 can be seen that apodization is essential for the steered beams since it substantially reduces the side lobe level. In Figure 2.4 an additional lobe appears at the left hand side, which is often encountered for a larger steering angles due to the discrete nature of phase arrays, this phenomenon will be discussed in more detail in Section 2.1.5.

2.1.4 Beam focusing

Focusing at a particular point at a distance f from the array is achieved by coherent summation of sensor outputs, $X(t)$, so that beams from all elements meet in phase at this point. This is achieved by introducing time delays compensating the elements distance to this point so that a cylindrical wave is sent in the desired direction. For focusing a linear array consisting of M elements in far field the beamforming equation becomes

$$b(\omega, \psi_0) \approx \mathbf{a} \cdot e^{jkd \cdot \mathbf{p}_m} \quad \text{where} \quad \mathbf{p}_m = \frac{d}{2f}[0, 1, \ldots, (M-1)^2] \tag{2.7}$$

Radiation emitted by the array *A32EL* focused at a distance of 60mm for 3MHz CW in copper is shown in Figure 2.5. Radiation pattern is presented at Figure 2.5a while the beam cross-sections are shown in Figures 2.5b and 2.5c. From Figure 2.5, it can be seen that the array's beam has a well pronounced maximum at the focal distance (60mm) in the direction 0°.

Simultaneous beamforming and focusing consists in superposing both time delays as it is illustrated in Fig. 2.6.

2.1.5 Spatial aliasing

Consider the un-steered beam with beam pattern defined by Eq. (2.5), it can be proven (see [4], [5] for details) that the magnitude of the beam pattern is given by

$$|b(\omega, \psi_0)| = \left| \frac{\sin(\pi\delta \cdot M \cdot \sin\psi)}{\sin(\pi\delta \cdot \psi)} \right| \quad \text{where} \quad \delta = \frac{df}{c} \tag{2.8}$$

For far field the angle ψ is small and we can use the approximation

$$|b(\omega, \psi_0)| \approx \left| \frac{\sin(\pi\delta \cdot M \cdot \psi)}{\sin(\pi\delta \cdot \psi)} \right| \tag{2.9}$$

Thus Eq. (2.9) attains a maximum when the denominator becomes zero, that is for

$$\pi\delta \cdot \psi = n\pi \quad \text{for} \quad n = 0, \pm 1, \pm 2, \ldots \tag{2.10}$$

This means that the beam pattern is periodic, since it has its maximum not only for $\psi = 0$ but also repeating peaks at $\psi = n/\delta$. The repeating peaks define so called *grating lobes* that appear due to the discrete nature of the array. This undesirable effect is known as *spatial aliasing*. Position of the grating lobes in space is defined by the relative separation δ, that is, for a wave with frequency f propagating in a medium characterized by the sound velocity c the array spacing d can be used to control position of the grating lobes.

Consider $\delta = 1/2$, that is the array spacing equal to half wavelength, $d = \lambda/2$, then the first grating lobes will appear at $\pm 90°$ which is also the maximum steering angle possible. Thus, the array separation $d = \lambda/2$ eliminates spatial aliasing and corresponds to the Nyquist frequency in signal processing [5], [1]. Spatial aliasing should be taken into account during array design, especially when the array is to be steered with larger angles (see Figure 2.7 illustrating aliasing problem). From Figure 2.7, it can be seen that increasing array spacing above $\lambda/2$ results in a grating lobe that appears at an undesired angle $< 90°$. Note that amplitude of this lobe cannot be attenuated by apodization.

2.1.6 Spatial resolution

Spatial resolution of an array is determined by the width of its main lobe given an accepted level of its side lobes. Consider Eq. (2.9), for small values of ψ it can be approximated by

$$|b(\omega, \psi_0)| \approx \left| \frac{\sin(\pi\delta \cdot M \cdot \psi)}{\pi\delta \cdot \psi} \right| \tag{2.11}$$

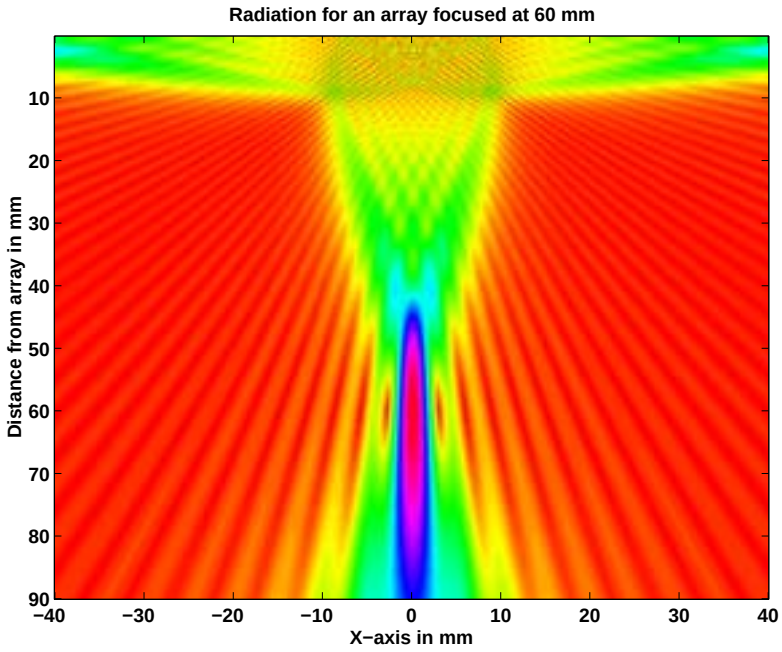

(a) Radiation pattern

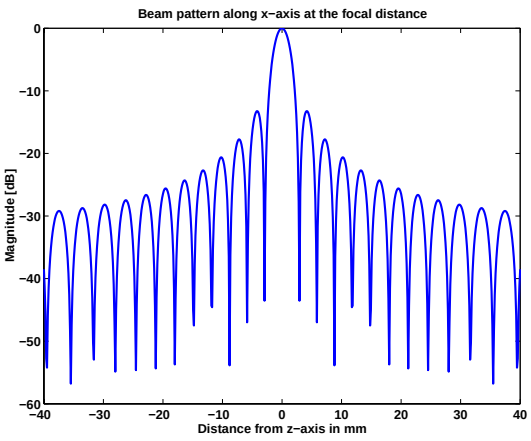

(b) Beam profile in dB

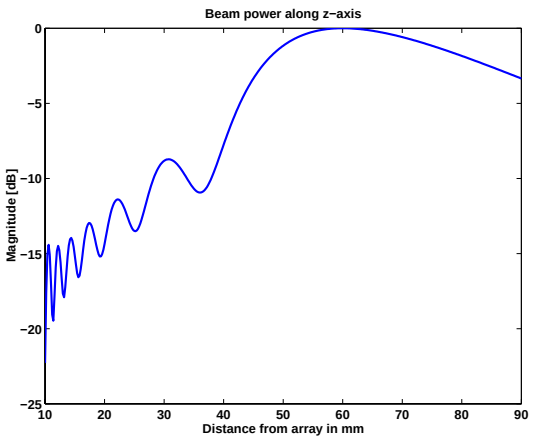

(c) Beam intensity on z-axis in dB

Figure 2.5: Radiation pattern, beam profile at focal distance, and beam intensity on axis for the array *A32EL* focused at 60mm in copper

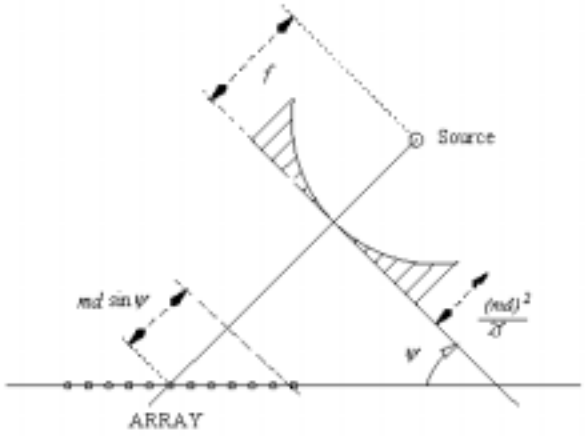

Figure 2.6: Steering and focusing of a linear array.

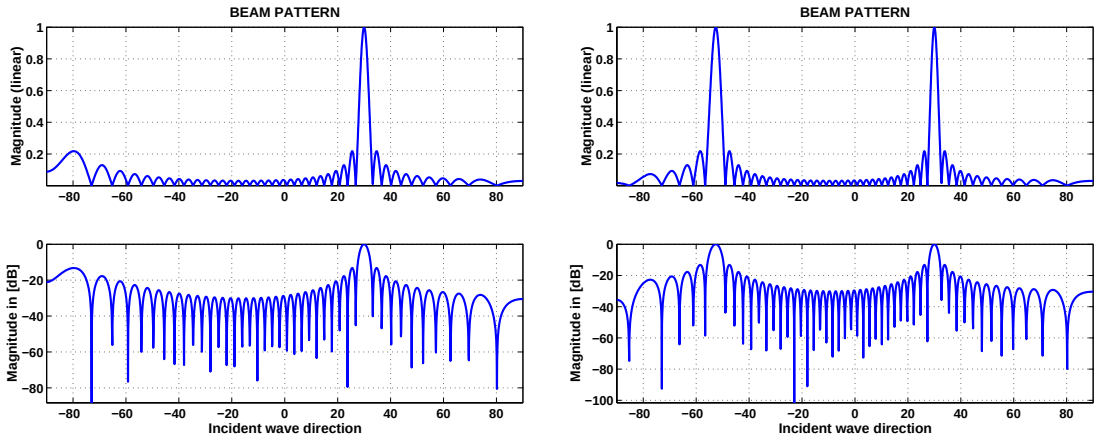

(a) 1mm pitch

(b) 1.2mm pitch

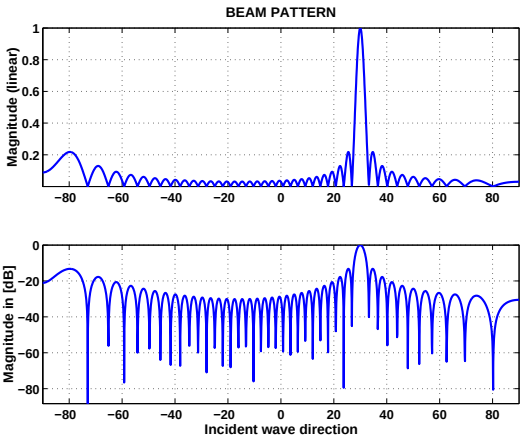

(c) 1mm pitch with apodization

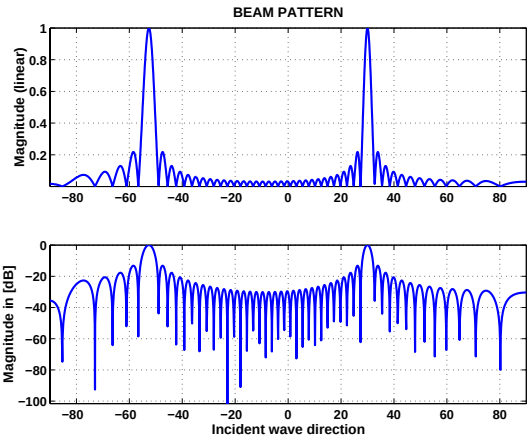

(d) 1.2mm pitch with apodization

Figure 2.7: Theoretical beam patterns in far field for the 32-element ultrasonic array in copper, respective with pitch 1mm and 1.2mm. Upper row without apodization and lower row with Hamming apodization.

which is known as the *sinc* function of peak value M. Main lobe width is normally defined in terms of an angle either to the first zero in the beam pattern or to the point where the beam amplitude drops to a certain level. The $3dB$ beam width (half-power beam-width)defines an angle Θ_{3dB} that is used as a measure of spatial resolution.

$$\Theta_{3dB} = 0.89 \cdot \arcsin(M\delta)^{-1} = 0.89 \cdot \arcsin(\frac{\lambda}{Md}) \tag{2.12}$$

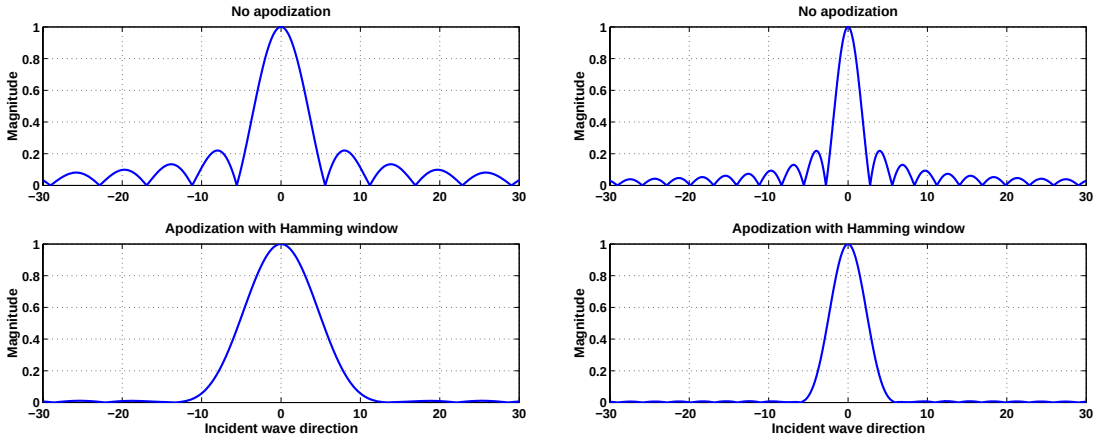

(a) 16-element array

(b) 32-element array

Figure 2.8: Theoretical beam patterns in far field for the 16- respective 32-element ultrasonic arrays in copper, respective without and with apodization.

Thus, spatial resolution of an array is inverse proportional to the product of its relative separation δ and the number of its elements (see Figure 2.8). Note that the definition Eq. 2.12 is valid for an array without apodization only. As it was mentioned above, apodization attenuates the side lobes but decreases the resolution, which can be clearly seen in Figure 2.8. Another drawback of apodization is that it decreases the overall energy emitted by an array in transmission and decreases signal to noise ratio in reception (since outer array elements are attenuated).

2.1.7 Finite sized array elements

Arrays $A16EL$ and $A32EL$ used in the above-presented simulations were artificial since they consisted of point like, infinite small elements. Real arrays have finite sized elements able to emit and receive a finite amount of energy. Element size is mainly limited by the array pitch that determines location of grating lobes (see Section 2.1.5). Thus, each array design results from a compromise between the amount of energy emitted/received by its individual elements, and the desired spatial characteristics determining array's spatial resolution as well as the position of grating lobes. Finite sized elements introduce diffraction effects to the array's spatial characteristics that can be clearly observed in the near field.

Diffraction effects result from the fact that by virtue of Huygens' principle, a finite sized acoustic transducer emits an infinite number of spherical waves originating at all points at its surface. The field observed at each point of the surrounding space is a result of interference of those waves. The reverse is observed during reception, the electrical signal observed at the transducer output is produced as an integral of the acoustical field incident at all points of the transducer's surface. The result of the interference is well pronounced close to the transducer (in

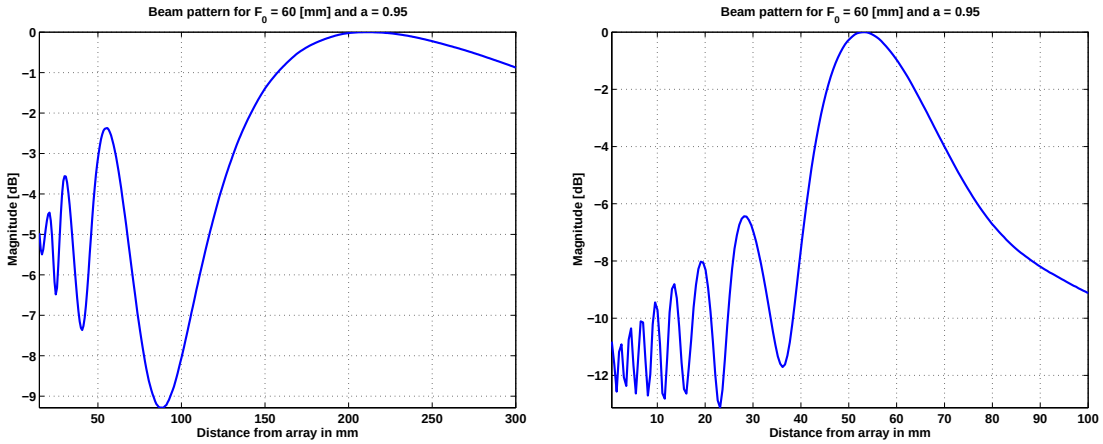

(a) Unfocused array

(b) Focused array

Figure 2.9: Beam intensity on axis of 32-element ultrasonic array $A32FEL$ in copper, respective unfocused and focused (note different scales on z-axes).

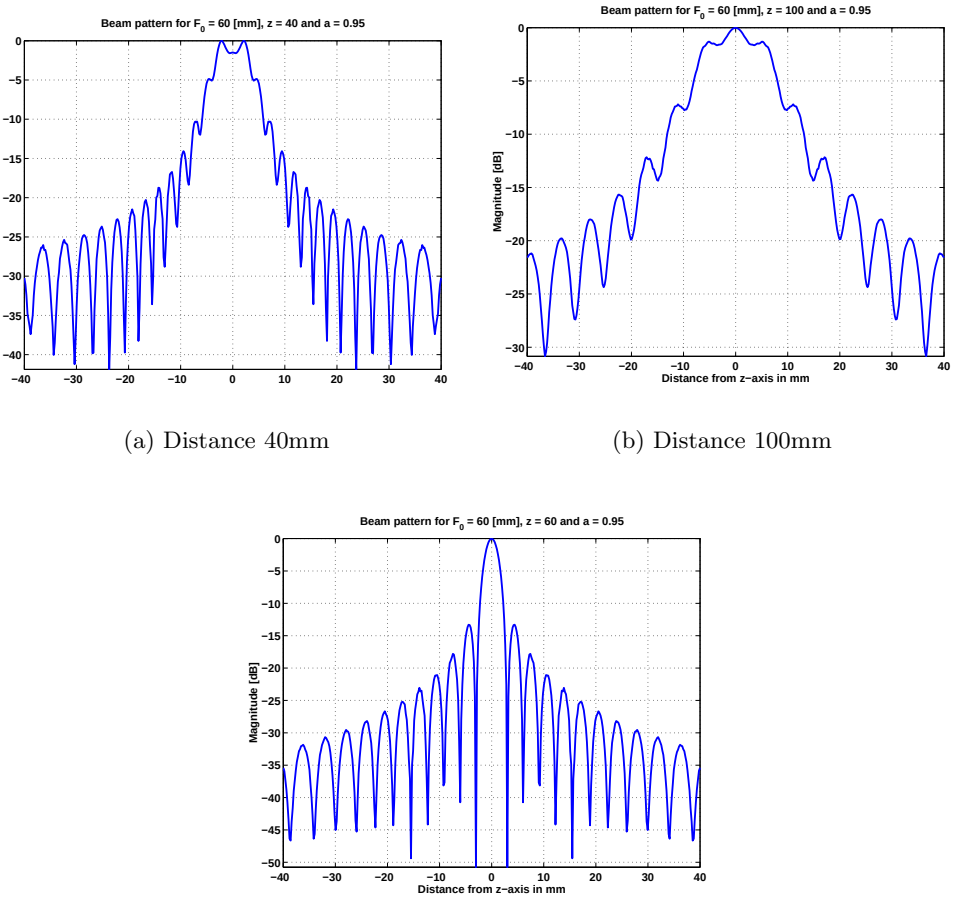

(a) Distance 40mm

(b) Distance 100mm

(c) Distance 60mm

Figure 2.10: Beam cross section for the array $A32FEL$ focused at 60mm in copper, at a distance respective 40, 100 and 60mm.

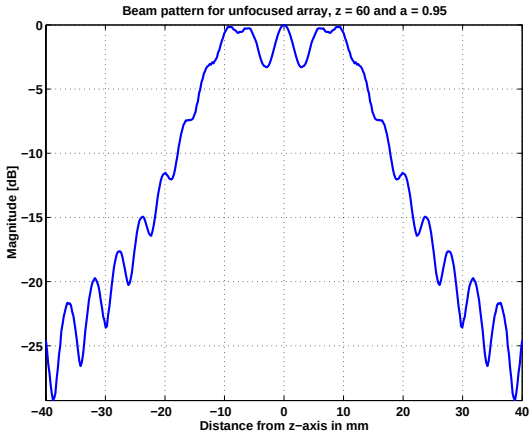

(a) Distance 60mm

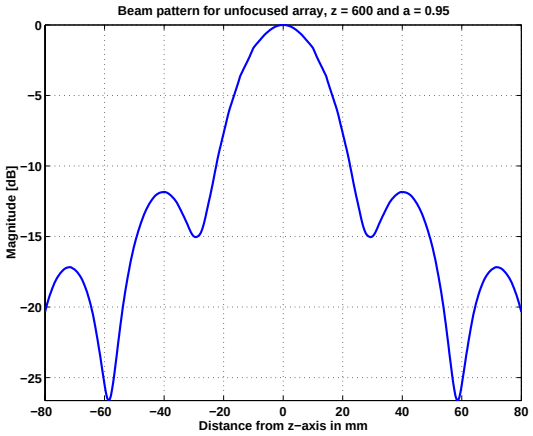

(b) Distance 600mm

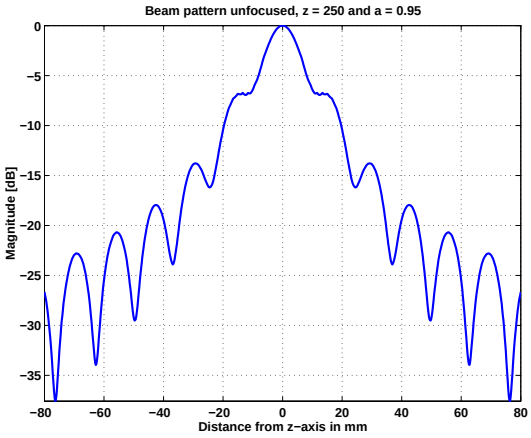

(c) Distance 250mm

Figure 2.11: Beam cross section for the unfocused array $A32FEL$ in copper, at a distance, respective 60, 250 and 600mm (note different scales on x-axes).

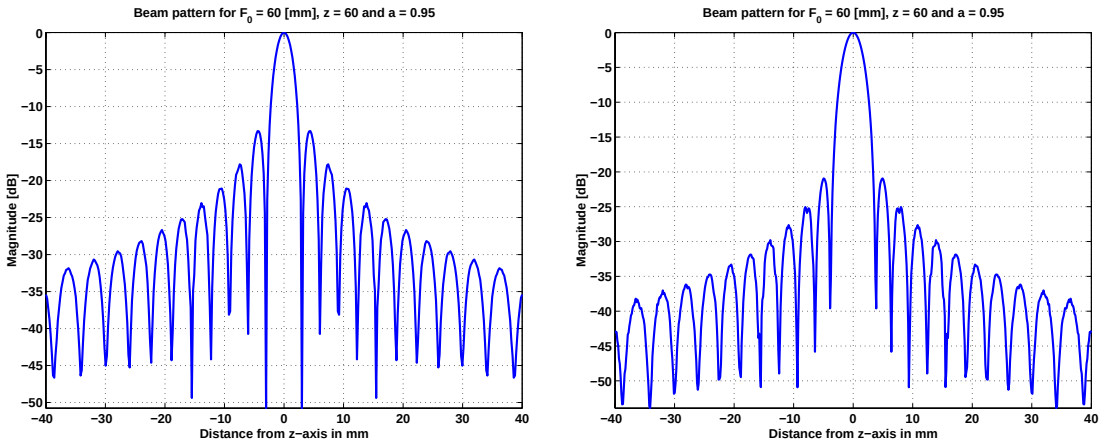

(a) Without apodization

(b) With apodization

Figure 2.12: Beam cross section at a distance 60mm for the for the array $A32FEL$ focused at 60mm in copper, respective without and with apodization (note slightly different scales on y-axes).

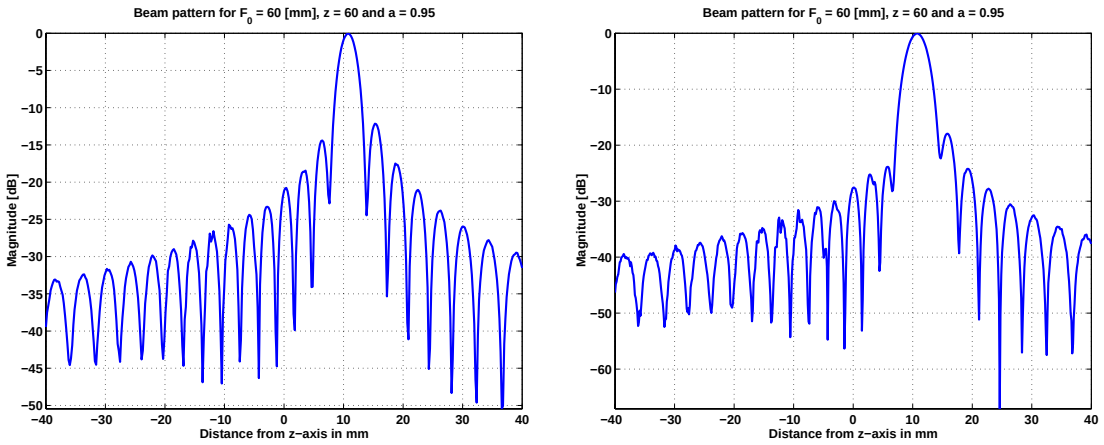

(a) Without apodization

(b) With apodization

Figure 2.13: Beam cross section at a distance 60mm for the for the array $A32FEL$ focused at 60mm and steered with 10° in copper, respective without and with apodization (note slightly different scales on y-axes).

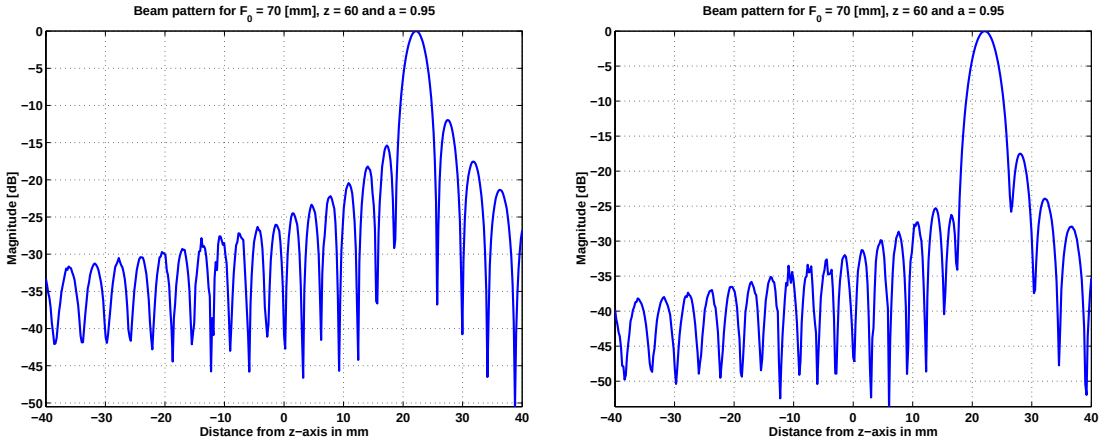

(a) Without apodization

(b) With apodization

Figure 2.14: Beam cross section at a distance 60mm for the for the array $A32FEL$ focused at 70mm and steered with 20° in copper, respective without and with apodization (note slightly different scales on y-axes).

near field) where the difference in waves' times of flight results in considerable phase differences. In far field the phase differences become less significant and the spatial characteristics tend to those for point like elements.

Below we present a number of simulations illustrating the diffraction effects introduced by finite sized array elements. The simulations were performed using the Simulation Tool DREAM [6] for a realistic version of array $A32EL$. The array referred to as $A32FEL$ had 32 elements with width 0.95mm, array pitch was 1mm. The simulations were made for longitudinal waves in copper for a single continuous frequency 3MHz. Note that the simulations show beam patterns obtained by applying respective focusing laws in transmission only, the effects of the focusing laws in reception are not included.

Beam intensity on z-axis for an unfocused $A32FEL$ and the same array focused at 60mm can be compared in Figure 2.9; it can be clearly seen that the focal law used in transmission shifts the beam maximum from approx. 210mm to 55mm. The reason that the real the focal depth is somewhat lower than the nominal 60mm used in the focusing law is the finite element size, for point sources the same focusing law results in the correct focal depth (cf. Figure 2.5). The respective cross beam sections for the focused and unfocused $A32FEL$ are presented at Figure 2.10 and Figure 2.11, respectively.

The effects of apodization are illustrated by Figure 2.12 showing beam profile of the focused $A32FEL$. The same effect can be observed in Figures 2.13 and 2.14 for the steered and focused $A32FEL$.

Summarizing the comparison of the above-presented simulations, we can see differences between the arrays with point and finite sized elements in the near field where the finite size contributes to diffraction, while in the far field the respective beam patterns are the same.

2.1.8 Transducer bandwidth

The above presented results were calculated for transducers excited with continuous wave with single frequency, which is a standard way of presenting beam patterns used in literature. Real transducers, however, have certain frequency response (bandwidth) that depends on their elec-

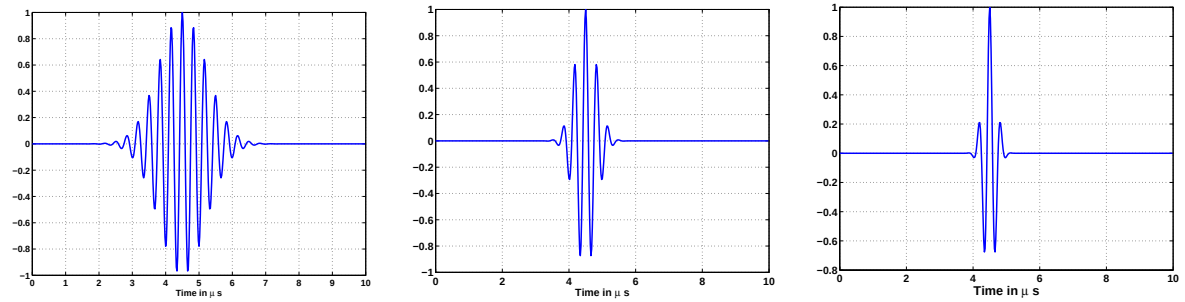

(a) Pulse 1 (b) Pulse 2 (c) Pulse 3

Figure 2.15: Pulses used for the illustration of the influence of pulse bandwidth on array beam pattern.

tromechanical characteristics. Transducer bandwidth is an important factor that influences its

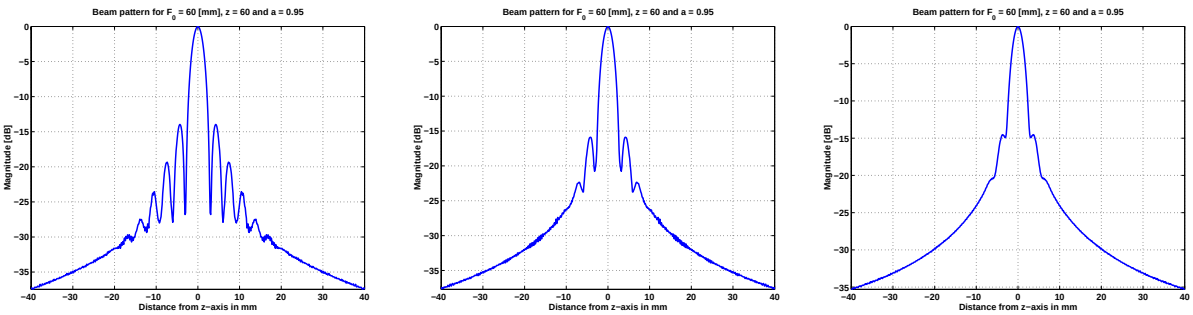

(a) Excitation with pulse 1 (b) Excitation with pulse 2 (c) Excitation with pulse 3

Figure 2.16: Beam cross section at a distance 60mm for the array $A32FEL$ focused at 60mm in copper excited using pulses, respective 1, 2 and 3.

beam pattern. A wide band excitation reduces the interference effects that are well pronounced especially in the transducer's near field.

Generally, the wider bandwidth the smoother are the beam patterns — the side lobes become less pronounced and the oscillations on the axis in the near field are smoothed. This can be observed in Figures 2.16 and 2.17 where the beam patterns are presented for three different exciting pulses shown in Figure 2.15. The pulses are artificially generated 3MHz sine wave with envelopes of different lengths and bandwidths. The beam cross sections at focal distance 60mm obtained for the $A32FEL$ excited with the respective pulses are presented at Figure 2.16. It is apparent that the shortest pulse (Pulse 3, which has the largest bandwidth) results in a very smooth beam cross section. Similar effect can be observed in Figure 2.17 showing the respective beam profile on the axis.

2.1.9 Beamformers

Beamforming in transmission is rather simple for practical realization, array elements are excited by the pulses that are generated in different time instances to form a desired wavefront. Modern digital electronics running with high clock frequency rates enables achieving sufficient time resolution in the range of nanoseconds. However, beamforming in the reception is far more

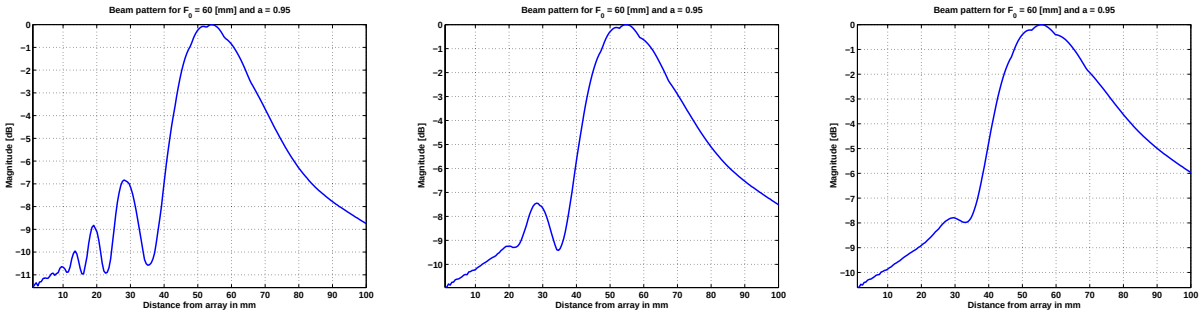

(a) Excitation with pulse 1 (b) Excitation with pulse 2 (c) Excitation with pulse 3

Figure 2.17: Beam profile on axis for the array $A32FEL$ focused at 60mm in copper excited using pulses, respective 1, 2 and 3.

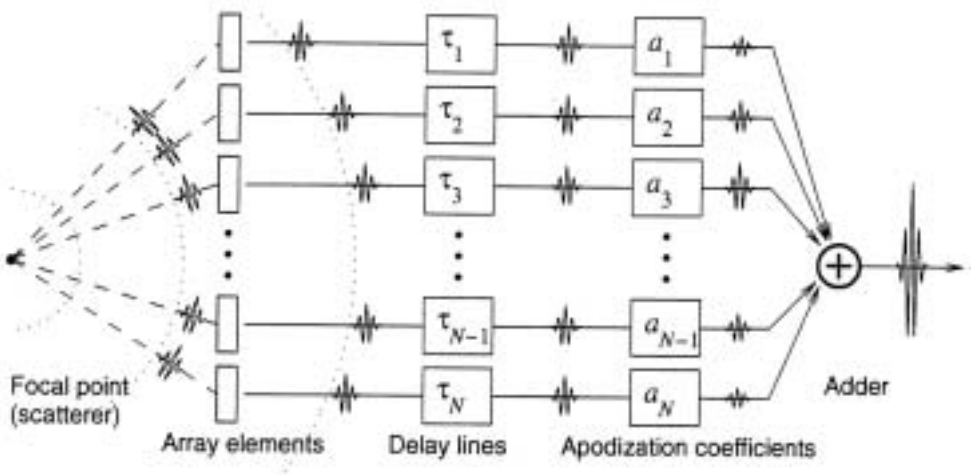

Figure 2.18: A time domain delay-and-sum beamformer.

complicated since the signals received by the array elements have to be delayed to enable coherent summation according to the scheme shown in Figure 2.18. The delay elements denoted by $\tau_1, \ldots, \tau_N$ delay the received signals, their amplitude is then modified by the apodization coefficients $a_1, \ldots, a_N$ and a coherent sum is produced in the end. Modern beamformers employ A/D converters for converting signals received by the array elements into a digital form. The A/D converters have to be characterized both by a high sampling frequency (tenths of MHz) and by high resolution (10 bits at least). In many applications low power consumption can also be an important requirement. However, the most difficult issue is providing sufficient resolution for the discrete time delay elements (denoted by $\tau_1, \ldots, \tau_N$ in Figure 2.18). Suppose that the sampling frequency f_s is 10 times higher that the transducer's center frequency, $f_s = 10f_0$. Typical transducer may have 100% bandwidth, which means it would receive signals with the highest frequency $1.5f_0$, which according to Nyquist theorem would require sampling frequency $3f_0$. Thus, from the signal processing point of view the signal would be over-sampled, however, the resolution in delay measured in degrees would be only $360°/10 = 36°$. Increasing sampling frequency is expensive and unjustified since the signal bandwidth is limited by the transducer (array).

One solution to this problem consists in using some type of *interpolation filter*, that is, an artificial technique that involves increasing the effective sampling frequency by an integer factor. This can be relatively easily done for the band-limited signals received by the array elements.

Another solution, often used in medical instruments employs *quadrature demodulation*, consisting in shifting the signal of interest to a lower frequency band, before sampling. The significant decrease in frequency obtained in this way releases sampling constraints and enables using relatively high sampling rates.

2.1.10 Conclusions

The main limitations of all beamforming systems are the restrictions imposed by the medium, which means that the wavelength and frequency feasible for a given medium will dictate the array size and technology. Transmitted and received waveforms are spread by the medium and volume scatterers, introducing unexpected errors and noise. Generally, higher frequency results in higher resolution but also imposes harder limitations on array geometry (pitch).

A detailed study of spatial aliasing indicates that it can be completely avoided by setting the array pitch equal to or less than half the wavelength. If however, such an inter-element spacing is not possible, the steering angle at which spatial aliasing occurs can be calculated.

The spatial resolution of a beamformer can be determined by measuring the difference between the -3dB power levels in the main lobe. Our study revealed that the spatial resolution is directly proportional to the product of number of elements and their spacing (cf. Eq. 2.12). Using the calculated beam widths, it is possible to determine the number of beams required to cover a two-dimensional input space (cf. Eq. 2.10).

Side lobe level is also an important factor that limits the resolution. Side lobe level can be reduced by using apodization (windowing function). The DFT (discrete Fourier transform) can be used to examine the characteristics of various window functions and the effects they have on the beam power plots. However, a narrow window function increases the main lobe width and thus decreases the resolution.

Finally, note that the above presented beamforming formulae yield correct results only in far field. In the near field the use of numerical simulations taking into account diffraction effects is recommended.

Bibliography

[1] M. Soumekh. *Synthetic Aperture Radar Signal Processing*. John Wiley & Sons, Inc., 1999.

[2] H.L. Van Trees. *Optimum Array Processing. Part IV of Detection, Estimation, and Modulation Theory*. John Wiley & Sons, Inc., 2002.

[3] B. D. van Veen and K. M. Buckley. Beamforming: A versatile approach to spatial filtering. *IEEE ASSP Magazine*, April 1988.

[4] J. Goodman. *Introduction to Fourier Optics*. McGraw-Hill, second edition, 1996.

[5] G.S. Kino. *Acoustic Waves: Devices, Imaging and Analog Signal Processing*, volume 6 of *Prentice-Hall Signal Processing Series*. Prentice-Hall, 1987.

[6] B. Piwakowski and K. Sbai. A new approach to calculate the field radiated from arbitrarily structured transducer arrays. *IEEE Trans. on Ultrasonics, Ferroelectrics, and Frequency Control*, pages 422–440, 1999.

Chapter 3

Iterative Approach to ESAFT

by Erik Wennerström

3.1 Introduction

Extended synthetic aperture focusing technique (ESAFT) that was proposed in the previous phase of this project [1] will be further developed and verified in this chapter. Recently, it has been shown that this technique is superior both to conventional SAFT and phased array techniques concerning lateral resolution [2, 3]. Now, we propose an improved synthetic aperture imaging technique that will be characterized by the increased lateral resolution compared with ESAFT. ESAFT is based on the assumption that probability density of the imaged targets (so called prior) is Gaussian, which is the simplest case for the analysis. The increase of performance is expected due to the efficient use of the prior information available in the ultrasonic imaging system. A more realistic assumption concerning prior probability density will be investigated, resulting in an iterative algorithm using the result obtained in the first step as a prior for the second step. The algorithm will be developed using simulated data and verified on data acquired using our array system.

The second section of this chapter, Section 3.3, reports an implementation of the ESAFT method to 3D ultrasonic data. It verifies the ESAFT method on real data and shows how the ESAFT can be used to improve resolution of ultrasonic images collected with a real measurement system.

3.2 Iterative approach to the ESAFT algorithm

The model-based statistical approach to ultrasonic synthetic aperture imaging presented in our recent report [1] uses a discrete linear model of the imaging system expressed with matrix notation. Diffraction effects introduced by ultrasonic array and noise present in the acquired data are included in the linear model and a reconstruction filter is designed producing the best linear estimate of the original image. Covariance matrices of the measurement noise and the reconstructed image are parameters in our filter. The assumptions made are usually quite conservative, assuming that little is known about the image. Below, in the first section of this chapter, Section 3.2, an extension to this method is proposed. In the proposed method, the initial parameter values are refined, step by step, based on the results from the previous iterations. It is shown that this approach offers some improvement over the standard ESAFT algorithm.

3.2.1 Discrete linear model of the imaging system

The ESAFT algorithm is based on a linear convolution model of the imaging system (see [2] for details). The model includes spatial and electrical impulse responses of the aperture and targets in the image. The targets can be described in a discrete form with an *object function* $o(x, z)$. It is defined as being zero where there is no target and equal to the target's reflectivity at points $\mathbf{r}(x, z)$ where a target is located

$$o(x,z) \triangleq \begin{cases} s_e & \text{for } \; x,z \in \mathcal{T} \\ 0 & \text{otherwise.} \end{cases} \tag{3.1}$$

where $\mathcal{T}$ is the set of points in the xz-plane where the targets are located. The object function $o(x, z)$ corresponding to certain region of interest (ROI) can be discretized by taking its values at the sampling points, to form a matrix $\mathbf{O}$.

An A-scan measurement from a single point target is a convolution of three components: The double path spatial impulse response (SIR) from the source to the target, the electrical impulse

response, and the excitation signal. A complete A-scan model takes the form of a sum of such convolutions over all targets in the image. Thus, a discrete version of an A-scan measurement vector can be expressed as

$$\mathbf{y}_n = \sum_{\tilde{n}=n-L}^{n+L} \mathbf{h}_{sir}(\tilde{n}, n)\mathbf{o}_{\tilde{n}} + \mathbf{e}_n \tag{3.2}$$

where $\mathbf{e}_n$ is the measurement noise, vector $\mathbf{o}_{\tilde{n}}$ denotes column $\tilde{n}$ in $\mathbf{O}$, and vector $\mathbf{h}_{sir}(\tilde{n}, n)$ contains the sampled SIR at a distance $d(\tilde{n}, n) = |x_{\tilde{n}} - x_n|$ (which is the horizontal distance between the observation point and the source).

Consider measurements consisting of M A-scans, each of length N. Let us form the *measurement vector* $\mathbf{y}$ by concatenating all A-scans into a single $M * N$ elements vector. The *image vector* $\mathbf{o}$ is formed similarly by vectorizing $\mathbf{O}$. A B-scan model can then be expressed in compact matrix notation as

$$\mathbf{y} = \mathbf{P}\mathbf{o} + \mathbf{e} \tag{3.3}$$

where $\mathbf{e}$ is the noise and $\mathbf{P}$ is a $MN \times MN$ block diagonal transformation matrix, including spatial and electrical impulse responses introduced by the measurement system. See [4, 5] for more information on the impulse responses and details of this model.

3.2.2 The inverse filter, minimization problem

The approach proposed in [2] consist in finding $\hat{\mathbf{o}}$ from $\mathbf{y}$ using a reconstruction filter K that minimizes the mean square error $I = E\{\|\mathbf{o} - \mathbf{K}\mathbf{y}\|^2\}$, i.e., the filter is found by minimizing

$$\arg\min_{\mathbf{K}} I \tag{3.4}$$

As shown in previous works, [1, 4] the linear reconstruction filter that minimizes I can be expressed in an analytical form

$$\mathbf{K} = (\mathbf{C_{oo}}^{-1} + \mathbf{P}^T\mathbf{C_{ee}}^{-1}\mathbf{P})^{-1}\mathbf{P}^T\mathbf{C_{ee}}^{-1} \tag{3.5}$$

where $\mathbf{C_{oo}}$ is the covariance matrix of the image vector $\mathbf{o}$ and $\mathbf{C_{ee}}$ is the covariance matrix of the noise $\mathbf{e}$. Under the assumptions that $\mathbf{o}$ and $\mathbf{e}$ are Gaussian the resulting estimate $\hat{\mathbf{o}} = \mathbf{K}\mathbf{y}$ is equal to the *maximum a postiori* estimate of $\mathbf{o}$, in other words the most probable $\mathbf{o}$, given the measurements $\mathbf{y}$. Assuming that $\mathbf{e}$ and $\mathbf{o}$ are also Gaussian, the estimate becomes

$$\arg\max_o p(o|y) = \arg\min_o \{\frac{1}{2}(\mathbf{y} - \mathbf{P}\mathbf{o})^T\mathbf{C_{ee}}^{-1}(\mathbf{y} - \mathbf{P}\mathbf{o}) + \frac{1}{2}\mathbf{o}^T\mathbf{C_{oo}}^{-1}\mathbf{o}\} = \arg\min_o J \tag{3.6}$$

In solving Eqs 3.5 and 3.6, the covariance matrix $\mathbf{C_{oo}}$ can be viewed as containing our *prior knowledge* of $\mathbf{o}$. It must be set to a numerical value before solving the equation. A common assumption on $\mathbf{C_{oo}}$ is that it is diagonal, with all elements on the diagonal equal. This assumption means that all elements in the image $\mathbf{o}$ are uncorrelated from each other, and the probability of a value deviating from zero is equally large for all image elements.

Here, we propose a way of extending the minimization problem by taking into account the second unknown parameter, a vector containing all the diagonal elements in $\mathbf{C_{oo}}$. More details on this approach can be found in [6]. Let

$$\mathbf{C_{oo}} = \begin{pmatrix} \delta_1 & 0 & \dots & 0 \\ 0 & \ddots & & \\ \vdots & & & \\ 0 & & & \delta_M \end{pmatrix} \tag{3.7}$$

Now, consider the minimization of Eq. 3.6 with respect to both $\mathbf{o}$ and $\mathbf{C_{oo}}$. It has to be done in several steps, first find

$$\hat{\mathbf{o}}_1 = \arg\max_{\mathbf{o}} J|_{\mathbf{C_{oo}}=\lambda_o \mathbf{I}} \tag{3.8}$$

using Eq. 3.6 above. The covariance matrix $\mathbf{C_{oo}}$ is in this step is set to the usual prior, i.e. the unit matrix multipled by a constant.

Secondly, minimize J again with respect to $\mathbf{C_{oo}}$

$$\mathbf{C_{oo}}_1 = \arg\max_{\mathbf{C_{oo}}} J|_{\mathbf{o}=\hat{\mathbf{o}}_1} \tag{3.9}$$

that is, when $\mathbf{o} = \hat{\mathbf{o}}$, find the $\mathbf{C_{oo}}$ that minimizes J. The resulting estimate of $\mathbf{C_{oo}}$ is then used to find a new estimate of $\mathbf{o}$, and so forth. This process is repeated as long as J converges.

The algorithm can be summarized in steps:

1. Initialize $i := 1$ and $\mathbf{C_{oo}}_0 = \lambda_o \mathbf{I}$
2. Find the i:th estimate of the image, using the i-1:st estimate of the covariance matrix, Eq. 3.10.
3. Find the i:th estimate of the covariance matrix, using the estimate of the image from the last step, Eq. 3.11.
4. Set i:=i+1
5. Repeat step 2, 3 and 4 as long as the error J decreases sufficiently fast.

$$\hat{\mathbf{o}}_i = \arg\max_{\mathbf{o}} J|_{\mathbf{C_{oo}}=\mathbf{C_{oo}}_{i-1}} \tag{3.10}$$

$$\mathbf{C_{oo}}_i = \arg\max_{\mathbf{C_{oo}}} J|_{\mathbf{o}=\hat{\mathbf{o}}_i} \tag{3.11}$$

To eliminate trivial solutions to Eqs 3.10 and 3.11 we have to impose constraints on $\mathbf{C_{oo}}$. Without such constraints, various diagonal elements δ_i in $\mathbf{C_{oo}}$ could quickly grow out of proportion or quickly diminish.

The first constraint results from the condition that the total energy in the image should not change. Initial assessments of the measurement noise and the image energy are made when solving Eq. 3.10 and those should hold in each step of the iterated minimization.

The second constraint takes the form of a lower limit for $\delta_i = 0$, indeed if δ_i tended to 0 it would be equivalent to assuming that there is nothing in the corresponding area in the image. This would not be a sensible assumption as the method should be open to the possibility of a target anywhere in the image.

The above presented upper and lower constrains on δ_i, can be expressed in the following form

$$C_1(\mathbf{o}, \mathbf{C_{oo}}) = \sum_m \delta_m^2 - K_1 = 0 \tag{3.12}$$

$$C_2(\mathbf{o}, \mathbf{C_{oo}}) = \sum_m \frac{1}{\delta_m^2} - K_2 = 0 \tag{3.13}$$

where K_1 and K_2 are constants. K_1 can be set to $\lambda_o N$, and K_2 can be seen as a user parameter. If K_2 is chosen large, all δ_i are allowed to vary with less restrictions.

3.2.3 Minimization with constraints

To minimize the criterion 3.6 under the constraints 3.12 and 3.13, we minimize the Lagrangian (see [7] for details)

$$L = J + \lambda_1 C_1 + \lambda_2 C_2 \tag{3.14}$$

Derivation of Eq. 3.14 with respect to $\mathbf{o}$, and setting $\mathbf{C_{oo}} = \lambda_o \mathbf{I}$ yields the same expression for $\hat{\mathbf{o}}$ as the filter, Eq. 3.5:

$$\hat{\mathbf{o}} = (\mathbf{C_{oo}}^{-1} + \mathbf{P}^T \mathbf{C_{ee}}^{-1} \mathbf{P})^{-1} \mathbf{P}^T \mathbf{C_{ee}}^{-1} \mathbf{y} \tag{3.15}$$

In the second optimization step we use the $\hat{\mathbf{o}}$ found in the previous step as an estimate of $\mathbf{o}$. Minimizing L in this step is not as trivial as before. Let us find

$$\frac{dL}{d\delta_m^2}|_{\mathbf{o}=\hat{\mathbf{o}}} = \frac{dL}{d\delta_m^2} \left[\sum_m \frac{\hat{o}_m^2}{\delta_m^2} + \lambda_1 \left(\sum_m \delta_m^2 - K_1 \right) + \lambda_2 \left(\sum_m \frac{1}{\delta_m^2} - K_2 \right) \right] \tag{3.16}$$

$$= \frac{1}{2} \left(-\frac{\hat{o}_m^2}{\delta_m^4} \right) + \lambda_1 (1) + \lambda_2 \left(-\frac{1}{\delta_m^4} \right) \tag{3.17}$$

Solving Eq. 3.17 for δ_m^2 yields

$$\delta_m^2 = \sqrt{\frac{\lambda_2 + \frac{1}{2}\hat{o}_m^2}{\lambda_1}} \tag{3.18}$$

and inserting in the constraints Eq. 3.12 and Eq. 3.13 results in

$$K_1 = \sum_m \sqrt{\frac{\lambda_2 + \frac{1}{2}\hat{o}_m^2}{\lambda_1}} \tag{3.19}$$

$$K_2 = \sum_m \sqrt{\frac{\lambda_1}{\lambda_2 + \frac{1}{2}\hat{o}_m^2}} \tag{3.20}$$

This is a system of two non-linear equations with two unknowns that are difficult to solve analytically; the equations have to be solved numerically. When $\lambda_{1,2}$ has been found, all δ_m can readily be calculated from Eq. 3.18. These steps can now be iterated until L in Eq. 3.14 converges. Below, this algorithm will be referred to as *iterated ESAFT*.

Note that if λ_2 is close to zero, which may occur when K_2 is large, then Eq. 3.18 reduces to $\delta_m^2 \approx \alpha \hat{o}_m$; the estimated variances for the next step will simply be the estimated image from the recent step, scaled by some constant α.

3.2.4 Experimental setup

The objective of the measurements presented here was to evaluate performance of the proposed method. The ability to resolve two closely spaced targets was used as the performance measure. Ultrasonic data was collected using the ALLIN array system with a 3MHz, 64-element array. Two 0.3 mm thick steel wires, separated by 2 mm and submersed in water were used as targets. B-scans were gathered along a line perpendicular to the wires.

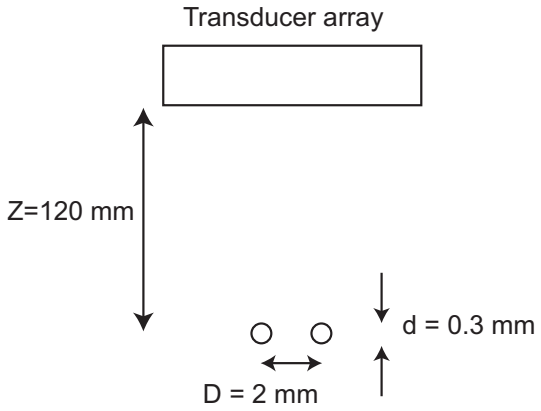

Figure 3.1: Measurement setup. Two closely spaced wires in water.

The array consists of 64 rectangular elements spaced at 1mm. The elements that take the form of 1mm strips can be easily bridged to form larger apertures. If all elements in an aperture are fired simultaneously, they act like a rectangular unfocused source of variable size. The number of 1mm wide array elements used in the experiments (and thus the transducer width in mm) was, respectively, 1, 4, 8 and 16mm. The distance between targets and the aperture was constant 120mm as shown in Figure 3.1. B-scans were acquired using scanner's spatial sampling 0.5 mm.

3.2.5 Experimental results

In this section, the results obtained for the above listed transducer sizes (aperture widths) are presented in Figures 3.2 to 3.5. B-scan images of raw data, the ESAFT results and the iterated ESAFT are presented in the upper rows. In the lower rows B-scan profiles obtained from the ESAFT and the iterated ESAFT are shown besides the plot of the optimizing criterion.

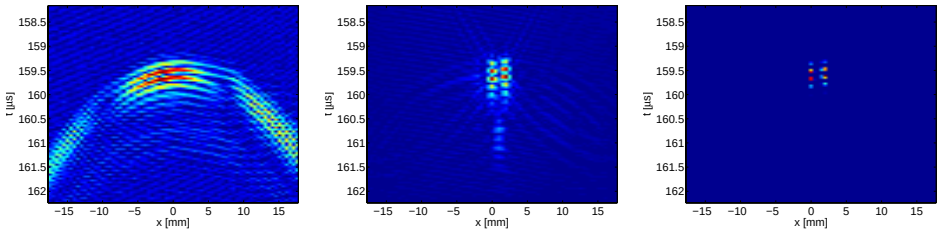

(a) Original B-scan (b) B-scan, original ESAFT (c) B-scan, iterated ESAFT

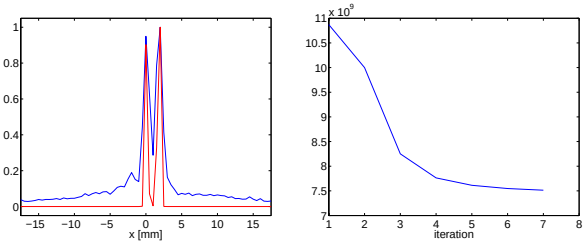

(d) Profiles (e) Error criterion

Figure 3.2: Measured and processed data for 1 mm transducer.

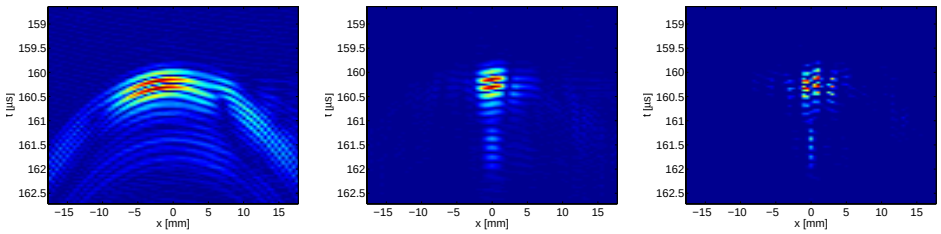

(a) Original B-scan (b) B-scan, original ESAFT (c) B-scan, iterated ESAFT

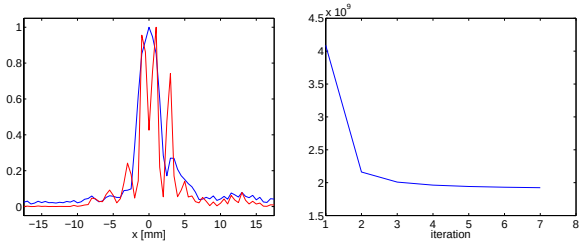

(d) Profiles (e) Error criterion

Figure 3.3: Measured and processed data for 4 mm transducer.

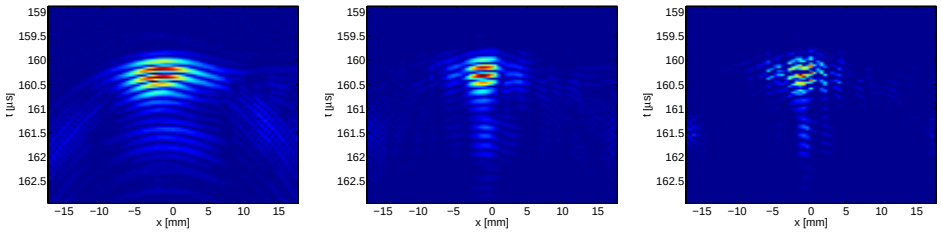

(a) Original B-scan (b) B-scan, original ESAFT (c) B-scan, iterated ESAFT

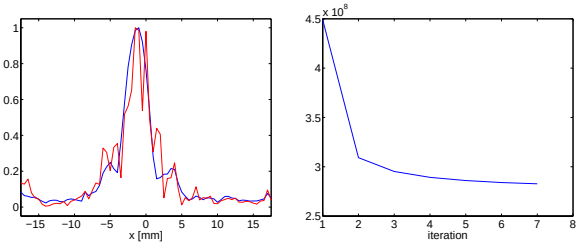

(d) Profiles (e) Error criterion

Figure 3.4: Measured and processed data for 8 mm transducer.

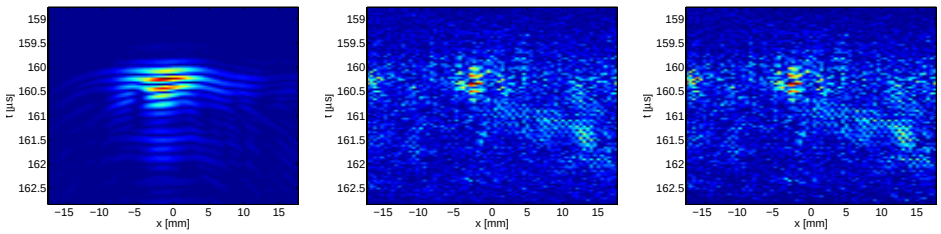

(a) Original B-scan (b) B-scan, original ESAFT (c) B-scan, iterated ESAFT

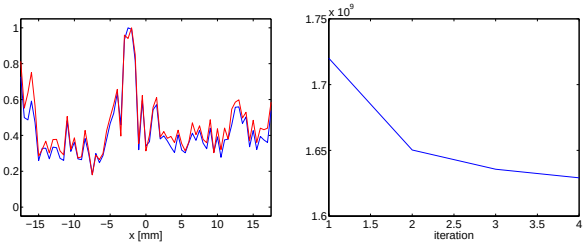

(d) Profiles (e) Error criterion

Figure 3.5: Measured and processed data for 16 mm transducer.

Summary

To summarize the above presented results , we show results for the 8 mm (8x1mm) aperture in Figures 3.6 and 3.7. Please recall that the larger aperture the more its spatial impulse response (SIR) deviates from the ideal SIR of a point like transducer. In consequence, when the ultrasonic measurement performed using a large aperture is processed using ordinary SAFT a satisfactory spatial resolution is difficult to achieve [1]. In this context, 8 mm aperture of a 3MHz transducer in water is fairly large for targets at a distance 120mm.

From the plots in Figure 3.6 can be seen that after the first iteration of the proposed algorithm the two wires have not been separated, but after further steps they can clearly be distinguished. In this example λ_0 in *step*1 was set to $1e^{-4}$. When a different start value ($\lambda_0 = 1e^{-6}$) was used

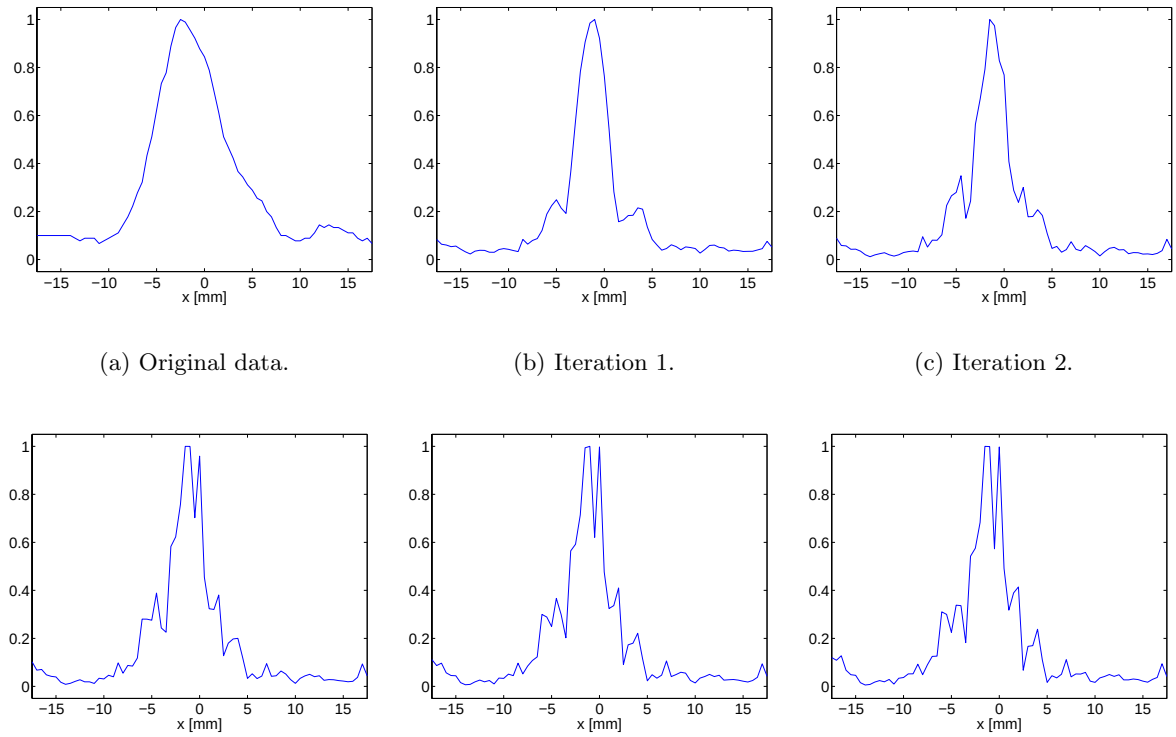

(a) Original data. (b) Iteration 1. (c) Iteration 2.

(d) Iteration 3. (e) Iteration 4. (f) Iteration 5.

Figure 3.6: Profile plots obtained for 8 mm transducer. After one iteration the two wires cannot be distinguished

the wires could be distinguished after the original single-step ESAFT approach, see Figure 3.7. Please note however, the higher noise floor and less distinct peaks corresponding to the wires comparing to the iterative SAFT result in Figure 3.6f. This illustrates the performance of the the iterative approach.

3.2.6 Conclusions

Even though the improvement seen in the previous section for the iterative ESAFT was modest, this approach has its practical advantages. Note that the original ESAFT method is essentially one single iteration of the iterative version, based on more or less correct assumptions concerning the covariances of the noise **e** and the image **o**. It is not expected (even though not fully tested in this report) that a defect or another target that could not be detected at all with the

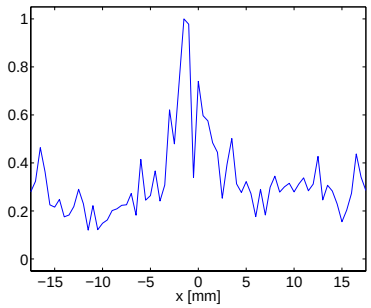

Figure 3.7: Th result obtained for 8 mm transducer, without the iterative approach for $\lambda_0 = 1e^{-6}$.

original ESAFT would be found after several iterations. However, since the detected targets are investigated more closely in several steps the result of defect classification should be more accurate.

From a user perspective both methods are similar — they require input estimates (initial) of variances for the noise $\mathbf{e}$ and the image $\mathbf{o}$, or at least a ratio between them. The iterative variant also requires an additional input — the ratio between K_1 and K_2. This might seem as an increase in complexity, but it is actually the other way around. Performance of the original ESAFT depends heavily on the initial estimates of variances $\mathbf{C_{oo}}$ and $\mathbf{C_{ee}}$. The images presented here were created after testing many reasonable values, looking at the results and selecting the most suitable candidate. The iterative ESAFT repeats its steps until the error criterion L converges, which makes it less dependent on the initial variances. Thus, it is much more suited for the automated defect detection/classification than the original ESAFT.

3.3 Synthetic Aperture Imaging for 3-Dimensional Data

3.3.1 Introduction

Until now, the ESAFT algorithm, which represents the family of synthetic aperture imaging (SAI) techniques has been applied to 2D ultrasonic data (B-scans). In this section we demonstrate the improvement that can be achieved due to the application of ESAFT to 3D ultrasonic data obtained from a phased array system. If a planar phased array is applied for a contact inspection of a solid specimen electronic focusing can be performed in one dimension only (along the array). In the other dimension the array is unfocused, which results in elliptical responses to small scatterers in the acquired C-scans. If a 3D ultrasonic data is available it can be post-processed using SAFT and the elliptical responses can, at least in theory, be converted to circular ones, resulting in an improved overall resolution.

In this Section, we show potential of this technique using both simulated and real ultrasonic data. In Section 3.3.4 we compare the performance of ESAFT to that of the classical SAFT algorithm [8].

3.3.2 3D data and focusing

Ultrasonic data analyzed in this section was acquired using the array system from Technology Design, UK, available at SKB's Canister Lab in Oskarshamn. Simulations of the measurement setup used in the SKB's Canister Lab were also performed to evaluate the method for a wider range of parameters than those available in the measured data.

The ultrasonic measurement system was used to acquire complete 3D ultrasonic data of the

inspected copper specimen. Movement and focusing along one of the axes was done purely electronically. More details of the system can be found in Section 3.3.3. The geometry of A- and B-scans in the measurement is illustrated by Figure 3.8. In the sequel a 2D matrix of data in the YZ - plane will be referred to as a B-scan.

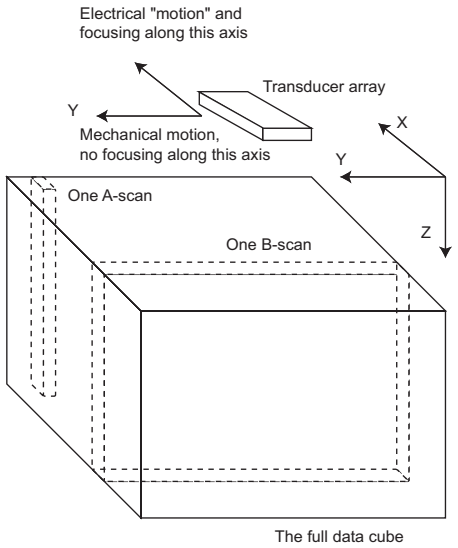

Figure 3.8: Geometry of A- and B-scan.

The ESAFT algorithm can be applied to such 3D ultrasonic data in essentially three different ways:

Normal 2D. Each B-scan is treated separately. Information found in one B-scan is not used when focusing others. (See section 3.3.3 for more on this assumption and its validity.) Focusing is achieved in one direction only.

2.5D focusing. An extension of the previous approach. Focusing is performed independently in both directions, one after another. The same assumptions as above are made.

Full 3D focusing. All the data in the complete data-cube is treated at once, in one single minimization problem. This includes very heavy computations and large amounts of RAM memory are required.

In the experiments presented here, the first approach (**Normal 2D**) has been chosen. Focusing along the X-axis was performed by the electronically by the instrument, so out task has been concerned with focusing in the other direction. Recently, some preliminary work and simulations have been done on the 3D approach, the results are promising, but they are not presented here.

3.3.3 Experiment

Measurement setup

The measurement system was equipped with a phased array consisting of 80 elements. A 32-element aperture was used at a time, and focusing was performed along the X-axis (parallel to the length of the array) both in transmission and using a standard delay-and-sum operations in the receiving electronics. Electronic scanning was performed by shifting the aperture, one element at a time. Along the Y-axis, the array was moved mechanically by stepper motors. No

focusing was performed along this mechanical axis. Figure 3.9 shows details of the acquisition system.

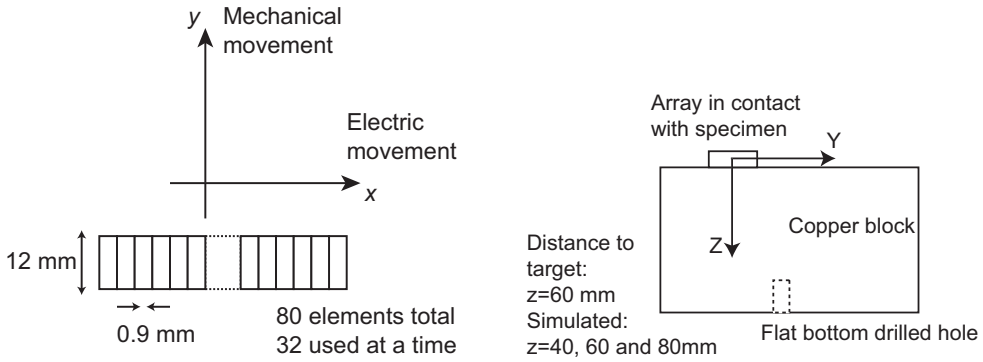

(a) Array geometry.

(b) Measurement setup.

Figure 3.9: Setup used in measurements and simulations.

Since focusing was only done in one direction, along the X-axis, the response of a point source in a C-scan took the form of an ellipse, with its longer axis in the Y-direction. An example of this can be seen in Figure 3.19.

Equal spatial sampling distance of 1mm was used in both Y- and X-direction for acquired and simulated ultrasonic data and the array was focused at 60mm. The A-scans were digitized using sampling frequency 50MHz. A block of copper with a small bottom drilled hole at a depth of 60mm from the upper surface was used as a target.

Simulated data

Three sets of simulated data were generated, for point targets at z =40, 60 and 80mm, respectively. The point targets can approximate the small hole used as scatterer in the case of measured data. All three data sets were generated for the same focusing law (60mm), so two of the simulated targets were out of focus. Sampling rate and spatial sampling grid were the same as in the real case, described above. All simulations were done using the DREAM toolbox. (See [9] and *http://www.signal.uu.se/Toolbox/dream/* for more information on the DREAM toolbox). For every set of simulated data, three levels of white additive Gaussian noise were added. The noise had an energy that resulted in the SNR of 10, 20 and 30 dB, respectively.

ESAFT

Both simulated and measured data was focused along the Y-axis using ESAFT. In this approach, every B-scan (a slice of the data cube in the YZ plane) is treated separately. Information found in nearby B-scans is not used for focusing. Every B-scan was treated as if it was independent from the others, which is a rather rough approximation. In the region close to where the array is focused it is valid, as most of the energy from a small scatterer will go into one B-scan only. At other ranges, the image will be smeared, and the energy will leak into many adjacent B-scans. So, outside the focal zone along the Z-axis, we can expect a somewhat reduced performance from the ESAFT algorithm as well.

3.3.4 Results

Simulations

Parameters of the simulated system are shown in Figure 3.9. The results from simulations are presented in Figures 3.10 through 3.18. Every figure has three subfigures. The first subfigure shows an unprocessed C-scan. It is composed of the maximum value of every A-scan, in an depth interval close to the target. The second subfigure is a C-scan obtained from the ESAFT processed image. The last subfigure shows profiles of the two C-scans along the Y-axis. Each point of the profiles is constructed by taking the maximum values of an entire row of the C-scan.

Note loss of focus in the unprocessed C-scans outside the focal zone. Sidelobes in the X-direction become apparent in the images from targets closer to the transducer than the focal distance (figure 3.10). The targets beyond the focal distance become large and blurred (figure 3.16). As discussed in section 3.3.3, ESAFT is less sensitive to distance than the delay-and-sum technique, but some loss of resolution is also expected.

The simulated results for all distances have a few things in common. Naturally, the resolution is only improved in the Y-direction, as ESAFT has only been applied along this axis. The improvement is well pronounced, even though it varies with the distance. For targets close to the focal distance, the elliptic original C-scan is replaced by a much more point-like image. Further from the focal distance, the improvement is not as dramatic, but evident.

Relatively high noise level that can be observed in the ESAFT C-scans is the price paid for the improved resolution. ESAFT is a spatio-temporal filter that compensates (deconvolves) transducer's diffraction effects by amplifying higher frequencies and thus also a high frequency noise.

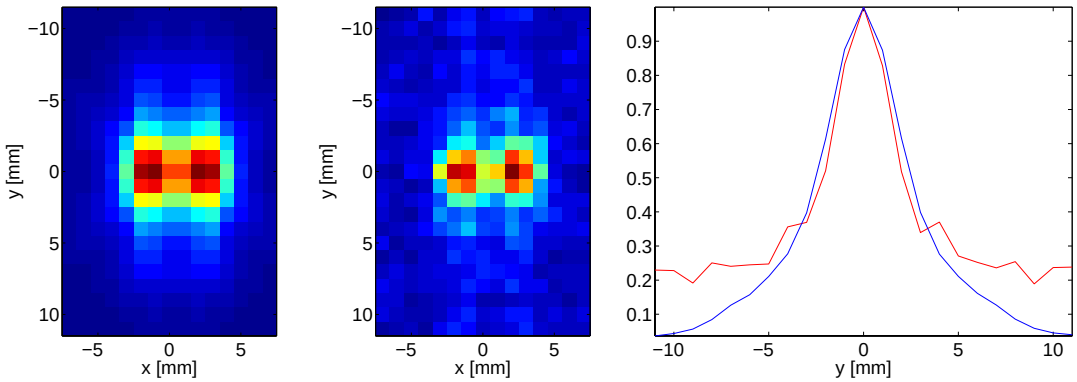

(a) Original C-scan

(b) ESAFT processed C-scan

(c) Profile plots. Unprocessed (blue) and ESAFT processed (red).

Figure 3.10: Simulated data. SNR 30dB, z=40 mm.

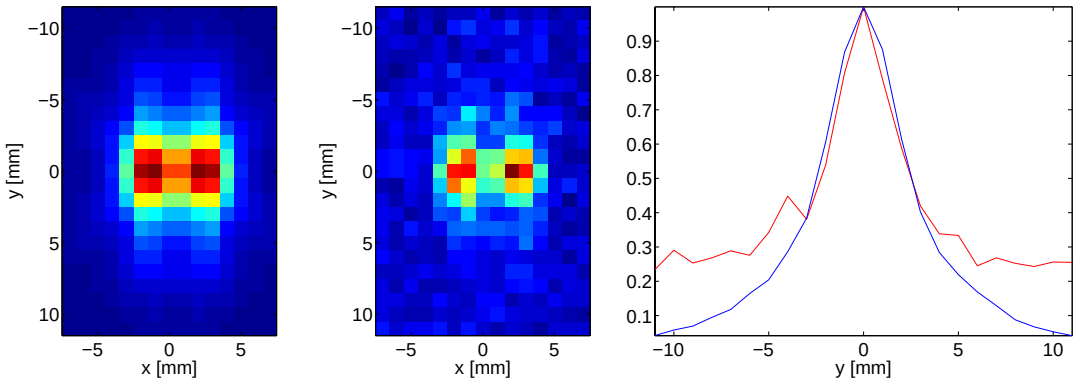

(a) Original C-scan

(b) ESAFT processed C-scan

(c) Profile plots. Unprocessed (blue) and ESAFT processed (red).

Figure 3.11: Simulated data. SNR 20dB, z=40 mm.

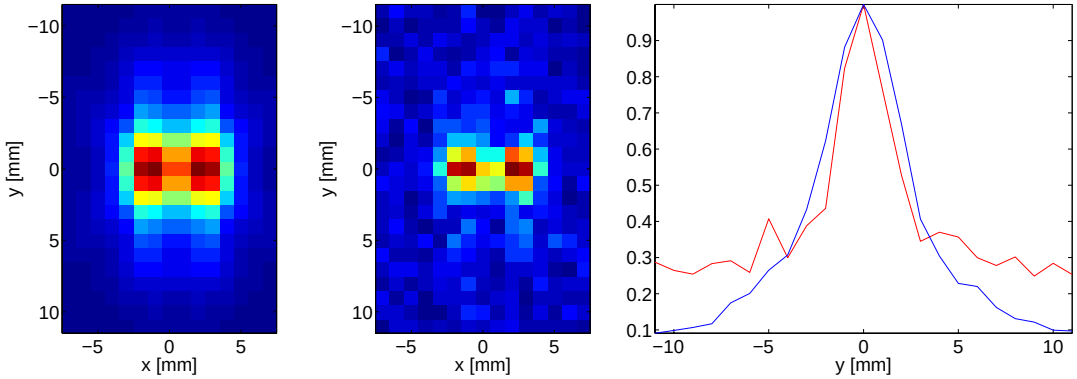

(a) Original C-scan

(b) ESAFT processed C-scan

(c) Profile plots. Unprocessed (blue) and ESAFT processed (red).

Figure 3.12: Simulated data. SNR 10dB, z=40 mm.

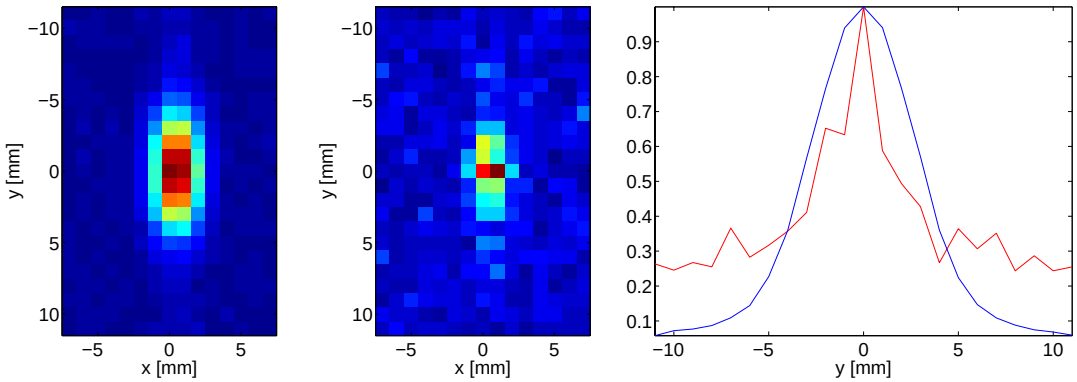

(a) Original C-scan

(b) ESAFT processed C-scan

(c) Profile plots. Unprocessed (blue) and ESAFT processed (red).

Figure 3.13: Simulated data. SNR 30dB, z=60 mm.

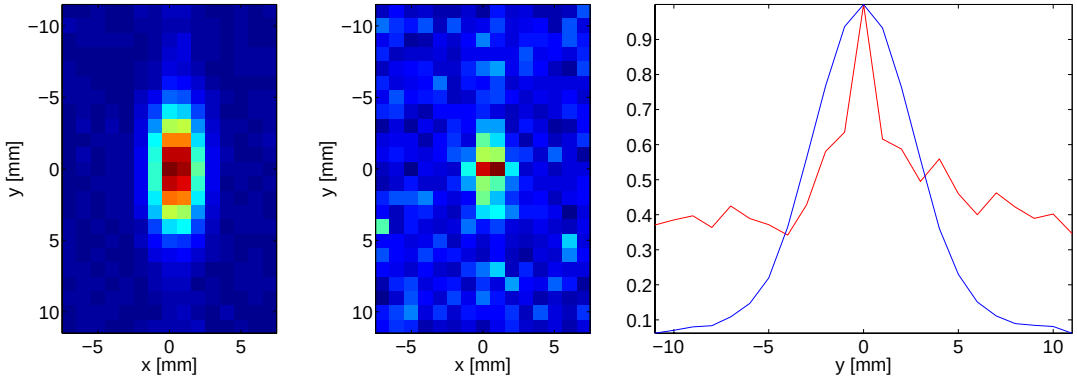

(a) Original C-scan

(b) ESAFT processed C-scan

(c) Profile plots. Unprocessed (blue) and ESAFT processed (red).

Figure 3.14: Simulated data. SNR 20dB, z=60 mm.

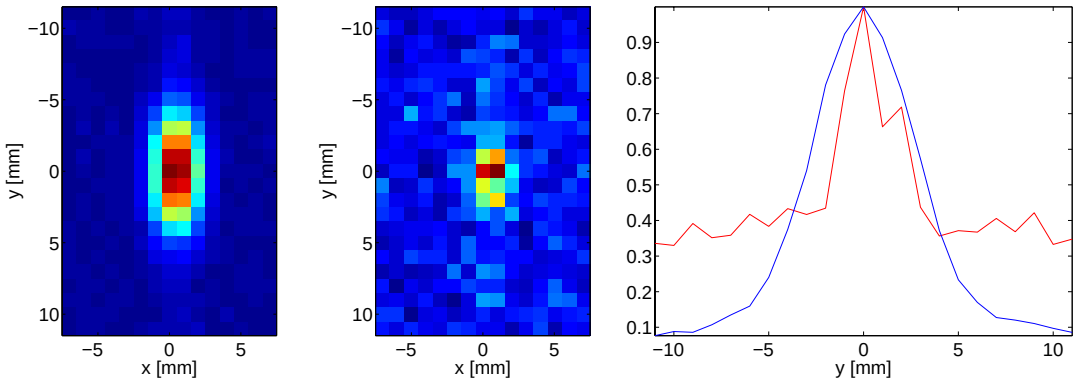

(a) Original C-scan

(b) ESAFT processed C-scan

(c) Profile plots. Unprocessed (blue) and ESAFT processed (red).

Figure 3.15: Simulated data. SNR 10dB, z=60 mm.

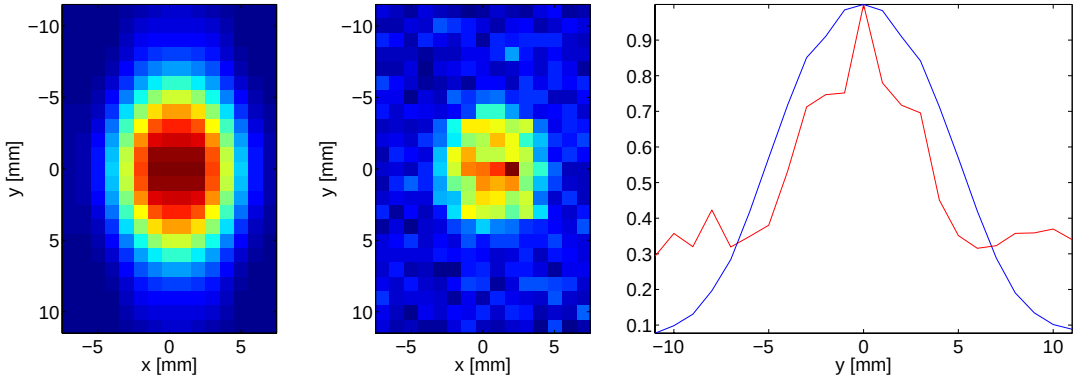

(a) Original C-scan

(b) ESAFT processed C-scan

(c) Profile plots. Unprocessed (blue) and ESAFT processed (red).

Figure 3.16: Simulated data. SNR 30dB, z=80 mm.

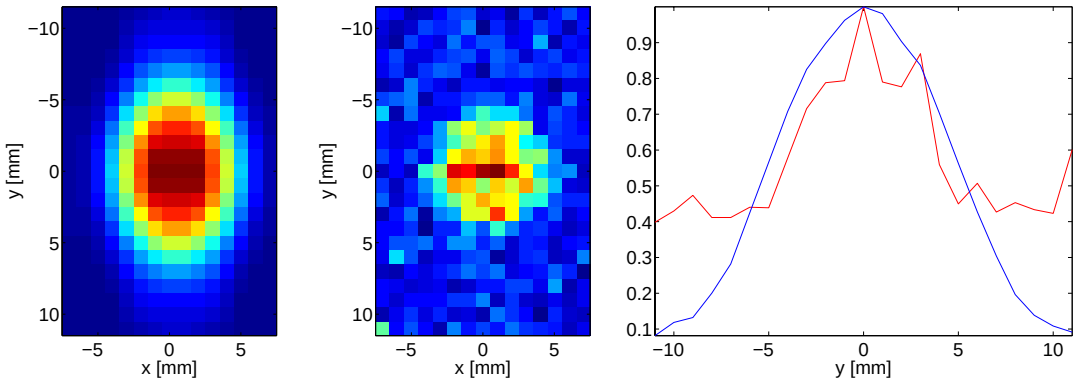

(a) Original C-scan

(b) ESAFT processed C-scan

(c) Profile plots. Unprocessed (blue) and ESAFT processed (red).

Figure 3.17: Simulated data. SNR 20dB, z=80 mm.

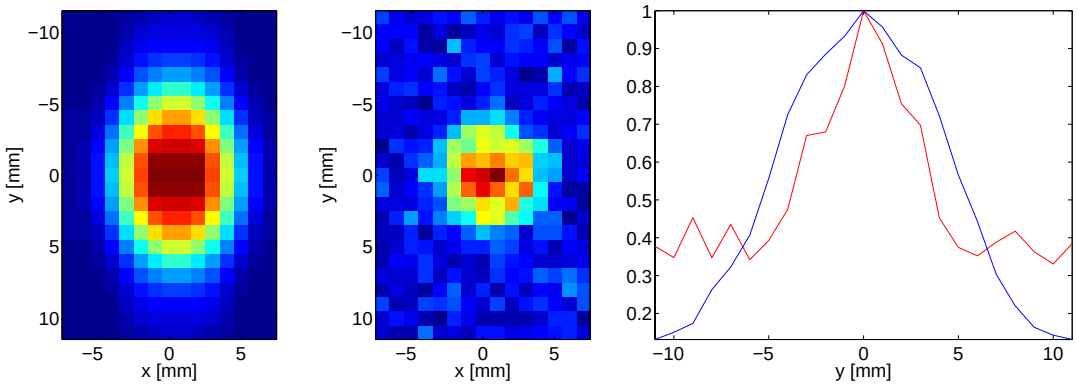

(a) Original C-scan

(b) ESAFT processed C-scan

(c) Profile plots. Unprocessed (blue) and ESAFT processed (red).

Figure 3.18: Simulated data. SNR 10dB, z=80 mm.

Measured data

The results of ESAFT processing of measured data are shown in Figure 3.19. The respective images presented in this figure were obtained in the same way as those in Section 3.3.4. It is apparent that the original C-scan is shaped like an ellipse instead of a circle, as the array is electrically focused in one direction only. After the ESAFT processing the target becomes much smaller and circular, which agrees well with the simulations in Section 3.3.4 above. A substantial improvement is also seen in the respective B-scans (Figure 3.19b and d). The improvement could be even better pronounced if the scanner step in the Y-direction was smaller.

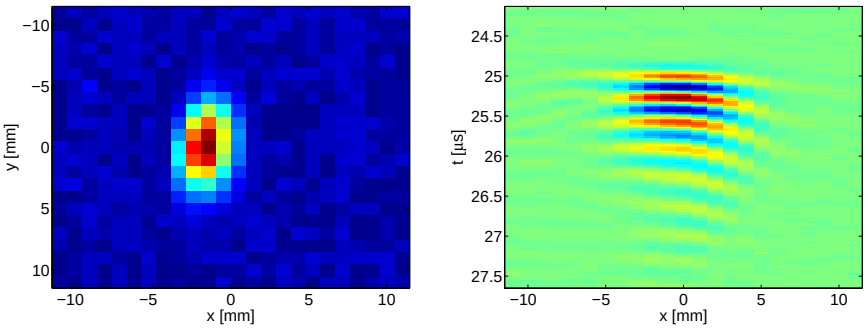

(a) Original C-scan

(b) Original B-scan

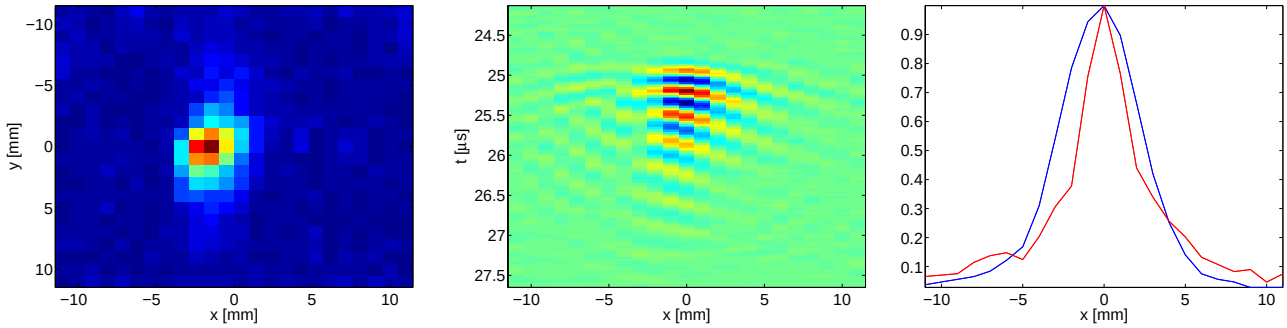

(c) ESAFT processed C-scan

(d) ESAFT processed B-scan

(e) Profile plots. Unprocessed (blue) and ESAFT processed (red).

Figure 3.19: Measured data. Single point-like target.

SAFT

As discussed in section 3.3.1 focusing with the SAFT algorithm is included for comparison. To work properly, SAFT requires small aperture emitting approximately spherical/cylindrical wavefront.

Measured data form the Section 3.3.4 was used here. The aperture used in the measurements was fairly large (12 mm in the direction that is focused) so it emitted waves that were far from spherical. Therefore, the SAFT method was expected to perform quite poorly and is included here for comparison only. From Figure 3.3.4 can be seen that no real improvement can be observed after processing with this method.

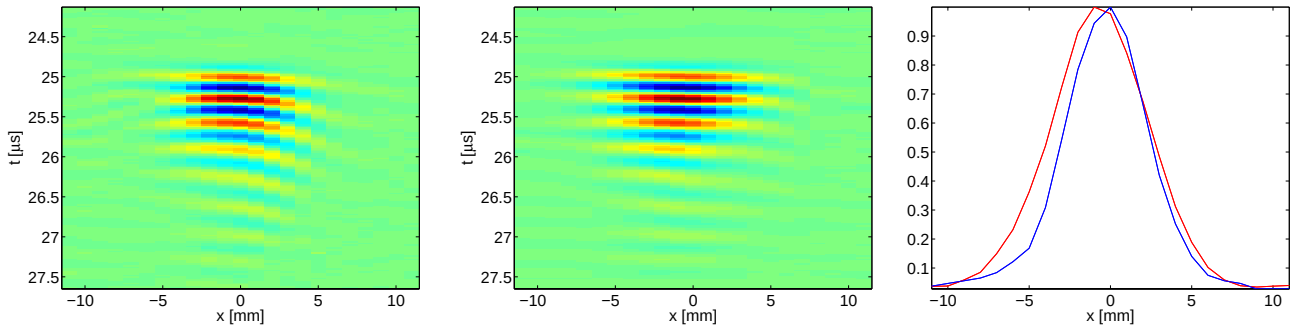

(a) Original B-scan

(b) SAFT processed B-scan

(c) Profile plots. Unprocessed (blue) and SAFT processed (red).

Figure 3.20: Measured data. Single point-like target.

3.4 Conclusions

An iterative ESAFT algorithm presented in the first part of this section has been tested using both simulated and real ultrasonic data. Application of this algorithm results in a slightely improved lateral resolution comparing with the ordinary ESAFT. However, its main advantage seems to be relative insensitivity to the initial parameters that have to be provided by the operator.

A successive application of ESAFT to the 3D ultrasonic data obtained for a phased array system has been demonstrated using both simulated and real data. Substantial resolution improvement was observed — elliptical responses to small scatterers produced by the array system focused in one dimension only took the form of smaller circular responses after the ESAFT processing.

Classical SAFT was applied to the real 3D data used for ESAFT demonstration, no improvements in resolution were noticed as it had been expected.

Bibliography

[1] T Stepinski, E Wennerstrm, F Lingvall, and P Wu. Inspection of copper canisters for spent nuclear fuel by means of ultrasound — NDE of friction stir welds, nonlinear acoustics, ultrasonic imaging. Technical Report TR-04-03, SKB, 2003.

[2] F. Lingvall, T. Olofsson, and T. Stepinski. Synthetic aperture imaging using sources with finite aperture: Deconvolution of the spatial impulse response. *J. Acoust. Soc. Am.*, 114(1):225–234, July 2003.

[3] F. Lingvall. A method of improving ovrtall resolution in ultrasonic array imaging using spatio-temporal deconvolution. *Ultrasonics*, 42:961–968, 2004.

[4] T Stepinski, F Lingvall, and P Wu. Inspection of copper canisters for spent nuclear fuel by means of ultrasound — nonlinear acoustics, synthetic aperture imaging. Technical Report TR-03-05, SKB, 2002.

[5] H. Lasota and R. Salamon. Application of time-space impulse responses to calculations of acoustic field in imaging systems. *Acoustic Imaging*, pages 493–512, 1980.

[6] T. Olofsson. Semi-sparse deconvolution robust to uncertainities in the impulse responses. *Ultrasonics*, 42:969–975, 2003.

[7] R. Fletcher. *Practical methods of optimization*. John Wiley & Sons Ltd., 2nd edition, 1987.

[8] J.A. Seydel. *Ultrasonic Synthetic-aperture Focusing Techniques in NDT*. Research Techniques for Nondestructive Testing. Academic Press, 1982.

[9] B. Piwakowski and K. Sbai. A new approach to calculate the field radiated from arbitrarily structured transducer arrays. *IEEE Trans. on Ultrasonics, Ferroelectrics, and Frequency Control*, pages 422–440, 1999.

Chapter 4

Nonlinear Ultrasonic NDE of Welds in Copper

by Ping Wu

4.1 Introduction

Friction stir welding (FSW), a novel welding method invented and patented by TWI [1], has been chosen as an alternative method for welding copper canister lids in parallel to electron beam welding, and tested on a full scale in the Canister Laboratory in Oskarshamn [2, 3].

The FSW has shown a few distinctive advantages, e.g., the welds have no porosity, no fume, no spatter, low shrinkage, low distortion even when the welds are long, and excellent mechanical properties as proven by fatigue, tensile and bend tests [4]. However, defects of different kinds in friction stir welds have also been observed [5]

- Lack of penetration;
- Wormholes;
- Kissing bonds;
- Faying surface defects;
- Root toe defects (defects at the toe or root of a weld)

Kissing bonds are a special type of lack-of-penetration defects in friction stir welds (FSWs) that are characterized by crack-type with contacting faces that are weakly or incompletely bonded. Since the welds are tightly closed by compressive residual stress [6], they are difficult to detect by means of linear ultrasonic inspection. Finding some effective NDE methods to inspect FSWs and to detect kissing bonds, thus, has become one of the goals in our research tasks since 2002. Our recent research on nonlinear ultrasonic has shown that nonlinear ultrasound can be a potential means to detect kissing bonds.

In addition to kissing bonds in FSWs, cracks and fatigue damages in materials and debonds in adhesive joints are similar defects with contacting faces. These defects often develop fast under periodical loading, and thus they are among the most dangerous defects. To cope with such defects, a variety of nonlinear ultrasonic techniques have been developed in the last decade. One of the common features in all the techniques is the use of power ultrasound to excite the defects so that the nonlinear behaviors of defects are present. These nonlinear behaviors have been exploited to detect such defects. These techniques can be classified in terms of wave generation and detection into two categories:

(1) propagation methods [7–20]

(2) modulation techniques [21–33]

In the propagation methods, a transmitter and a receiver are used separately. Usually, the former is a narrow-band transducer with a low center frequency (e.g., 0.5 MHz), and the latter is a broad-band transducer with a high center frequency (e.g., 1 MHz). A high power ultrasound generated by the transmitter is sent into the inspected material, and as it propagates in the material, it interacts with the defects in a nonlinear manner (e.g., in terms of clapping or kissing mechanism [17]). Then the ultrasound carrying the information on the nonlinear interaction is received by a high frequency transducer. The nonlinearity (the 2nd harmonic in many cases) is extracted commonly from the spectrum of the received signal, and used to diagnose defects. In the propagation methods, the ultrasound used can be either in through-transmission mode or in reflection mode. Since the nonlinearity carried by the propagating wave contains both the defect nonlinearity of our interest and the propagation nonlinearity (caused by imperfection of atomic lattices and not being of our interest) as well, the defect nonlinearity will be disturbed and can be too small to detect when the defects are small. Thus, the propagation methods are more adequate for inspecting large unbounded interfaces. This could be seen from the experimental results in the previous report and in this chapter.

In our previous report [6], it has been shown that the inspection of the copper specimens with the joints (bonded by hot isostatic pressing method) using the propagation method could not give any clear indications of defects, whereas the linear ultrasonic inspection (using pulse-echo method) indicated some defects in the joints. A possible reason for this is that the interface nonlinearity from the defects is not significantly larger than the propagation nonlinearity because the contacting areas of the defect's faces are small. As will be seen below in the this chapter, when the unbounded interfaces in the copper specimens are large, their ultrasonic nonlinearities are pronounced and thus become easy to detect.

In the modulation techniques, two transmitters are used, one generating a pumping wave with low frequency and high power, and the other producing a probing wave with high frequency and low amplitude. The probing wave is modulated by the pumping wave *at defects*, resulting in a modulated wave that is nonlinear, showing sidebands in the frequency spectrum. The modulated wave is then detected by a high frequency transducer. Since the generation of pumping and probing waves and the detection of modulated wave can be conducted using different setups, various modulation techniques have been developed, and they are relatively easy to modify to be adaptive to different circumstances. Since the high-frequency probing wave beam generated by the transducer can be focused and narrow, the local interaction of ultrasound with defects may become easier to capture using the narrow beam and, thus, the detection of defects could become more effective. Thus, the modulation methods are suited for detecting both large interfaces and local defects as well with appropriate setups. However, the methods are more complicated and more expensive to implement because they demand more complex equipment.

The research conducted here includes experimental and theoretical study of nonlinear ultrasonics of unbounded interfaces (mimicking kissing bonds) based on the ultrasonic propagation method, and an extensive literature investigation of nonlinear modulation techniques. Specifically, a few copper specimens that contain unbounded interfaces mimicking the kissing bonds were manufactured, and inspected using an ultrasonic propagation method and a material test system (INSTRON 8500). Theoretical study of the nonlinear responses of unbounded interfaces to ultrasound have been conducted. The interface is modeled as one (called rough interface) that consists of two *rough* surfaces. A theory is proposed for coping with ultrasonic response of such an rough interface. Two new setups for ultrasonic modulation techniques are under consideration that could be appropriate for detecting kissing bonds, and intended to use in the future work.

In this chapter, the theoretical and experimental results of our research on nonlinear ultrasonics of unbounded interfaces are presented. The detailed derivation of the theory is given in appendix 4.A. The simulations using the theory are presented in a intuitive manner in Section 4.2, and the measurements made on copper specimens are discussed in Section 4.3.

4.2 Simulations of Ultrasonic Nonlinearity of Unbounded Interfaces

A kissing bond or a contacting crack is a defect characterized by an interface of two rough surfaces that are unbounded but pressed into contact by some compressive stress. Detection of such defects using ultrasound is the purpose of the research. In this section, the simulations based on our theory (appendix 4.A) are presented in order to find out the characters of ultrasonic response of such an interface and to utilize to interpret measurement results.

An interface is a boundary separating two media and consists of two surfaces of the media. When the two surfaces are 'welded' together, they always move together when they are insonified by ultrasound. Such an interface is called perfect interface that possesses linear elasticity is not of the interest.

The interfaces of our interest are those that consist of two surfaces unbounded but in contact. Surfaces found in nature are observed to be rough in the microscopic scale. However, smooth surfaces can be good approximations of surfaces with small roughness under certain circumstances (e.g., when ultrasonic wave length is much larger than the roughness). When an interface is made up two smooth surfaces in contact (in an ideal case) (Fig. 4.1), it is called *unbounded smooth interface*. When an interface consisting of two rough surfaces in contact (in the real situation) (Fig. 4.2) it is referred to as *unbounded rough interface*. A smooth interface can be treated as a special and ideal case of the rough interface with a zero roughness. The unbounded interfaces of two surfaces in contact are also called imperfect interfaces, or contact interfaces. These two types of interfaces will be dealt with here.

When the response of an interface to ultrasound is nonlinear, the nonlinear degree of the response is referred to as ultrasonic nonlinearity. Such ultrasonic nonlinearity is also called interface nonlinearity in this report, in order to distinguish from propagation nonlinearity that arises from the nonlinear distortion of waves propagating in a medium.

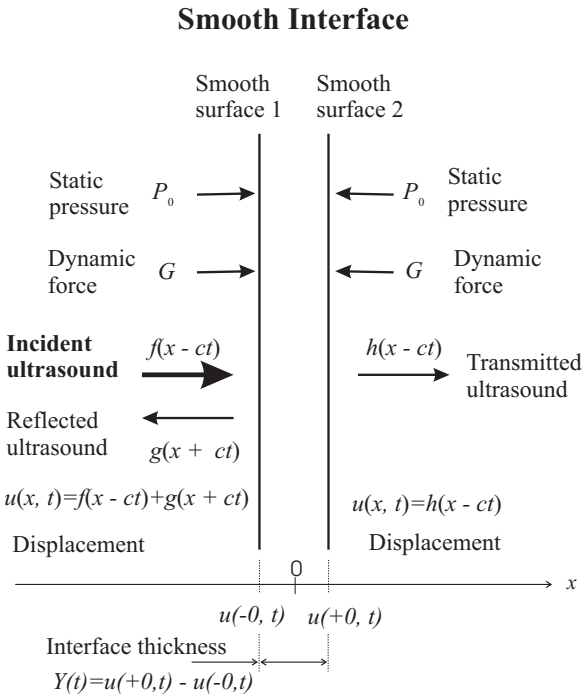

Figure 4.1: Geometry of a smooth interface.

An unbounded (contact) interface can not support tensile force. Thus, it manifests different elasticities (asymmetric elasticity) for tension and compression, e.g., smaller elasticity for tension and larger for compression. When such an interface is disturbed by an ultrasound (a dynamic driving force), the dynamic response of the interface to the ultrasound shows nonlinearity due to asymmetric elasticity.

The defects (e.g., kissing bonds or contacting cracks) that consist of rough surfaces in contact are well characterized by such an unbounded rough interface. It is why the nonlinearity of ultrasonic responses of defects has been tried to explore for the detection.

The interfaces (either smooth or rough) that we consider here are those that are planar and separate two semi-infinite media that are identical isotropic materials with linear elasticity. The problems of interest are the detection of nonlinearity of a planar interface to a normal incident plane wave. Such interface problems, although simple, can be good approximations to real situations, and the results can be used to qualitatively interpret some phenomena observed in

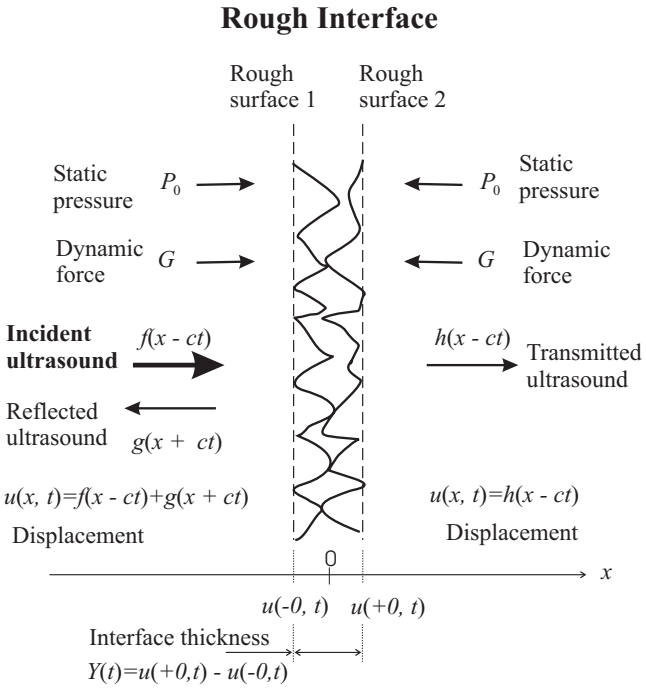

Figure 4.2: Geometry of a rough interface.

reality.

Theoretical study of the ultrasonic nonlinearity of unbounded interfaces has been made since several decades ago [34–37]. A theory was proposed by Richardson in 1979 [34] to deal with an unbounded smooth interface. Driven by newly-developed nonlinear ultrasonic techniques for detecting contacting cracks, theoretical research on the nonlinear interaction of ultrasound with rough interfaces has attracted much attention of NDE researchers recently [36, 37].

Here we have proposed a theory to treat rough interfaces, which is the extension of Richardson's theory. Our theory is more general and can be used to deal with rough interfaces and smooth interfaces as well. Two papers recently published in 2003 (one by Pecorari [37] and the other by Gusev *et al* [36]) concerned with the nonlinear ultrasonic interaction with rough interfaces were helpful for developing the present theory. In the first paper, the simple perturbation approach is used to solve the boundary value problem posed on the basis of the boundary conditions of contacting rough surfaces. The theoretical expressions on reflection and transmission at the rough interface are derived and the numerical results are presented. However, the theory is not suited for the calculation and analysis of waveforms as measured. In the second paper, the hysteresis in response of contacting rough interface to ultrasound is investigated. The theory derived seems to be complicated and difficult to implement numerically. Some qualitative analysis of ultrasonic response of a rough interface is made. No numerical results are given. The theory proposed here is easy to implement. It can be employed to calculate ultrasonic response of rough interfaces and transmitted waves. The calculated results are the waveforms that can be easily used to compare, analyze and interpret measurement results. The detailed derivation of our theory is given in appendix 4.A. The results presented in this section are calculated based on the theory.

4.2.1 Nonlinearity of an unbounded interface: the smooth interface case

Why does an unbounded interface manifest nonlinear elastic behavior under ultrasound? To answer the question, an example is first presented here in an intuitive way based on an unbounded smooth interface. The problem should be looked at and thought about on a microscopic scale. For example, a interface thickness is $1\mu m$, and a wavelength in copper at a frequency of 0.5 MHz is 9.2 mm, which is 9200 times the interface thickness.

Consider a planar smooth interface under ultrasonic insonification (Fig. 4.1). It is located at $x = 0$ and separates two identical elastic media. Assume that the interface gap is $Y(t)$ and it is closed initially, i.e., $Y(t \leq 0) = 0$, due to the pressing by an external static pressure P_0. Supposing that a plane ultrasonic wave with a particle displacement of sinusoid

$f(x - ct) = -A\sin(kx - \omega t)$

(where k is the wave number and ω is the angular frequency) impinges onto the interface, the corresponding ultrasonic force (*per unit area*, in Pascal), a dynamic driving force, imposed on the interface is (Eq. (4.22))

$F(t) = -(\lambda + 2\mu)\partial f(x - ct)/\partial x|_{x=0} = B\cos(\omega t)$

where $B = \rho c\omega A$. The examples of $f(x-ct)$ and $F(t)$ are shown in Fig. 4.3, when the ultrasound with $A = 0.4\ \mu m$ and $\omega = 2\pi F_0$ with $F_0 = 0.5 MHz$ impinges on an interface in a copper medium, and thus $B = 51.8\ MPa$. Note that from convention $F(t)$ is assumed to be positive for compression and negative for tension, and it has a $\pi/2$ phase difference from $f(x - ct)$.

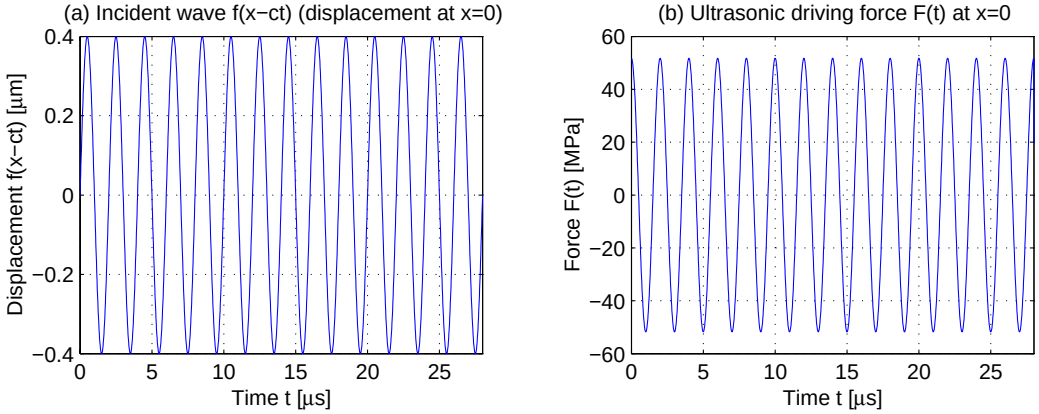

Figure 4.3: (a) Incident wave $f(x - ct)|_{x=0} = A\sin(\omega t)$, and (b) the corresponding ultrasonic force $F(t) = B\cos(\omega t)$ on the interface at $x = 0$, where $A = 0.4\ \mu m$, $B = \rho c\omega A = 51.8\ MPa$, and $\omega = 2\pi F_0$ with $F_0 = 0.5\ MHz$.

At the interface, the incident wave $f(x - ct)$ is reflected and transmitted. The resultant displacement, thus, becomes

$u(x, t) = f(x - ct) + g(x + ct)$

on the left hand side of the interface ($x < 0$), and

$u(x, t) = h(x - ct)$

on the right hand side ($x > 0$), where $g(x + ct)$ and $h(x - ct)$ the reflected and transmitted waves, respectively. The interface gap $Y(t)$ (referred to as interface opening displacement) in this case can be expressed as

$Y(t) = u(+0, t) - u(-0, t)$,

which changes with the relative motion of both sides of the interface, and the corresponding dynamic interfacial force present on the interface due to ultrasonic displacement $u(x, t)$ is (Eq. (4.29))

$G(t) = -(\lambda + 2\mu)\partial u(x, ct)/\partial x|_{x=0}$,
which is, in general, nonlinearly dependent on Y, i.e., $G = G(Y)$ is a nonlinear function of Y. The G(Y)-Y relation reflects the elastic characteristic of the interface. Note that the interfacial force $G(t)$ is different from the driving force $F(t)$.

If the ultrasonic force amplitude B is less than the static pressure P_0, i.e., $B < P_0$, then the interface keeps closed ($Y(t) = 0$) all the time. No nonlinear response of the interface will happen. This is not of our interest. When $B > P_0$, the interface can be open ($Y > 0$) and closed ($Y = 0$) when $F(t)$ changes alternately between tension and compression. When the interface changes from the open state to the closed, or vise versa, the interfacial force $G(Y)$ varies. The dependence of $G(Y)$ on Y is shown in Fig. 4.4, which shows that when the gap is closed ($Y(t) = 0$), $G(Y)$ may change in a range from P_0 to $F_{max} = B$, and when the gap is open ($Y(t) > 0$), $G(Y) = -P_0$. This can be interpreted as follows. When the driving force is in the compressive phase ($F(t) > 0$) or in the tensile phase ($F(t) < 0$) in which $|F(t)| < P_0$, the gap is closed ($Y(t) = 0$). In this case, $u(+0, t) = u(-0, t)$ and no reflection happens at the interface so that $u(-0, t) = u(+0, t) = f(-ct)$ and $G(Y) = F(t)$. When the driving force is in the tensile phase ($F(t) < 0$) but the relation $|F(t)| > P_0$ is satisfied, the gap will be opened ($Y(t) > 0$). In this case, the stress on the interface vanishes, i.e., $\sigma(+0, t) = \sigma(-0, t) = -G(Y) - P_0 = 0$ (Eq. (4.36)) so that $G(Y) = -P_0$. As $F(t)$ changes periodically from compression to tension, the interface will be closed open periodically. The differential equation governing the relative motion of the interface gap $Y(t) = u(+0, t) - u(-0, t)$ is of the form (Eq. (4.33) in appendix 4.A)

$$\rho c\dot{Y}(t) = 2G(Y) - 2F(t) \tag{4.1}$$

The interface opening displacement $Y(t)$ shows a nonlinear response to the ultrasonic force. In the present case, $F(t) = B\cos(\omega t)$, and $G(Y)$ nonlinearly depends on $Y(t)$, as schematically shown in Fig. 4.4. The above equation has a analytical solution.

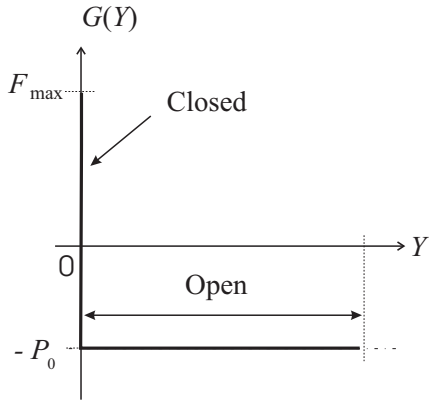

Figure 4.4: Dependence of dynamic interfacial force $G(Y)$ on interface opening displacement Y for a smooth interface.

For a closed interface, the interface opening displacement $Y(t)$ is

$$Y(t) = 0 \tag{4.2}$$

For an open interface, the interface opening displacement becomes (Eq. (4.48))

$$Y(t) = -2A\left[\eta\omega t + \sin(\omega t)\right] + C \tag{4.3}$$

where

$$\eta = P_0/B \tag{4.4}$$

and the arbitrary constant C is determined from the "initial" conditions at $t = t_i$ (Eq. (4.50)),

$$C(t_i) = Y(t_i) + 2A\left[\eta\omega t_i + \sin(\omega t_i)\right] \tag{4.5}$$

which needs to be calculated when the gap changes from the closed state to the open state.

An example of $Y(t)$ is shown in Fig. 4.5 (a) in which the results are calculated when the incident ultrasonic wave on the interface is one in Fig. 4.3 and the static pressure is $P_0 = B/2$=25.9 MPa. From Fig. 4.5 (a) it can be seen that the lower end of $Y(t)$ is flattened as the interface is closed. The transmitted wave (Eq. (4.40))

$h(x-ct)|_{x=0} = f(x-ct) + (1/2)Y(t-x/c)|_{x=0}$

is shown in Fig. 4.5 (b), and it is the wave that is received by a receiving transducer. The negative part of $h(t)$ becomes spiky. The nonlinear phenomenon can be easily seen from their spectra Fig. 4.5 (a') and (b'), in which the strong harmonics are present and the second harmonic level is -6.35 dB in $Y(t)$ and -13.93 dB in $h(t)$, respectively. When external static pressure P_0 changes, the nonlinearity differs, and accordingly, the harmonics are different. This can be seen in Fig. 4.6 that shows the variation of the second harmonic in $Y(t)$ (normalized by the incident wave amplitude A) with the ratio $P0/F(t)_{max}$. The figure demonstrates that the efficiency of second harmonic generation varies with the external pressure for a given ultrasonic amplitude A.

In reality, however, the surfaces constituting an interface are rough. As it will be seen below, the smooth interface theory gives overestimated nonlinearity.

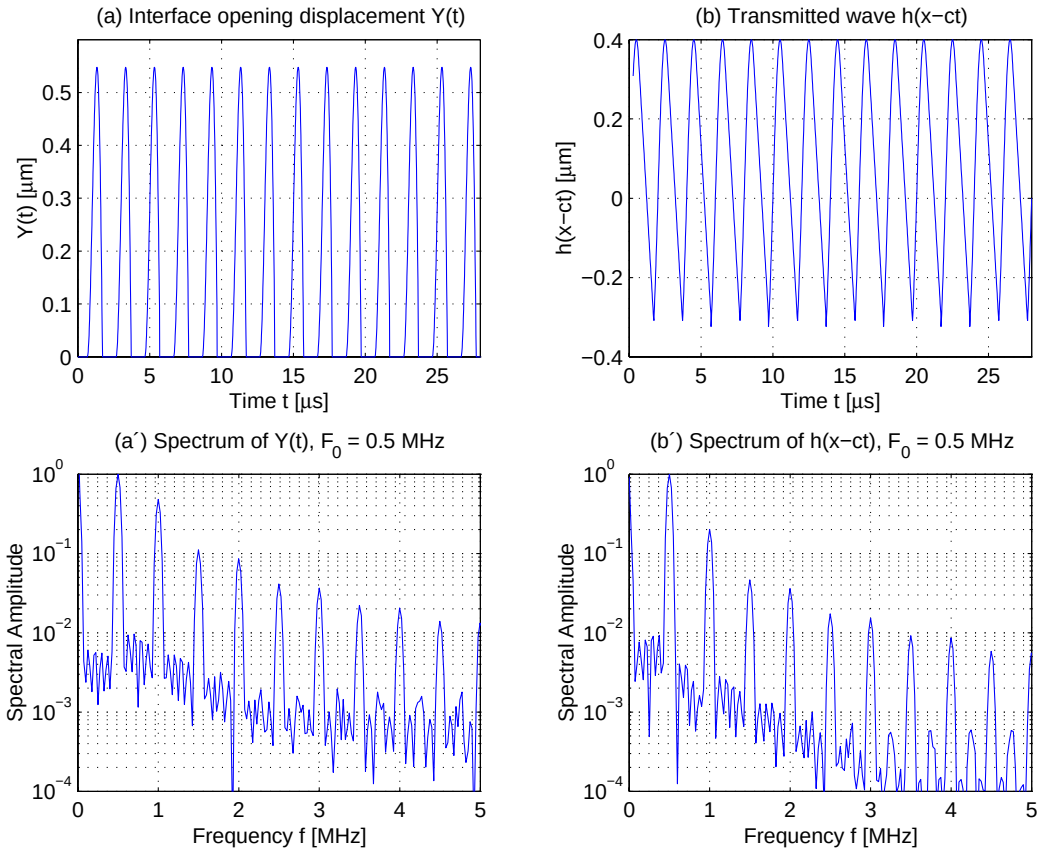

Figure 4.5: (a) Interface opening displacement $Y(t)$ and (a') its spectrum; (b) transmitted wave and (b') its spectrum. The second harmonic level is -6.35 dB in $Y(t)$ and -13.93 dB in $h(t)$.

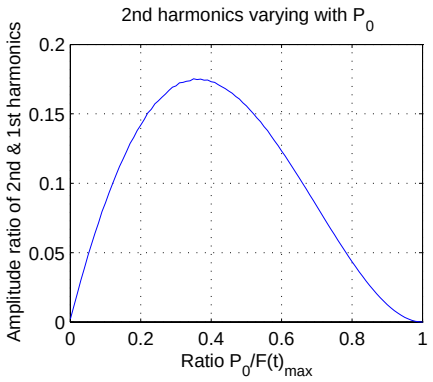

Figure 4.6: Variation of second harmonic generation with external static load. The amplitude is normalized by A the amplitude of incident wave.

4.2.2 Characteristics of rough surfaces and contacting rough interfaces

Surfaces are rough in a microscopic scale. This results in the real area of contact of two surfaces to be small compared to the nominal area. The real area of contact changes with external load. The topographical characteristics of rough surfaces are relevant to their behavior when pressed into contact. To establish the theory concerning the nonlinear response of an rough interface to an ultrasound, the properties of rough surfaces and their contact (the interface) shall be first understood.

Rough surfaces and their contacts are the subjects in solid mechanics [38, 39], tribology [40], geophysics [41]. The relevant theories are given in details in appendix 4.A.2.

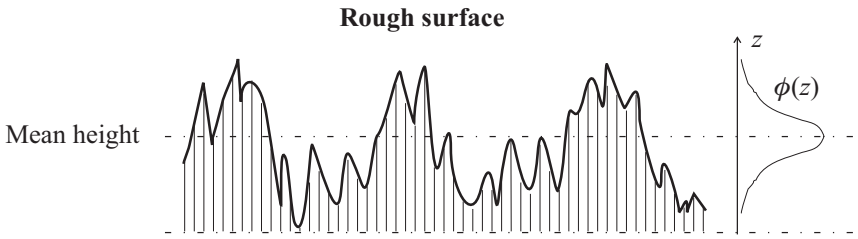

Figure 4.7: A rough surface.

A nominal flat rough surface contains a large number of asperities whose heights vary randomly (Fig. 4.7), and thus, the surface is characterized in a statistical manner by a distribution of heights of asperities, and a distribution of asperity radii, or equivalently, asperity curvatures. The surface heights are commonly estimated by Gaussian or inverted chi-square distributions [41–43]. The inverted chi-square distribution (Eq. (4.18)) is simply a chi-square distribution (Eq. (4.19)) with a variable substitution such that it has a zero mean and is skewed toward positive heights. The advantages of the inverted chi-distribution are (i) that it contains a parameter (n) controlling its skewness, and thus fits the topography data better than the symmetric Gaussian, and (ii) that it becomes zero when the surface heights are larger than the maximum height, as does a real surface [41].

A measure of average roughness is the root-mean-square (rms) or standard deviation σ of the surface hight from the mean hight line. The larger the deviation the bigger the roughness.

An example of inverted chi-square distribution is illustrated in Fig. 4.8(a) in which the rms roughness $\sigma = 0.23\ \mu m$ and the maximum height $z_{max} = 0.575\ \mu m$ are used in the probability

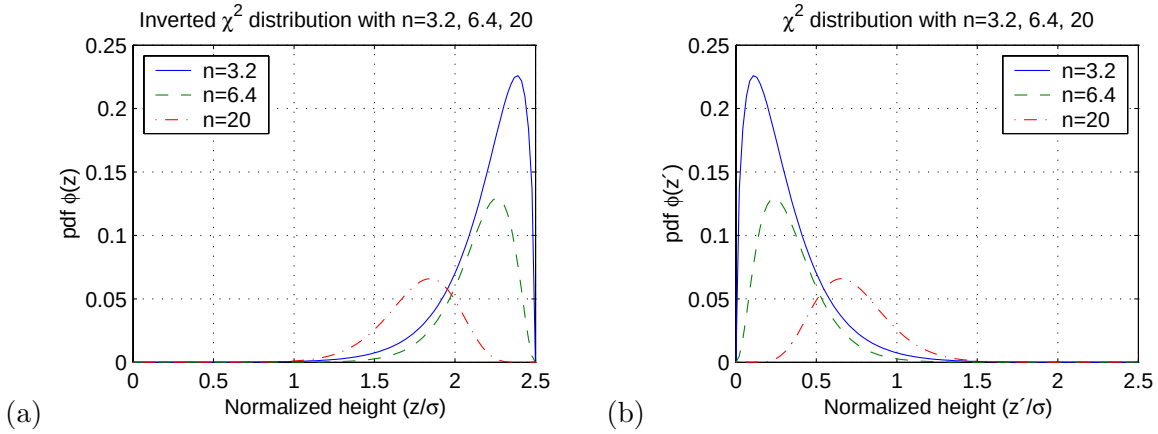

Figure 4.8: Probability density functions (pdf) of inverted chi-square (χ^2) distribution (a) and chi-square (χ^2) distribution (b) of asperity heights of a rough surface for different degrees of freedom (skewness parameter). The rms roughness is $\sigma = 0.23\ \mu m$ and the maximum height is $0.575\ \mu m$.

density function (pdf) $\phi(z)$. The figure shows that $\phi(z) = 0$ beyond the maximum height, $z > z_{max}$, and it is skewed toward the positive z.

If a substitution of $z' = z_{max} - z$ is made in $\phi(z)$ (i.e, the z-axis is reversed and then the origin is shifted to the right by z_{max}), the inverted chi-distribution $\phi(z)$ is converted to the chi-distribution $\phi(z')$. An example of the chi-square distribution is shown in Fig. 4.8(b) in which the rms roughness is $\sigma = 0.23\ \mu m$, and the pdf $\phi(z')$ at the maximum height is zero.

When two rough surfaces are pressed into contact to form a contact rough interface , the real area of contact of two surfaces is much smaller than the nominal area (Fig. 4.9 (a)), and the real area and the interface gap between the two surfaces change with external load P. The interface of two rough surfaces in Fig. 4.9 (a) can be converted into an equivalent interface between a rigid smooth surface and a composite deformable rough surface as shown in Fig. 4.9 (b). If the surface heights of the two rough surfaces in contact are characterized by inverted chi-square distributions $\phi(z_1)$ and $\phi(z_2)$ with rms roughnesses σ_1 and σ_2, respectively, the distribution of the composite surface heights is still described by an inverted chi-square distribution $\phi(z_s)$ (where $z_s = z_1 + z_2$) with rms roughness $\sigma_c = \sqrt{\sigma_1^2 + \sigma_2^2}$. Similarly, if z' is substituted for $z_{smax} - z_s$ in $\phi(z_s)$, then the inverted chi-distribution $\phi(z_s)$ is converted to the chi-distribution $\phi(z')$ (Fig. 4.8(b)). The equivalent interface in Fig. 4.9 (b) has been used to build the models for the contact of two rough surfaces [41–43].

4.2.3 Nonlinearity of contacting rough interfaces

To study the interaction of ultrasound with unbounded rough interfaces, the static model developed by Brown and Scholz [41] is first discussed. The model (Eq. (4.21)) describes the dependence of applied normal pressure P on the relative approach (the interface gap decrement) δ between two contacting surfaces. The contact of the surfaces in the model is assumed to be elastic without friction and hysteresis. The model is established using an equivalent rough interface that consists of a rigid smooth surface and a composite deformable rough surface (Fig. 4.10). The composite surface has a rms roughness $\sigma_c = \sqrt{\sigma_1^2 + \sigma_2^2}$ in which σ_1 and σ_2 are the rms roughnesses of the two rough surfaces in contact, and the surfaces heights are statistically characterized by the chi-square distribution $\phi(z')$ with use of the z'-axis in Fig. 4.10.

When an external pressure P is applied on the interface, the two surfaces approach to each

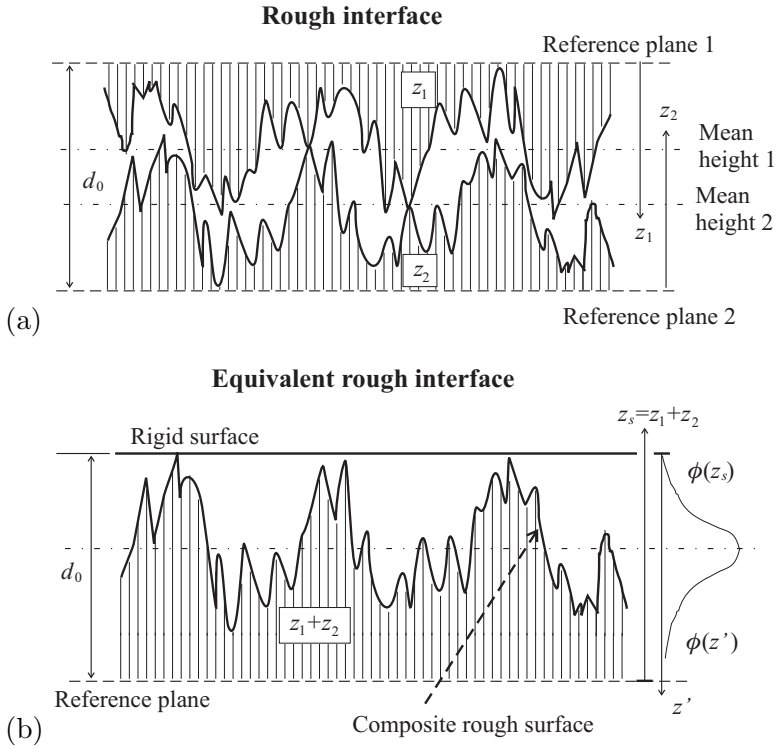

Figure 4.9: A rough interface. (a) Original interface, and (b) equivalent interface.

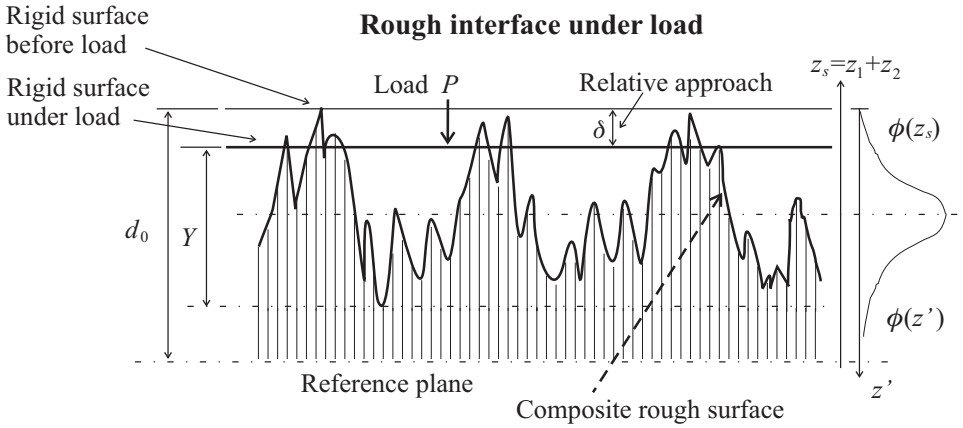

Figure 4.10: A rough interface under load.

other in amount of δ (relative approach) (Fig. 4.10). The relation between P and δ that is determined by Brown and Scholz's model (Eq. (4.21)) is shown in Fig. 4.11 in which the rms roughness of the composite surface is $\sigma_c = 0.23\ \mu m$ and the degrees of freedom used in $\phi(z')$ is 6.4. The figure shows that P increases with δ in a nonlinear manner. When δ increases until the gap is just completely closed, the applied normal pressure P reaches P_c. After that, δ will keep unchanged although P can further increase (Fig. 4.12). Since the curve shown in the figure has a feature of $P(\delta) \propto \delta^{\alpha}$, a polynomial of the form $P(\delta) = (a\delta)^{\alpha} - (b\delta)^{\beta}$ can be used for the fitting of $P(\delta)$. This can simplify the numerical calculation of differential equation governing the motion of interface gap (interface opening displacement) (Eq. (4.33)). In Fig. 4.11, the fitting polynomial is $P(\delta) = (8.65\delta)^{3.4} - (4.6\delta)^{4.3}$.

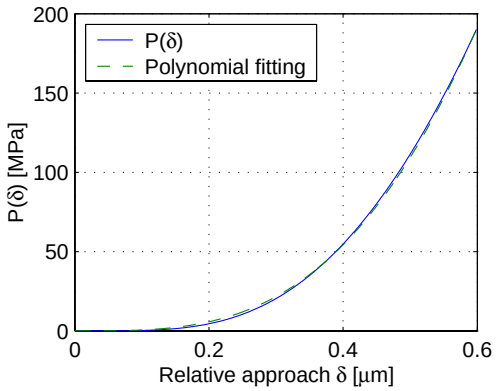

Figure 4.11: A rough interface deformation under external load. The relation between load and relative approach.

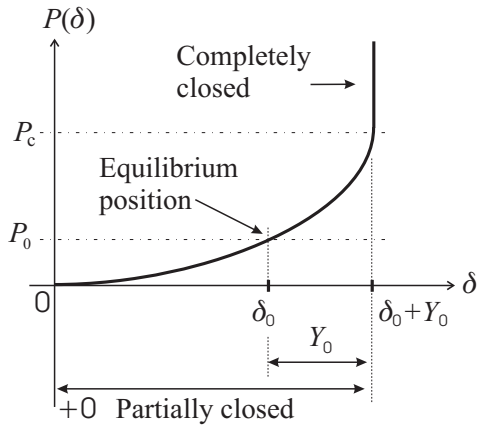

Figure 4.12: A rough interface under external load.

We now consider the response of a rough interface to ultrasound (refer to Fig. 4.2). Assume that the rough interface of two rough surfaces in contact has a thickness of $Y_0+\delta_0$ for hydrostatic pressure $P(\delta) = 0$ (Fig. 4.12). When the interface is pressed by a hydrostatic pressure $P_0 \neq 0$, and the relative approach is δ_0. In this case, the initial gap before ultrasonic disturbance becomes $Y(0) = Y_0$, and the dynamic interfacial force $G(Y_0) = 0$ is zero (Fig. 4.13 in which $F_c = P_c - P_0$). When an ultrasound that generates a driving force $F(t)$ strong enough to be able to completely close and open the interface impinges onto the interface, the interface may have three states: completely closed ($Y(t) = 0$) for $F(t) > F_c$, partially closed ($0 < Y(t) \leq Y_0 + \delta_0$) for $-P_0 < F(t) < F_c$, and completely open $Y > Y_0 + \delta_0$ for $F(t) < -P_0$. In the partially

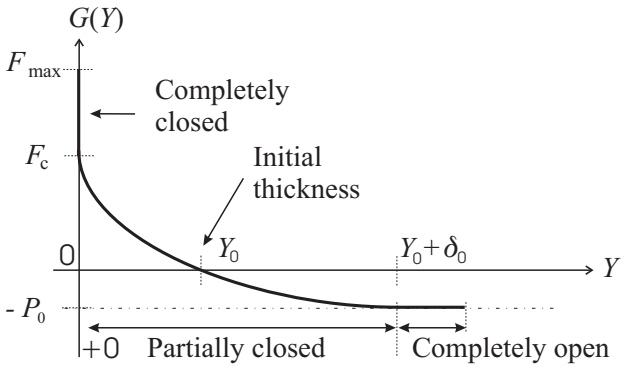

Figure 4.13: Dependence of dynamic interfacial force $G(Y)$ on interface opening displacement Y for a rough interface with a nonlinear stiffness constant.

closed state ($0 < Y(t) \leq Y_0 + \delta_0$), $G(Y)$ is usually nonlinearly dependent on Y because a rough interface has a nonlinear interfacial stiffness constant. The whole relation of $G(Y)$ with Y in the presence of all three states is illustrated in Fig. 4.13. The $G(Y) - Y$ curve can be formed by flipping from left to right the $P(\delta) - \delta$ curve in Fig. 4.12, and then shifting down by P_0. In this case, $F_c = P_c - P_0$ Fig. 4.13. Note that in the present sign convention $G(Y)$ is positive for compression on the interface because $G(Y) = -\sigma(0,t) = -(\lambda + 2\mu)\partial u(0,ct)/\partial x$ (Eq. (4.29)). Thus, when $G(Y)$ increases in the positive direction (compressive phase), Y decreases.

The differential equation governing the relative motion of the interface gap $Y(t) = u(+0,t) - u(-0,t)$ (referred to interface opening displacement) is also of the form

$$\rho c\dot{Y}(t) = 2G(Y) - 2F(t) \tag{4.6}$$

But the $G(Y) - Y$ curve in general looks like one in Fig. 4.13.

Here we consider a simple case in which the rough interface in the partially-closed state ($Y_0 < Y \leq Y_0 + \delta_0$) has a linear interfacial stiffness constant κ_0 so that

$$G(Y) = -\kappa_0[Y(t) - Y_0] \tag{4.7}$$

which is illustrated in Fig. 4.14. In this case, Eq. (4.6) will have an analytical solution.

For the completely closed interface, one has

$$Y(t) = 0 \tag{4.8}$$

When the interface is completely open ($Y(t) > Y_0 + \delta_0$), $Y(t)$ can be determined as in the smooth interface case, in the following manner

$$Y(t) = -2A\left[\eta\omega t + \sin(\omega t)\right] + C_o \tag{4.9}$$

where the arbitrary constant C_o can be found from the "initial" conditions at $t = t_i$,

$$C_o(t_i) = Y(t_i) + 2A\left[\eta\omega t_i + \sin(\omega t_i)\right] \tag{4.10}$$

For the partially-closed interface ($0 < Y(t) < Y_0 + \delta_0$), we have

$$Y(t) = \exp(-\xi t)\left\{-2\omega A\frac{\exp(\xi t)}{\xi^2 + \omega^2}[\xi\cos(\omega t) + \omega\sin(\omega t)] + C_p\right\} + Y_0 \tag{4.11}$$

where

$$\xi = \frac{2\kappa_0}{\rho c} \tag{4.12}$$

and C_p is determined by the "initial" conditions at $t = t_j$,

$$C_p(t_j) = \exp(\xi t_j)\left\{[Y(t_j) - Y_0] + \frac{2\omega A}{\xi^2 + \omega^2}[\xi\cos(\omega t_j) + \omega\sin(\omega t_j)]\right\} \tag{4.13}$$

which need be calculated when the interface gap changes either from the open state to the partially-closed state or from the completely-closed state to the partially-closed state provided the states are present.

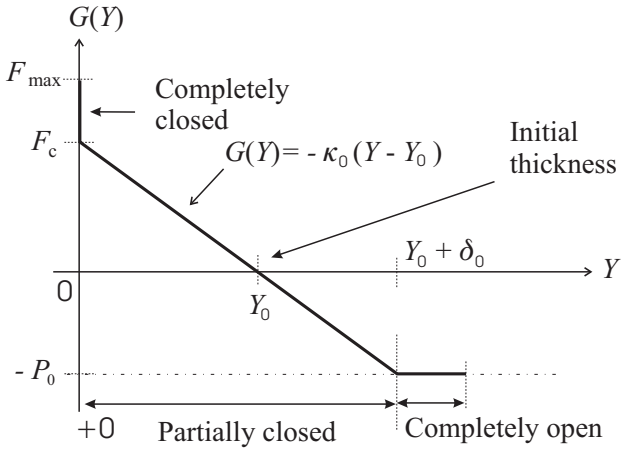

Figure 4.14: Dependence of dynamic interfacial force $G(Y)$ on interface opening displacement Y for a rough interface with a linear stiffness constant κ_0.

The previous study has shown that the ultrasonic response of a smooth interface only has two cases: either in the completely closed state ($Y(t) = 0$) when $B < P_0$ or varying alternately between the closed state and the open when $B > P_0$. For a contact rough interface, its ultrasonic response is different and more complicated, and may have the following cases:

- (i) always in the completely closed state, and no nonlinearity occurs;
- (ii) varying alternately between the completely-closed state and the partially-closed;
- (iii) varying only in the partially-closed state, and no nonlinearity occurs;
- (iv) varying alternately between the partially-closed state and the completely-open; and
- (v) varying alternately from the completely-closed state, to the partially-closed and then to the completely-open, or vise versus.

P_0 is an important factor that may change the response case of an interface, and thus changes the efficiency of nonlinearity generation. For example, for a fixed ultrasonic force amplitude B, when $P_0 > B$ is satisfied, the interface will be never completely opened, but it may have a nonlinear response if the ultrasonic force can completely close the gap; when $P_0 < B$ is satisfied, the interface may be completely open. In this case, the ultrasonic nonlinearity can become stronger.

Let us now look at two examples showing how a rough interface responds to a sinusoidal ultrasound $f(x - ct) = A\sin(\omega t)$. The rough interface is assumed to have a linear stiffness constant $\kappa_0 = 8.632 \times 10^{13}[N/m^3]$, and the $P(\delta) - \delta$ relation is shown in Fig. 4.15(a). The interface gap of the two rough surfaces in contact is 0.6 μm for $\delta = 0$.

In the first example, the incident wave is $f(x-ct) = A\sin(\omega t)$ with $A = 0.2\ \mu m$ and $\omega = 2\pi F_0$ with $F_0 = 0.5\ MHz$ and the ultrasonic force is $F(t) = B\cos(\omega t)$ with $B = \rho c\omega A = 25.9\ MPa$.

The external static pressure is assumed to be $P_0 = B/2 = 12.95\ MPa$ so that the relative approach is $\delta_0 = 0.15\ \mu m$, and $Y_0 = 0.45\ \mu m$. The $G(Y) - Y$ relation is illustrated in 4.15 (b).

Since $B = 25.9\ MPa < F_c = 38.92\ MPa$ for which the interface just starts to be completely-closed, the ultrasonic response of the interface in this example is the case (iv) in which the gap varies alternately between the partially-closed state and the completely-open. The calculated results for $Y(t)$ and $h(t)$ are shown in Fig. 4.16. The nonlinearity can be seen from the spectra in Figs.Fig. 4.16(a') and (b') in which the second harmonic level is -17.65 dB in $Y(t)$ and -17.73 dB in $h(t)$. Comparing to the smooth interface case, the second harmonic level in $Y(t)$ in this example is much smaller (11.3 dB smaller), but the one in $h(t)$ is 3.8 dB lower.

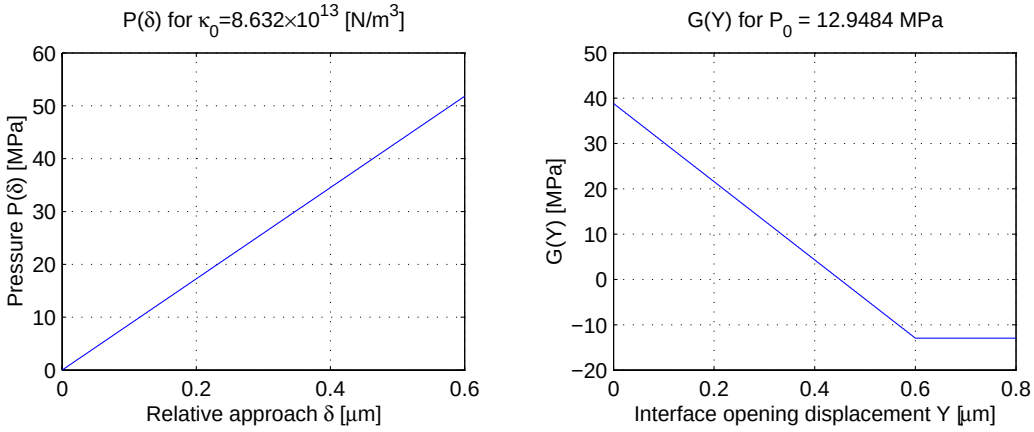

Figure 4.15: (a) the relation between the static load and the relative approach for $\kappa_0 = 8.632 \times 10^{13}[N/m^3]$, and (b) dependence of dynamic interfacial force $G(Y)$ on interface opening displacement Y for $P_0 = B/2 = 12.95\ MPa$, in which $Y_0 = 0.45\ \mu m$.

In the second example, the incident wave has an amplitude of $A = 0.4\ \mu m$ and a frequency is still $F_0 = 0.5\ MHz$ (Fig. 4.3 (a)) and the amplitude of the ultrasonic force becomes $B = 51.8\ MPa$ (Fig. 4.3 (b)). The external static pressure takes on $P_0 = B/2 = 25.9\ MPa$, which results in a relative approach $\delta_0 = 0.30\ \mu m$, and $Y_0 = 0.30\ \mu m$. The $G(Y) - Y$ relation is illustrated in 4.17 (b).

Since $B = 51.8\ MPa > F_c = 25.92\ MPa$ in this example, the ultrasonic response of the interface is the case (v) in which the gap varies alternately from the completely-closed state, to the partially-closed and then to the completely-open. The calculations of $Y(t)$ and $h(t)$ are shown in Fig. 4.18. From the figure it can be seen that the second harmonic level is -14.43 dB in $Y(t)$ and -15.46 dB in $h(t)$, which are larger, respectively, than the those in the first example. This indicates a more severe nonlinearity in this example. It should be specially mentioned that the negative part of the waveform, $h(t)$, in Fig. 4.18(b) becomes spikier and prolonged in comparison with that in Fig. 4.16(b). Comparing to the smooth interface case, the second harmonic level in $Y(t)$ in this example is 8.08 dB smaller, and the one in $h(t)$ is only 1.53 dB lower.

Both examples have shown that the estimation of nonlinearity for $Y(t)$ from the smooth interface model is much higher than from the rough interface model. Since all the surfaces in real situations are rough, the smooth interface model may overestimate the ultrasonic nonlinearity of a rough surface.

4.2.4 Conclusions

The ultrasonic responses of smooth and rough interfaces to ultrasound have been investigated.

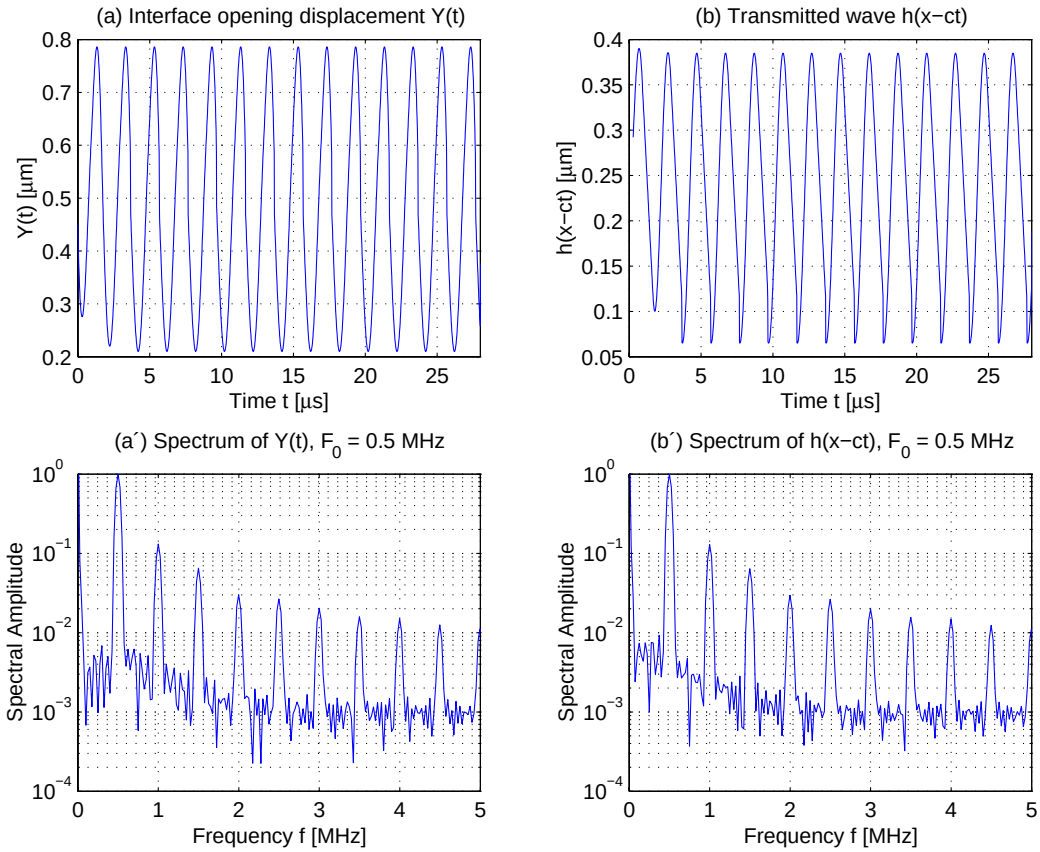

Figure 4.16: (a) Interface opening displacement $Y(t)$ and (a') its spectrum; (b) transmitted wave and (b') its spectrum. The second harmonic level is -17.65 dB in $Y(t)$ and -17.73 dB in $h(t)$.

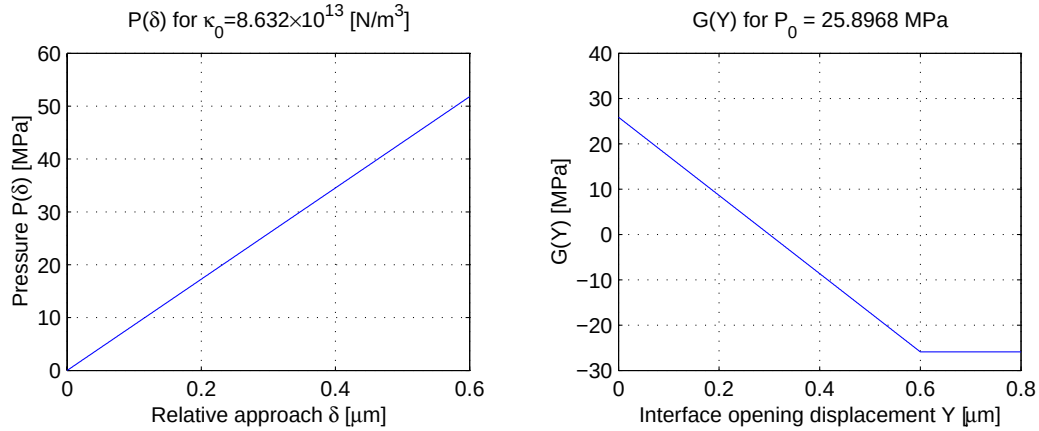

Figure 4.17: (a) the relation between the static load and the relative approach for $\kappa_0 = 8.632 \times 10^{13}[N/m^3]$, and (b) dependence of dynamic interfacial force $G(Y)$ on interface opening displacement Y for $P_0 = B/2 = 25.9\ MPa$, in which $Y_0 = 0.45\ \mu m$.

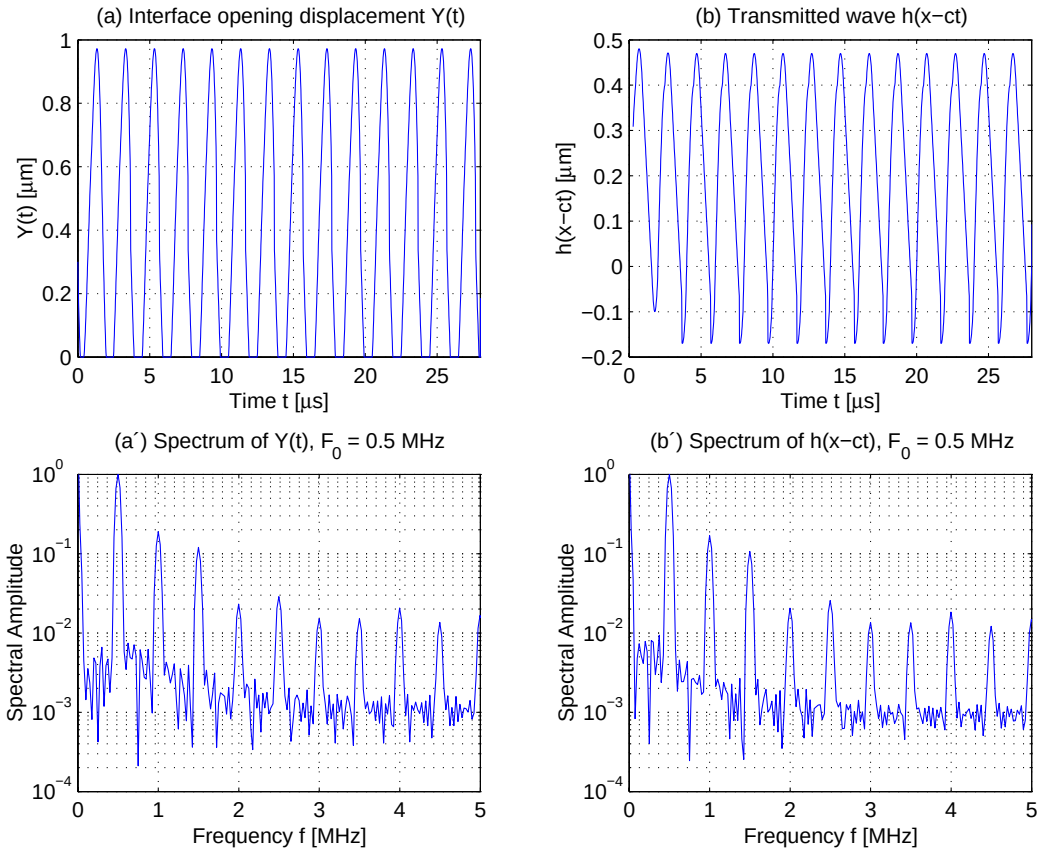

Figure 4.18: (a) Interface opening displacement $Y(t)$ and (a') its spectrum; (b) transmitted wave and (b') its spectrum. The second harmonic level is -14.43 dB in $Y(t)$ and -15.46 dB in $h(t)$

The ultrasonic response of a smooth interface only has two cases:

- (i) in the completely closed state ($Y(t) = 0$) when $B < P_0$; and no nonlinearity occurs;
- (ii) varying alternately between the closed state and the open when $B > P_0$.

The ultrasonic nonlinearity from a smooth interface may be produced only from the second case. An example for a smooth interface has shown that

- When the interface changes alternately from the open state to the close, the waveform of $Y(t)$ becomes flattened in the lower end due to the gap closing, and thus, the higher harmonics (normalized) result (Fig. 4.5(a) and (a')). The waveform of $h(t)$ becomes spiky in the lower part, and the higher harmonics (normalized) are comparatively lower (Fig. 4.5(b) and (b')).

For a contact rough interface, its ultrasonic response is much more complicated and may have the following cases:

- (i) always in the completely closed state ($Y(t) = 0$), and no nonlinearity happens;
- (ii) varying alternately between the completely-closed state and the partially-closed ($0 \leq Y(t) < Y_0 + \delta_0$);
- (iii) varying only in the partially-closed state ($0 < Y(t) < Y_0 + \delta_0$), and no nonlinearity occurs;
- (iv) varying alternately between the partially-closed state and the completely-open; and
- (v) varying alternately from the completely-closed state, to the partially-closed and then to the completely-open, or vise versus. In this case, the nonlinearity can become largest.

The ultrasonic nonlinearity from a rough interface may be generated from three cases, i.e., cases (ii), (iv) and (v), depending on the ratio P_0/B. Two examples for a rough interface under different static pressure P_0 have shown that

- in the case that the interface varies alternately between the partially-closed state and the completely-open; the waveform of $Y(t)$ will not be flattened in the lower end because the gap is not close, and the waveform of $h(t)$ will be smooth in the lower part (Fig. 4.16); and
- in the case that the interface varies alternately from the completely-closed state, to the partially-closed and then to the completely-open, or vise versus; in this case, the waveform of $Y(t)$ will become flattened in the lower end due to the gap closing, and the waveform of $h(t)$ will become spiky in the lower part (Fig. 4.18).
- in the case that the interface varies alternately between the completely-closed state and the partially-closed; the waveform of $Y(t)$ may become flattened in the lower end due to the gap closing, and the waveform of $h(t)$ may become spiky in the lower part; if a rough interface has a nonlinear interface stiffness (as shown in Fig. 4.13), the harmonic generation might be smaller than a rough interface with a linear interface stiffness;

These features of the waveform of $h(t)$ in the rough surface case can be seen in the measurement results below.

Comparing the results for a smooth surface and a rough surface demonstrates that the ultrasonic nonlinearity from a smooth surface is larger than that from a rough interface under

the same ratio of static pressure to ultrasonic force amplitude $P_0/B = 2$. This may indicate that the theory with the smooth surface assumption yields overestimated nonlinearity. Since surfaces observed in nature are rough, the rough interfaces give more accurate description of real contact interfaces.

4.3 Measurements of Ultrasonic Nonlinearity of Unbounded Interfaces

4.3.1 Experimental setups and copper specimens

The experimental setup for the measurements of ultrasonic nonlinearity of unbounded interfaces is shown in Fig. 4.19. It is composed of two parts: ultrasonic inspecting system and static pressure supplying system.

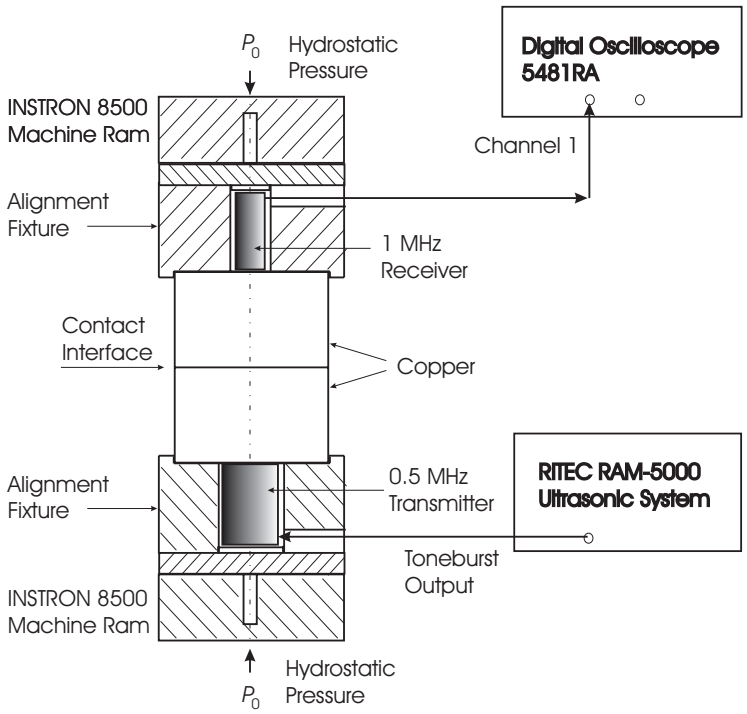

Figure 4.19: INSTRON 8500.

The former system includes a 0.5-MHz narrow-band transmitter and a 1-MHz broad-band receiver (both made by Valpey Fishers Co., USA), RITEC RAM-5000 Ultrasonic System, and a digital oscilloscope (Inifiniium Oscilloscope 54810AR made by Agilent Technology). The RITEC System and the 0.5-MHz transmitter provides a high-power ultrasound tone-burst, and the 1-MHz receiver and the oscilloscope are used to receive and record the signals that propagate through the inspected specimen.

The latter system consists of INSTRON 8500 material dynamic testing machine (Fig. 4.20) and the alignment fixtures, and it supplies static pressure P_0 on inspected copper specimens.

The inspected specimens (Fig. 4.21) are four copper cylinders (all with a diameter of 70 mm or a cross-section area of $Ac = 3848mm^2$) that are named CuCyl 0, CuCyl 1, CuCyl 2, and CuCyl 3 from left to right in the photo. Specimen CuCyl 0 is a cylinder without interface, and is used for measurement reference. The other three specimens are all consist of two pieces of cylinders with polished surfaces, and thus each specimen contains an unbounded interface with two surfaces pressed into contact by INSTRON. The geometry (H_1/H_2) of CuCyl 1 is 60/30 mm, CuCyl 2 is 40/50 mm and CuCyl 3 is 60/60 mm.

In the measurements, the RITEC outputs that excited the 0.5-MHz transmitter were 14-cycle tone-bursts all with a 0.5-MHz frequency ($F_0 = 0.5MHz$) but with various amplitudes (E_0) ranging from 60 to 2260 volts (peak to peak). Note that the amplitude of the RITEC

Figure 4.20: INSTRON 8500.

Figure 4.21: Cu cylinders.

output is changeable in 101 different levels, i.e., from 0 to 100, which correspond to 60 to 2285 volts for the 0.5-MHz transmitter. The 11 amplitudes used in the measurements corresponded to levels, 0, 10, 20, ..., and 99. The static pressure P_0 from INSTRON were applied to the inspected specimen in the force range from 1 to 100 kN, which correspond to a pressure range from 2.6 to 26.0 MPa on the interface with an area of $Ac = 3848mm^2$. For each specimen, a series of measurements were made using different tone-burst amplitudes E_0 and static pressure P_0. The waveforms were recorded with the digital oscilloscope. The spectra were calculated using MATLAB, with Hamming window applied on the waveforms.

4.3.2 Results and discussions

The measurements were made on all the four copper specimens. But only the results of measurements made on CuCyl 0 (without interface) and CuCyl 3 (with an interface at a 60-mm depth) under different excitations (E_0) from the RITEC and static pressure (P_0) from the INSTRON are selected and presented here.

To investigate the ultrasonic nonlinearity of the contact interface, let us first compare some representative results from CuCyl 0 (Fig. 4.22) and CuCyl 3 (Fig. 4.23) for $P_0 = 30kN$ and various values of E_0. The results are presented in waveform-spectrum pair. The waveforms (with Hamming window applied) are on the left column, and their spectra on the right. More measurement results are available in appendix 4.B

From the figures, we may observe that

- at the lowest RITEC output amplitude $E_0 = 60v_{pp}$, no obvious harmonics can be seen in the spectra from both specimens (Figs. 4.22(a') and 4.23(a'));
- when the output amplitude increases to $E_0 = 206v_{pp}$, a pronounced second harmonic and a small third harmonic for the interfaced specimen CuCyl 3 can be seen (Fig 4.23(b')), but for CuCyl 0 only a third harmonic is visible (Fig. 4.22(b'));
- when E_0 increases to 934 and 2260 v_{pp}, the second harmonic for CuCyl 3 (Figs. 4.23(e') and (k')) increases faster and is larger than for CuCyl 0 (Figs. 4.22(e') and (k')), but the third harmonics for CuCyl 3 are smaller;
- an interesting difference between the two specimens' results can be seen in the waveforms. The waveforms for CuCyl 3 become asymmetric for E_0=934 and 2260 v_{pp}, with the lower part becomes spikier and prolonged, which is the feature that can be observed from the theoretical calculation of transmitted wave $h(t)$ in Fig. 4.18 (b) in which the interface gap is much squashed by a large static pressure P_0 and the ultrasonic force was so strong as to be able to completely close the gap in compressive periods; while the waveform for CuCyl 0 becomes asymmetric for 2260 v_{pp}, with the lower part becoming round and shortened, which is a typical feature of wave propagation nonlinearity.

To study how the static pressure P_0 affects the ultrasonic nonlinearity of the interface, we now compare with the measurement results under static pressure $P_0 = 100kN$.

From the spectra in Figs. 4.24 (CuCyl 0) and 4.25 (CuCyl 3), we can observe that the second and third harmonics for CuCyl 3 grow in a similar way to those for CuCyl 0, and that the second harmonics for CuCyl 3 are much smaller compared with those when $F_0 = 30kN$ in Fig. 4.23. This may be interpreted qualitatively from the preceding theory. For large $P_0 = 100kN$, the ultrasonic force is not strong enough to open the interface so that the interface nonlinearity is becomes small, and the waveforms for both specimens show similar asymmetry: round and shortened negative part.

After having observed and compared the results from two specific cases, we shall now get a broader view on the effects of P_0 and E_0 on the ultrasonic response of an unbounded interface. The second and third harmonics normalized by the corresponding fundamentals are presented as E_0 varies for fixed P_0 (Figs. 4.26 and 4.28) or as P_0 varies for fixed E_0 (Figs. 4.27 and 4.29). Please be noted the difference of the scales in the figures, when comparing the results.

Comparing the results in Fig. 4.26 (for CuCyl 0) and in Fig. 4.28 (for CuCyl 3), one can see that

- the second harmonic for CuCyl 0 in all the cases increases monotonically as E_0 increases, while the one for CuCyl 3 first increases and then decreases as E_0 increases so that a maximum is present and its position depends on P_0;
- when P_0 increases up to 50 kN, there appeases a valley (minimum), which might be caused by propagation nonlinearity that becomes significantly large for large E_0 and cancels part of the interface nonlinearity (due to the different asymmetries of two types of nonlinearities)
- for large static pressure, e.g., $P_0 = 80, 100kN$, the second harmonic for CuCyl 3 change with E_0 in quite a similar manner to that for CuCyl 0, which may reveals that the interface nonlinearity decreases rapidly as P_0 becomes large;
- the second harmonics for CuCyl 3 are dramatically larger when $P_0 = 30$ and 40 kN.

Comparing the results in Figs. 4.36 (for CuCyl 0) and 4.38) (for CuCyl 3), we can see that

- the second harmonics for CuCyl 0 do not vary so much with P_0 when $E_0 \leq 934 v_{p-p}$, while the ones for CuCyl 3 all have a maximum at about $P_0 = 7.8\ MPa$ (equivalent to 30 kN because P_0 is normalized by $Ac = 3848 mm^2$, the cross-section area of the copper cylinder). This may possibly be explained in the way that for the 30 KN pressure the initial interface opening displacement (initial interface gap) $Y(0) = Y0$ could be at such a 'middle' point in the $G(Y) - Y$ curve (see Fig. 4.14 or Fig. 4.13) that the rough interface may change alternately from the completely-closed state, to the partially-closed and then to the completely-open, or vise versus so that the nonlinearity occurs most efficiently (i.e., $Y(t)$ distorts in both ends of the $G(Y) - Y$ curve).
- for large $E_0 = 2284\ v_{p-p}$, the second harmonics for CuCyl 0 increases quickly with P_0 in the beginning and stays at a high amplitude level in the range of $P_0 = 18$ to 26 MPa)

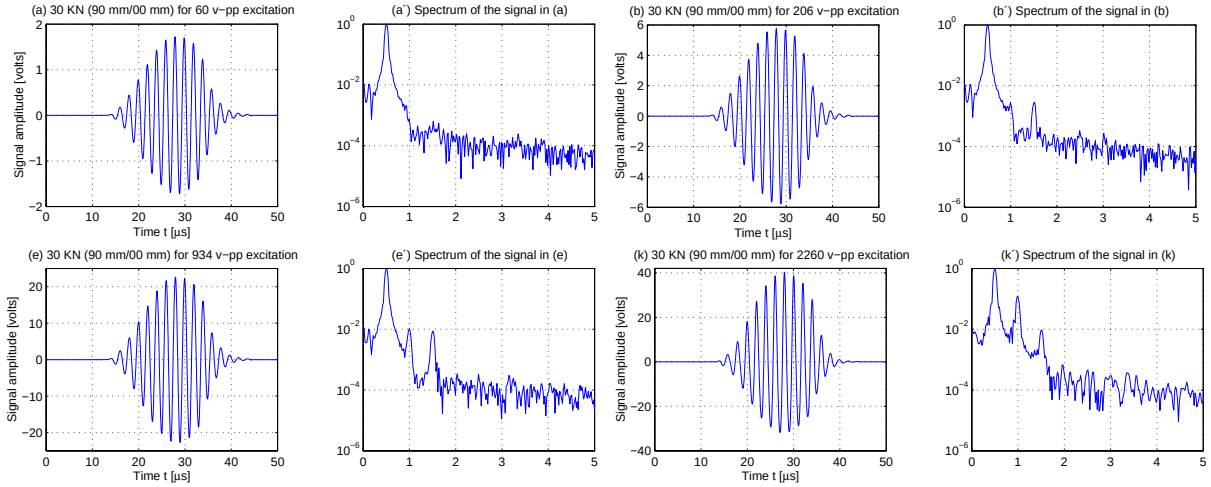

Figure 4.22: Measurements on Specimen CUCYL 0 for the tone-burst excitations with different amplitudes V when the external force is P_0=30 KN. (a) to (k) Waveforms, and (a) to (k) their spectra.

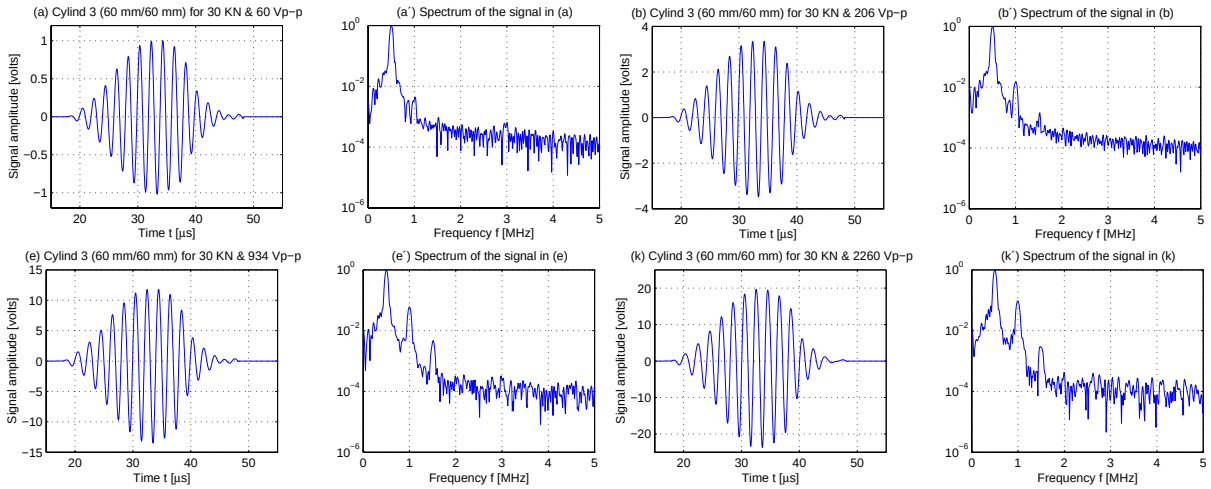

Figure 4.23: Measurements on Specimen CUCYL 3 for the tone-burst excitations with different amplitudes V when the external force is P_0=30 KN. (a) to (k) Waveforms, and (a) to (k) their spectra.

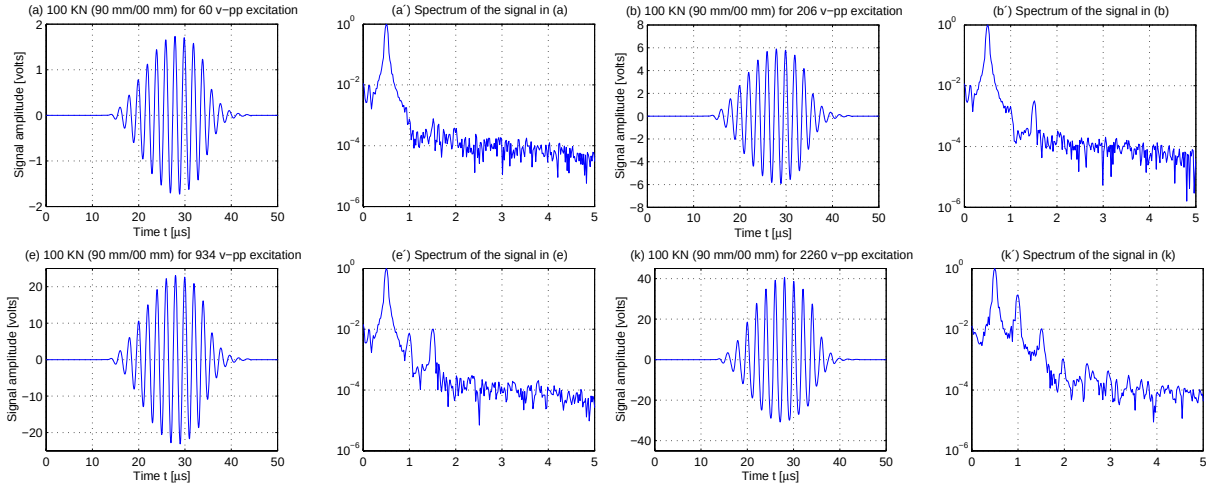

Figure 4.24: Measurements on Specimen CUCYL 0 for the tone-burst excitations with different amplitudes V when the external force is P_0=100 KN. (a) to (k) Waveforms, and (a) to (k) their spectra.

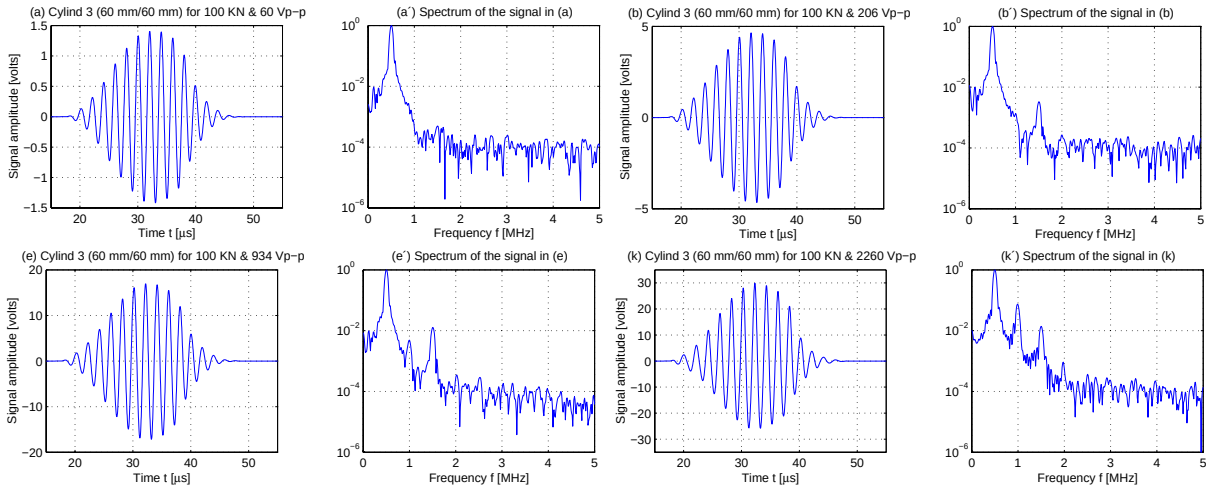

Figure 4.25: Measurements on Specimen CUCYL 3 for the tone-burst excitations with different amplitudes V when the external force is P_0=100 KN. (a) to (k) Waveforms, and (a) to (k) their spectra.

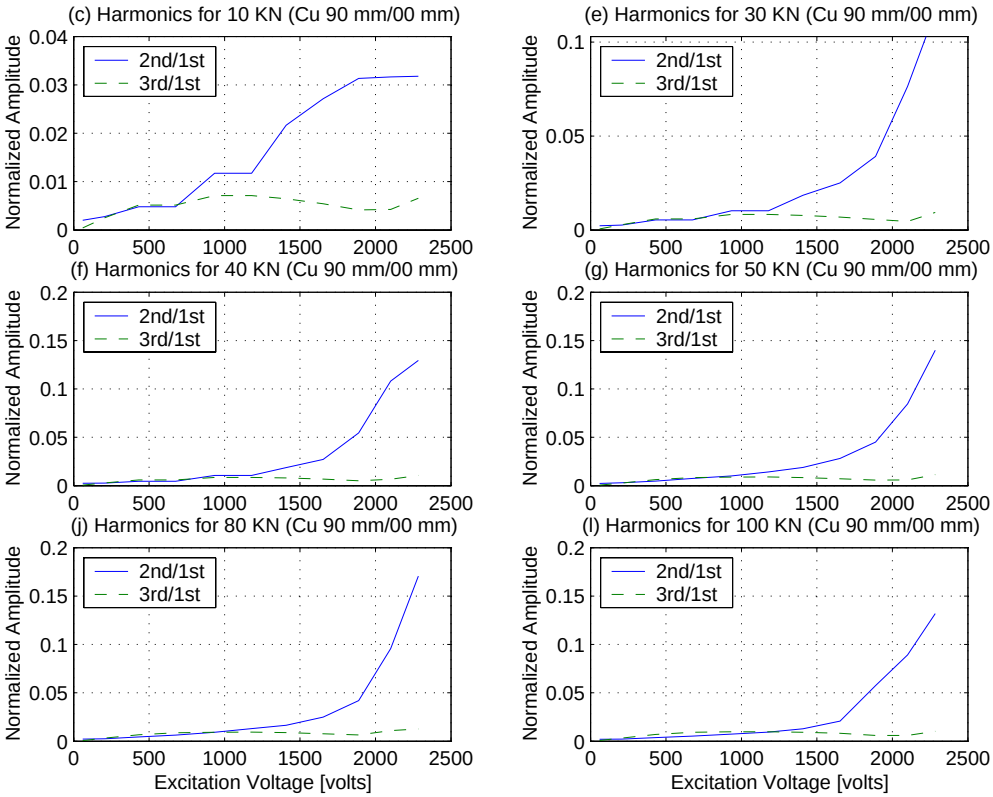

Figure 4.26: Variation of second (−) and third (- -) harmonics (normalized by the fundamental) with tone-burst excitation for external static pressures: (c) 10 KN, (e) 30 KN, (f) 40 KN, (g) 50 KN, (j) 80 KN, and (l) 100 KN.

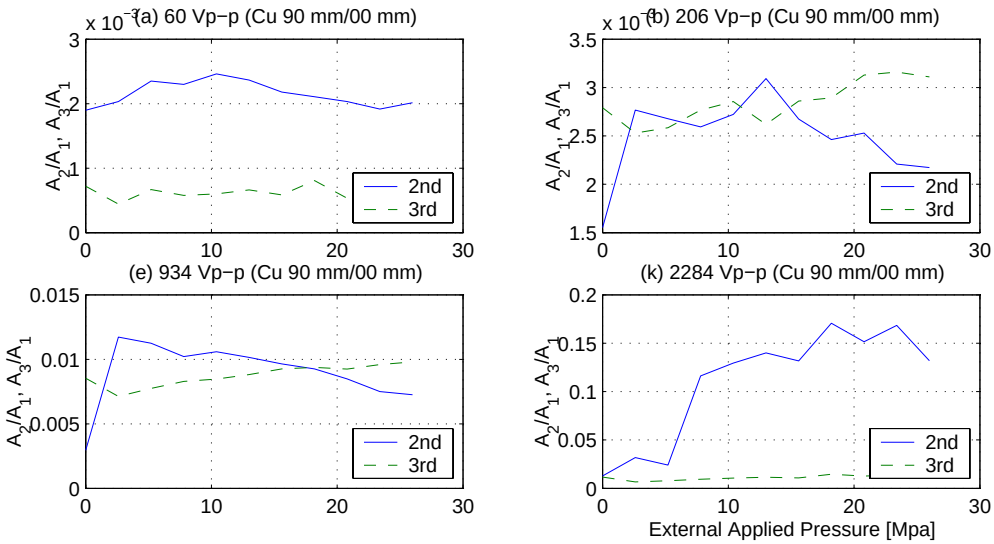

Figure 4.27: Variation of second (−) and third (- -) harmonics (normalized by the fundamental) with external static pressure for different tone-burst excitations. (a) 60 Vp-p, (b) 206 Vp-p, (e) 934 Vp-p, and (k) 2284 Vp-p.

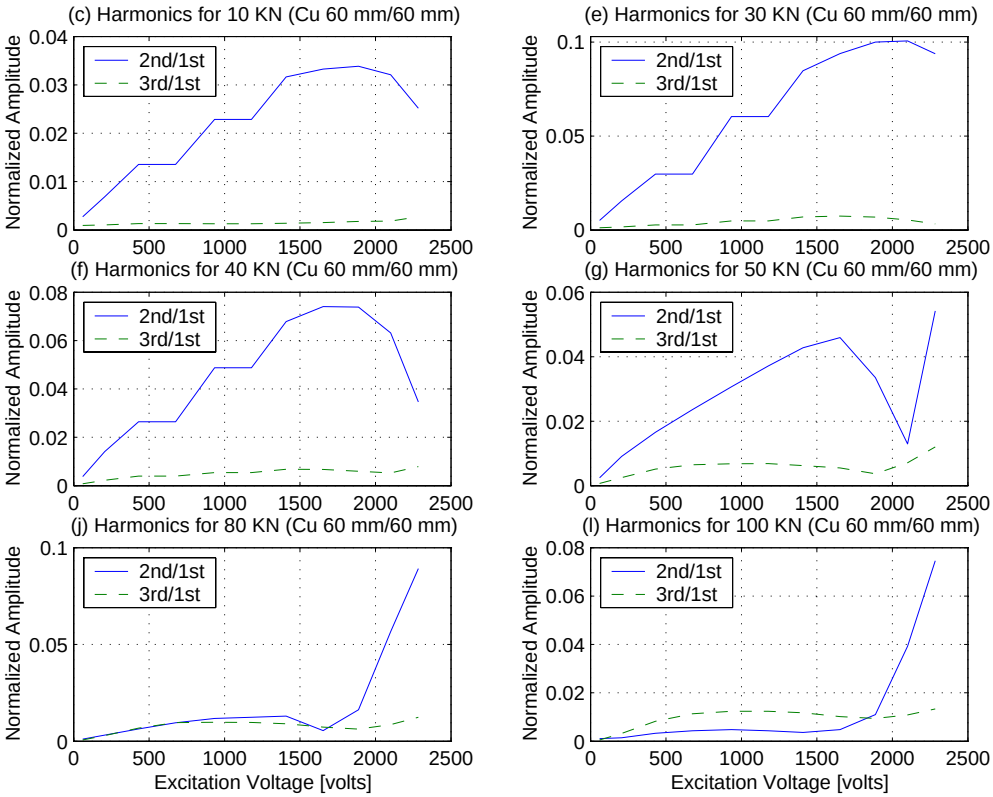

Figure 4.28: Variation of second (−) and third (- -) harmonics (normalized by the fundamental) with tone-burst excitation for external static pressures: (c) 10 KN, (e) 30 KN, (f) 40 KN, (g) 50 KN, (j) 80 KN, and (l) 100 KN.

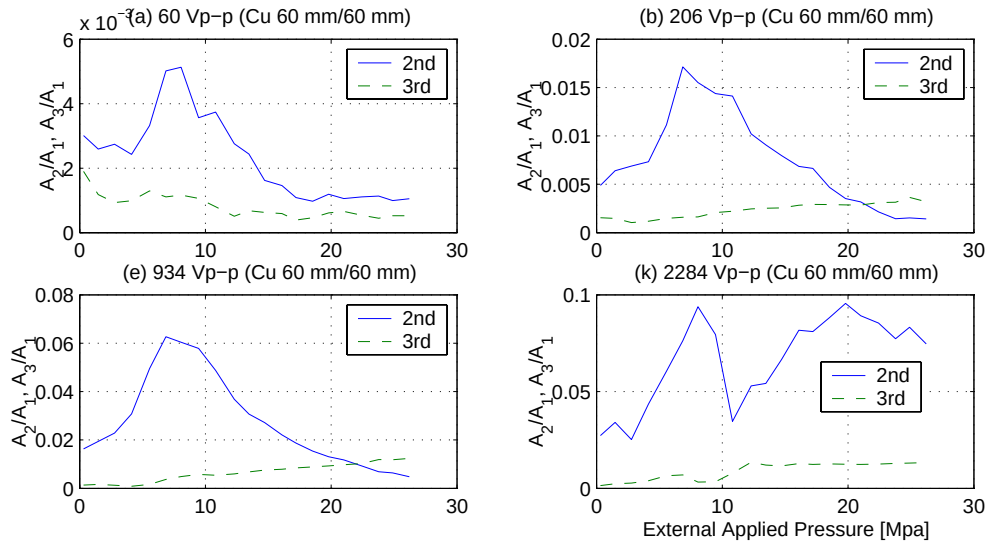

Figure 4.29: Variation of second (−) and third (- -) harmonics (normalized by the fundamental) with external static pressure for different tone-burst excitations. (a) 60 Vp-p, (b) 206 Vp-p, (e) 934 Vp-p, and (k) 2284 Vp-p.

4.4 Discussions and Conclusions

Ultrasonic nonlinearity of interfaces of two surfaces in contact have been investigated theoretically and experimentally. A theory has been proposed that can be used to deal with ultrasonic nonlinearity of rough interfaces and smooth surfaces as well. It is the extension of Richardson's theory for unbounded smooth interfaces. The calculations of ultrasonic interface nonlinearity have been made for both smooth and rough interfaces. The results show that the smooth interface assumption yields overestimated nonlinearity than the rough interface assumption (mainly based on the comparison of second harmonics). Since surfaces observed in nature are rough, the rough interface (consisting of two rough surfaces in contact) is a more accurate model for unbounded interfaces, kissing bonds in FSWs and joints, contact cracks in materials. For a contact rough interface, its ultrasonic response may have five different cases:

- (i) always in the completely closed state, and no nonlinearity occurs;
- (ii) varying alternately between the completely-closed state and the partially-closed;
- (iii) varying only in the partially-closed state, and no nonlinearity occurs;
- (iv) varying alternately between the partially-closed state and the completely-open; and
- (v) varying alternately from the completely-closed state, to the partially-closed and then to the completely-open. In this case, the generation of interface nonlinearity might be most efficient.

These cases have shown to be useful in the interpretation of the measurement results.

Experimental investigation of nonlinear ultrasonics of interfaces have been conducted based on ultrasonic propagation technique. The measurements were made on four copper specimens (one without interface, and the others all with an interface) under different external static pressure P_0 and ultrasonic driving amplitudes E_0. Observation of the measurement results have revealed that

- large nonlinearity from contact interfaces are present under a modest static pressure P_0 (e.g., 7 to 9 MPa).
- the static pressure P_0 has a large impact on the nonlinear behavior of a contact interface. Under a modest P_0 (e.g., 6 to 12 MPa), the interface shows strong nonlinear behavior, which is demonstrated by the presence of a strong second harmonic in the spectrum. Under a large P_0, the interface nonlinearity becomes small because the interface is constrained in the case of varying from the completely-closed state to the partially-closed. There seems to exist a value of P_0 on which the second harmonic (nonlinearity) becomes largest. On this value the ultrasonic response of the rough interface may mostly occur in the case (v) in which the interface varies alternately from the completely-closed state, to the partially-closed and then to the completely-open.
- the interface nonlinearity (from a contact interface) and the wave propagation nonlinearity results in different asymmetries in waveforms: namely, the asymmetry due to interface nonlinearity results in the spiky and prolonged negative part of waveforms, which coincides with our theoretical prediction; the asymmetry because of the propagation nonlinearity leads to the round and shortened negative part.

The present research has shown that the propagation technique seems to work well to detect the nonlinearity of contact interfaces. However, the kissing bonds usually have contact rough

interfaces with *a small area*. In this case, this propagation technique may not work so well. Our previous report [6] had shown that nonlinear behavior of small contacts in the copper specimens (bonded with hot isostatic pressing technique) could not be detected using this technique.

An extensive literature study of modulation techniques that has been conducted by us has shown that nonlinear ultrasonic modulation technique can be more appropriate for detecting kissing bonds since the probing wave beam can be focused, and thus the local interaction of ultrasound with defects is easier to capture and detect.

In the future work, the first intention is to develop a nonlinear ultrasonic modulation technique suitable for detecting kissing bonds and contact cracks with small local interfaces, and the second is to extend the proposed theory (for contact interfaces) to treat kissing bonds, contact cracks and fatigue damages that are local interfaces and find more features on interface nonlinearity to characterize the defects.

Bibliography

[1] The Welding Institute (TWI). *Friction Stir Welding.* http://www.twi.co.uk /j32k /unprotected/band_1/fswintro.html.

[2] Svensk Kärnbränslehantering AB. *FUD (Program för forskning, utveckling och demonstration) 2001.* EnaInfo Tryck, Enköping, Sweden, 2001.

[3] Svensk Kärnbränslehantering AB. *Svensk Kärnbränslehantering AB, Activities 2002.* Tryckindustri Information AB, Solna, Sweden, 2003.

[4] The Welding Institute (TWI). *Friction Stir Welding.* http://www.twi.co.uk /j32k /unprotected/band_1/fswproc.html.

[5] A. Lammare and M. Moles. Ultrasound phased array inspection technology for the evaluation of friction stir welds. *Proc. of the 15th World Conference on Nondestructive Testing*, Roma, Italy. October 15-21 2000.

[6] T. Stepinski, F. Lingvall, E. Wennerström, and P. Wu. Inspection of copper canisters for spent nuclear fuel by means of ultrasound - nonlinear acoustics, synthetic aperture imaging. Technical Report TR-04-03, SKB, 2004.

[7] O. Buck, W. L. Morris, and J. M. Richardson. Acoustic harmonic generation at unbonded interfaces and fatigue cracks. *Appl. Phys. Lett.*, 33(5):371–373, September 1978.

[8] W. L. Morris, O. Buck, and R. V. Inman. Acoustic harmonic generation due to fatige damage in high-srtength aluminum. *J. Appl. Phys.*, 50(11):6737–6741, November 1979.

[9] L. Adler and P. B. Nagy. Second order nonlinearities and their applications in nde. *Rev. Progr. QNDE*, 10:1813–1820, 1991.

[10] P. B. Nagy. Excess nonlinearity in material containing microcracks. *Rev. Progr. QNDE*, 13:1987–1994, 1994.

[11] P. B. Nagy. Fatigue damage assessment by nonlinear ultrasonic material characterization. *Ultrasonics*, 36:375–381, 1998.

[12] K.-Y. Jhang and K.-C. Kim. Evaluation of material degradation using nonlinear acoustic effect. *Ultrasonics*, 37:39–44, 1999.

[13] K.-Y. Jhang. Application of nonlinear ultrasonics to the nde of material degradation. *IEEE Trans. Ultrason. Ferroelectr.Freq. Contr.*, 47(3):540–548, 2000.

[14] H. Jeong, S.-H. Nahm, K.-Y. Jhang, and Y.-H. Nam. Nondestructive method for estimation of the fracture toughness of crmov rotor steels based on ultrasonic nonlinearity. *Ultrasonics*, 41:543–549, 2003.

[15] I. Yu. Solodov, A. F. Asainov, and Ko sel Len. Non-linear saw reflection: experimental evidence and nde apllications. *Ultrasonics*, 31(2):91–96, 1993.

[16] I. Yu. Solodov. Nonlinear nde using contact acoustic nonlinearity. *1994 IEEE Ultrason Symp.*, pages 1279–1283, 1994.

[17] I. Yu. Solodov. Ultrasonics of non-linear contacts: propagation, reflection and nde-applications. *Ultrasonics*, 36:383–390, 1998.

[18] I. Yu. Solodov, N. Krone, and G. Busse. Can: an example of nonlclassical acoustic nonlinearity in solids. *Ultrasonics*, 40:621–625, 2002.

[19] C. J. Brotherhood, B. W. Drinkwater, and S. Dixon. The detectablity of kissing bonds in adhesive joints using ultrasonic techniques. *Ultrasonics*, 41:521–529, 2003.

[20] C. J. Brotherhood, B. W. Drinkwater, and F. J. Guild. The effect of compressive loading on the ultrasonic detectability of kissing bonds in adhesive joints. *J. of NDE*, 21(3):95–104, 2003.

[21] A. E. Ekimov, I. N. Didenkulov, and V. V. Kazakov. Modulation of torsional waves in a rod with a crack. *J. Acoust. Soc. Am.*, 106(3):1289–1292, 1999.

[22] D. Donskoy, A. Sutin, and A. Ekimov. Nonlinear acoustic interaction on contact interfaces and its use for nondestructive testing. *NDT&E International*, 34:231–238, 2001.

[23] Hui Xiao and P. Nagy. Enhanced ultrasonic detection of fatigue cracks by laser-induced crack closure. *J. Appl. Phys.*, 83(12):7453–7460, 1998.

[24] Z. Yan and P. Nagy. Thermo-optical modulation for improved ultrasonic fatigue crack detection in ti-6al-4v. *NDT&E Interbnational*, 33:213–223, 2000.

[25] Z. Yan and P. Nagy. Thermo-optical modulation of ultrasonic surface waves for nde. *Ultrasonics*, 40:689–696, 2002.

[26] K. E-A. Van Den Abeele, P. A. Johnson, and A. Sutin. Nonlinear elastic wave spectroscopy(news) techniques to discern material damage, part i: nonlinear wave modulation spectroscopy (nwms). *Res. Nnodestr Eval*, 12:17–30, 2000.

[27] K. E-A. Van Den Abeele, P. A. Johnson, and A. Sutin. Nonlinear elastic wave spectroscopy(news) techniques to discern material damage, part ii: single-mode nonlinear resonace acoustic spectroscopy (nwms). *Res. Nnodestr Eval*, 12:31–42, 2000.

[28] K. E-A. Van Den Abeele, A. Sutin, J. Carmeliet, and P. A. Johnson. Micro-damage diagnostics using nonlinear elastic wave spectroscopy. *NDT&E International*, 34:239–248, 2001.

[29] V. V. Kazakov, A. Sutin, and P. A. Johnson. Sensitive imaging of an elastic nonlinear wave-scattering source in a solid. *Appl. Phys. Lett.*, 81(4):646–648, 2002.

[30] V. Yu. Zaitsev, P. Sas, and M. Wevers. Nonlinear modulation methods of structural damage detection based on dissipative nonlinear effects. *Proc. ISMA 25 Int. Conf. Noise Vibration Eng*, pages 233–242, Sept. 13-15 2000.

[31] V. Yu. Zaitsev, V. Gusev, and B. Castagnède. Observation of the "luxemburg-gorky effect" for elastic waves. *Ultrasonics*, 40:627–631, 2002.

[32] V. Yu. Zaitsev, V. Gusev, and B. Castagnède. Luxemburg-gorky effect retooled for elastic waves: a mechanism and experimental evidence. *Phys. Rev. Lett.*, 89:105502–1–4, 2002.

[33] V. Zaitsev, V. Gusev, B. Castagnède, and P. Sas. Micro-damage detection using a modulaion technique based on dissipative nonlinear effects. *Forum Acusticum*, Sevilla, Spain, September 16-20, 2002.

[34] J. M. Richardson. Harmonic generation at an unbonded interface – i. planar interface between semi-infinite elastic media. *Int. J. Engng. Sci.*, 17:73–85, 1979.

[35] J.-M. Baik and R. B. Thompson. Ultrasonic scattering from imperfect interfaces: a quasi-static model. *J. Nondestr. Eval*, 4:177–196, 1984.

[36] V. Gusev, B. Castagnède, and A. Moussatov. Hysteresis in response of nonlinear bistable interface to continuously varying acoustic loading. *Ultrasonics*, 41(8):643–654, 2003.

[37] C. Pecorari. Nonlinear interaction of plane ultrasonic waves with an interface between rough surfcaes in contact. *J. Acoust. Soc. Am.*, 113(6):3065–3072, June 2003.

[38] K. L. Johnson. *Contact mechanics*. Cambrige University Press, New York, 1985.

[39] J. R. Barber and M. Ciavarella. Contact mechanics. *Int. J. Solids Struct*, 37:29–43, 2000.

[40] B. Bhshan. *Micro/Nano Tribology*. CRC Press, Boca Raton, 1999.

[41] S. R. Brown and C. H. Scholz. Closure of random elastic surfaces in contact. *J. Goephys. Res*, 90(B7):5531–5545, June 1985.

[42] J. A. Greenwood and J. B. P. Williamson. Contact of nominally flat surfaces. *Proc. R. Soc. Lond. A*, 295:300–319, 1966.

[43] A. Baltazar, S. I. Rokhlin, and C. Pecorari. On the relationship between ultrasonic and micro-mechanical properties of contacting rough surfaces. *J. Mech. Phys. Solids*, 50:1397–1416, 2002.

4.A Theory on ultrasonic nonlinearity of contact interfaces

In this appendix a detailed derivation of the theory is given that describes the nonlinearity of an unbounded rough interface under ultrasonic plane wave disturbance. The interface under consideration is planar and consists of two contacting rough surfaces of identical elastic materials. The theory is the extension of Richardson's theory [34] that is only valid for the smooth interface case, and it can be used for both rough and smooth interfaces.

4.A.1 General Consideration

Since the problem of interest is concerned with the response of a rough interface to an ultrasonic plane wave, it can be formulated in terms of a one-dimensional wave motion. In this case the equation of motion in terms of particle displacement $u = u(x,t)$ in an isotropic elastic medium with Lamé constants λ and μ can be written as

$$\rho \frac{\partial^2 u}{\partial t^2} = \frac{\partial \sigma}{\partial x} \tag{4.14}$$

where ρ is the density, and $\sigma = \sigma(x,t)$ is the stress. When an external hydrostatic compressive pressure P_0 (that is uniform and nonnegative) is present in the medium, the stress-strain relation may be assumed to be of the form

$$\sigma = (\lambda + 2\mu)\epsilon - P_0 = \kappa \frac{\partial u}{\partial x} - P_0 \tag{4.15}$$

where $\epsilon = \partial u/\partial x$ is the strain, and $\kappa = \lambda + 2\mu$ is the elastic constant. In Eq. (4.15), the reference state of zero strain (and also zero displacement) is one of equilibrium with P_0 (i.e., $\sigma = -P_0$ for ϵ=0) and with the interface closed at the origin. In convention, a stress is related to a strain in the form $\sigma = (\lambda + 2\mu)\epsilon = \kappa \partial u/\partial x$. In this case the reference state of zero strain corresponds to zero stress. In the present case the stress-strain relation in Eq. (4.15) is used because the stress is directly associated to the dynamic interfacial force due to ultrasonic disturbance.

Inserting σ in Eq. (4.15) into Eq. (4.14) leads to the wave equation

$$\frac{\partial^2 u}{\partial t^2} = c^2 \frac{\partial^2 u}{\partial x^2} \tag{4.16}$$

where c is the propagation speed of a longitudinal wave in an unbounded space, given by

$$c = \sqrt{\frac{\kappa}{\rho}} = \sqrt{\frac{\lambda + 2\mu}{\rho}} \tag{4.17}$$

Note that the static pressure P_0 disappears in Eq. (4.16), which means that P_0 does not influence the dynamic process resulting from acoustic disturbance.

4.A.2 Characterization of rough surfaces and their contacts

An interface of two rough surfaces in contact manifests nonlinear mechanical behavior because the interface elasticity varies for compressive and tensile stresses. Such a contact rough interface is a good model for some defects in materials like kissing bonds in friction stir welds and in adhesive joints. Such defects can be detected by exploiting their nonlinear responses to ultrasound.

The ultrasonic response of a rough interface is determined by the surface properties (profiles and friction) of the two surfaces in contact. Assume that an unbounded rough interface is the

frictionless, elastic contact of two flat rough surfaces. The contact stresses depend only upon the relative profile of the two surfaces, i.e., upon the shape of the gap between the surfaces before loading. A nominal flat rough surface contains a large number of asperities whose heights vary randomly (Fig. 4.7). The heights of asperities are often characterized using Gaussian distribution [41, 42] or inverted chi-square (χ^2) distribution [41–43]. The inverted chi-square distribution is of the form

$$\phi(z) = \frac{1}{2^{n/2}\Gamma(n/2)} \left(\frac{z_{max} - z}{\sigma/\sqrt{2n}} \right)^{(n-2)/2} \exp\left(-\frac{z_{max} - z}{2\sigma/\sqrt{2n}} \right) \tag{4.18}$$

where σ is the root-mean-square (rms) roughness, and z_{max} is the maximum height of asperities. Eq. (4.18) shows that the distribution requires two parameters to define its form: the standard deviation σ and a parameter controlling its skewness, the number of degrees of freedom n. The inverted chi-square distribution is simply a chi-square distribution with a variable substitution such that it has a zero mean and is skewed toward positive heights. It is of the form

$$\phi(z) = \frac{1}{2^{n/2}\Gamma(n/2)} \left(\frac{z}{\sigma/\sqrt{2n}} \right)^{(n-2)/2} \exp\left(-\frac{z}{2\sigma/\sqrt{2n}} \right) \tag{4.19}$$

which can be obtained by substituting $z_{max} - z$ with z in Eq. (4.18).

The previous research [41] has shown that the inverted chi-distribution is better than Gaussian distribution because it fits the topography data better than the symmetric Gaussian due to the skewness parameter n, and it becomes zero when the surface heights are larger than the maximum height, as does a real surface.

When two flat rough surfaces with rms roughnesses, σ_1 and σ_2, are pressed into contact so as to form a rough interface (Fig. 4.9 (a)), the interface can be converted into an equivalent interface between a rigid smooth surface and a composite deformable rough surface (Fig. 4.9 (b)). The distribution of the composite surface heights is still characterized by the inverted chi-square distribution,

$$\phi(z) = \frac{1}{2^{n/2}\Gamma(n/2)} \left(\frac{z}{\sigma_c/\sqrt{2n}} \right)^{(n-2)/2} \exp\left(-\frac{z}{2\sigma_c/\sqrt{2n}} \right) \tag{4.20}$$

where σ_c is the composite surface rms roughness ($\sigma_c = \sqrt{\sigma_1^2 + \sigma_2^2}$). The effects of the surface properties on the interfacial mechanics can be seen below.

4.A.3 Static responses of rough interfaces - Brown-Scholz's model

When a rough interface is pressed by a hydrostatic pressure, the interface gap decreases (in other words, the relative approach increases). The relation between the external normal pressure P and the relative approach δ (Fig. 4.10) between the two contacting surfaces can be determined by Brown-Scholz's model [43]

$$P(\delta) = \frac{4}{3} M\psi \int_0^\delta (\delta - z)^{3/2} \phi(z) dz \tag{4.21}$$

where δ is the relative approach between the mean planes of the two rough surfaces, $M = \eta\langle E\rangle\langle\beta^{1/2}\rangle$, η is the summit density of the composite surface, $\langle E\rangle$ is the average reduced elastic modulus of contacting asperities, and $\langle\beta^{1/2}\rangle$ is the average of the square root of the radius of a composite peak, ψ is the factor due to the effect of misalignment. In the present case, it is assumed that $\psi = 1$.

The surfaces of a rough interface are partly in contact, and the interface gap (or the relative approach δ) is determined by external pressure P (i.e., the larger the P, the smaller the gap or the larger the δ). The interfacial force due to the contact is in equilibrium with the external pressure. $P = P(\delta)$ usually is a nonlinear function of δ (Fig. 4.11).

4.A.4 Ultrasonic (dynamic) responses of rough interfaces - ultrasonic nonlinearity

Consider a rough interface that is pressed by an external static pressure P_0 and the initial relative approach is δ_0. When an ultrasound (a dynamic force) impinges onto the interface, the gap changes. Assuming that the dynamic change of the relative approach caused by the ultrasound is $\Delta\delta$, the contact force becomes $P(\delta_0 + \Delta\delta)$.

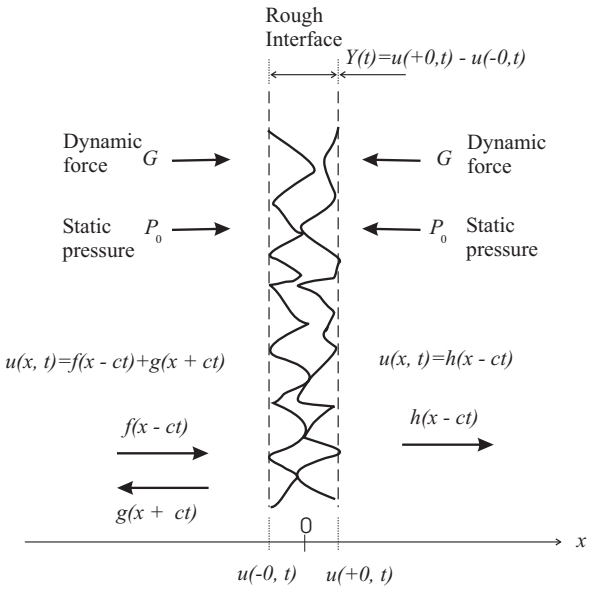

Figure 4.30: Geometry of a rough interface.

Assume that a rough interface is planar and separates two identical elastic media with Lamé elastic constants λ and μ and density ρ, and located at $x = 0$ (Fig. 4.30). When a plane wave with a particle displacement $f(x - ct)$ is incident on the interface, the corresponding ultrasonic force (the driving force *per unit area*) imposed on the interface may be expressed as

$$F(t - x/c) = -(\lambda + 2\mu)\frac{\partial f(x - ct)}{\partial x} \tag{4.22}$$

At the interface $x = 0$, the incident wave $f(x - ct)$ is partly reflected and partly transmitted. The displacement $u(x, t)$ can, thus, be expressed as

$$\begin{aligned} u(x,t) &= f(x - ct) + g(x + ct), \quad x < 0, \quad t > 0 \\ &= h(x - ct), \qquad\qquad\quad x > 0, \quad t > 0 \end{aligned} \tag{4.23}$$

where $g(x + ct)$ and $h(x - ct)$ are the reflected and transmitted waves, respectively. The stress σ can be written as

$$\begin{aligned} \sigma(x,t) = \kappa\frac{\partial u(x,t)}{\partial x} - P_0 &= \kappa[f'(x - ct) + g'(x + ct)] - P_0, \quad x < 0 \\ &= \kappa h'(x - ct) - P_0, \qquad\qquad\quad x > 0 \end{aligned} \tag{4.24}$$

At the interface the particle displacement becomes

$$\begin{aligned} u(+0,t) &= f(-ct) + g(+ct), \quad x < 0, \quad t > 0 \\ u(-0,t) &= h(-ct), \qquad\qquad\quad x > 0, \quad t > 0 \end{aligned} \tag{4.25}$$

the particle velocity is

$$\begin{aligned} \dot{u}(+0,t) &= -cf'(-ct) + cg'(ct), \quad x < 0, \quad t > 0 \\ \dot{u}(-0,t) &= -ch'(-ct), \qquad\qquad\quad x > 0, \quad t > 0 \end{aligned} \tag{4.26}$$

and the stress is

$$\begin{aligned} \sigma(+0,t) &= \kappa[f'(-ct) + g'(+ct)] - P_0, \quad x < 0 \\ \sigma(-0,t) &= \kappa h'(-ct) - P_0, \qquad\qquad\quad x > 0 \end{aligned} \tag{4.27}$$

The relative motions of interface boundaries

$$Y(t) = u(+0,t) - u(-0,t) \tag{4.28}$$

is defined as the interface opening displacement. The dynamic interfacial force (per unit area) on the contacting surfaces due to the ultrasonic displacement $u(0,t)$ is defined as

$$G = -\kappa \frac{\partial u(0,t)}{\partial x} \tag{4.29}$$

which is a function of Y.

When the interfacial gap is thin compared to the wavelength, the whole gap under ultrasonic disturbance may be assumed to have the same dynamic behavior, and thus can be modelled by a lumped system, which is a combination of distributed spring and mass [35]. This is the so-called quasi-static approximation (QSA). According to the QSA, an interfacial imperfection causes a discontinuity in the displacement that is proportional to the stress at the interface, while for interfaces between the contacting surfaces, the components of the stress fields are assumed to be continuous everywhere [43], namely,

$$\sigma(+0,t) = \sigma(-0,t) \tag{4.30}$$

From the above condition and Eq. (4.27), it follows that

$$\kappa[f'(-ct) + g'(+ct)] - P_0 = \kappa h'(-ct) - P_0 \tag{4.31}$$

which leads to the following relation (with consideration of the definition in Eq. (4.29))

$$\begin{aligned} G(Y) &= -\kappa[f'(-ct) + g'(ct)] \\ G(Y) &= -\kappa h'(-ct) \end{aligned} \tag{4.32}$$

From Eq. (4.26), and noting that $Y(t) = u(+0,t) - u(-0,t)$ and $c/\kappa = 1/(\rho c)$ (since $c^2 = \kappa/\rho$), Eq. (4.32) can be expressed as

$$\rho c \dot{Y}(t) = 2G(Y) - 2F(t) \tag{4.33}$$

which is the equation that governs the motion of interface opening displacement $Y(t)$ under ultrasonic insonification. The solution of the equation provides us the (nonlinear) response of the interface to the ultrasound. Note that $Y(t) \geq 0$ is always true, and $G(Y)$ is usually a nonlinear function of $Y(t)$.

For the initial relative approach δ_0 due to the hydrostatic pressure P_0, the initial interface gap (interface opening displacement) is assumed to be $Y(0) = Y_0$. When the interface is disturbed

by an ultrasound, it may have three states (Fig. 4.13): completely closed ($Y(t) = 0$), partially closed ($0 < Y(t) \leq Y_0 + \delta_0$), and completely open ($Y(t) > Y_0 + \delta_0$).

When the interface gap is completely closed, we have

$$Y(t) = 0; \qquad \dot{Y}(t) = 0 \tag{4.34}$$

In this case, the interface vanishes, and Eq. (4.33) gives

$$G(Y) = F(t) \tag{4.35}$$

When the interface is completely open ($Y(t) > Y_0 + \delta_0$), the stress on the interface surfaces vanish, and then we have

$$\sigma(\pm 0, t) = -G(Y) - P_0 = 0 \tag{4.36}$$

which leads to

$$G(Y) = -P_0 \tag{4.37}$$

In this case, Eq. (4.33) becomes

$$\rho c \dot{Y}(t) = -2P_0 - 2F(t) \tag{4.38}$$

When the interface is partially closed ($0 < Y(t) \leq Y_0 + \delta_0$), Eq. (4.33) can be solved if $G(Y)$ is known. If $G(Y)$ is a linear function of Y, then Eq. (4.33) may have analytical solution. However, $G(Y)$ in practice is mostly a nonlinear function of Y, thus one has to resort to numerical solution.

For a smooth interface, the gap only has two states: closed and open. It is just a special case of a rough interface without partially-closed state. Thus, Eq. (4.33) also applies to the smooth interface.

After $Y(t)$ and $u(\pm 0, t)$ are determined, and from $Y(t) = u(+0, t) - u(-0, t)$ and Eq. (4.25), the reflected wave $g(x + ct)$ and the transmitted wave $h(x - ct)$ can be found as follows

$$g(x + ct) = -\frac{1}{2} Y\left(t + \frac{x}{c}\right) \tag{4.39}$$

and

$$h(x - ct) = f(x - ct) + \frac{1}{2} Y\left(t - \frac{x}{c}\right) \tag{4.40}$$

The above two relations are useful because reflection or transmission is usually detected by a receiving transducer.

A. Ultrasonic nonlinearity of an unbounded smooth interface

Consider an incident wave of a sinusoid

$$f(x - ct) = -A \sin(kx - \omega t) \tag{4.41}$$

which at the interface $x = 0$ becomes

$$f(0 - ct) = A \sin(\omega t) \tag{4.42}$$

The driving force on the interface is (Eq. (4.22))

$$F(t) = -\kappa \frac{\partial f(x - ct)}{\partial x}|_{x=0} = \kappa k A \cos(-\omega t) = \rho c \omega A \cos(-\omega t) = B \cos(\omega t) \tag{4.43}$$

where

$$B = \rho c \omega A \tag{4.44}$$

A smooth interface may only have two states: closed ($Y(t) = 0$) and open ($Y(t) > 0$). For a closed interface, the interface opening displacement is

$$Y(t) = 0 \tag{4.45}$$

and the interfacial force is

$$G(Y) = F(t) \tag{4.46}$$

When the interface is open, one has $G(Y) = -P_0$ (Eq. (4.37)), and the governing equation of interface opening displacement (Eq. (4.38)) becomes

$$\rho c\dot{Y}(t) = -2P_0 - 2B\cos(\omega t) \tag{4.47}$$

The solution to the above differential equation is

$$\begin{aligned} Y(t) &= -\frac{2}{\rho c}\int [P_0 + B\cos(\omega t)]dt = -\frac{2}{\rho c}\left[P_0 t + \frac{B}{\omega}\sin(\omega t)\right] + C \\ &= -2A\left[\eta\omega t + \sin(\omega t)\right] + C \end{aligned} \tag{4.48}$$

where

$$\eta = P_0/B \tag{4.49}$$

and C is the arbitrary constant that can be determined from the "initial" conditions at $t = t_i$,

$$C(t_i) = Y(t_i) + 2A\left[\eta\omega t_i + \sin(\omega t_i)\right] \tag{4.50}$$

$C(t_i)$ needs to be calculated when the gap changes from the closed state to the open state, because Eq. (4.48) is valid only for the open gap. The relation of $G(Y)$ with Y is nonlinear provided that $|F(t)| > P_0$ (see Fig. 4.4).

B. Ultrasonic nonlinearity of unbounded rough interfaces

An unbounded rough interface under ultrasonic disturbance may have three states (Fig. 4.13): completely closed ($Y(t) = 0$), partially closed ($0 < Y(t) \leq Y_0 + \delta_0$), and completely open ($Y(t) > Y_0 + \delta_0$). The partially-closed state of a rough interface is the only difference from a smooth surface. The solution of Eq (4.33) for the closed and open states in the rough interface case are similar to those in the smooth interface case.

A rough interface in reality has a nonlinear stiffness (i.e., $G(Y)$ nonlinearly depends on Y in the partially closed state, $0 < Y(t) \leq Y_0 + \delta_0$) [41, 43]. Here, however, we consider a rough interface with a linear stiffness, which can be seen as a simplified case of some real rough interfaces. For such an interface, an analytical solution to Eq (4.33) is available. For the solution to a rough interface with a nonlinear stiffness one can resort to numerical calculation.

Assume that the rough interface has a linear interfacial stiffness for $0 < Y(t) < Y(0) + \delta_0$

$$G(Y) = -\kappa_0[Y(t) - Y_0] \tag{4.51}$$

where Y_0 is the initial equilibrium thickness of the interface, and κ_0 is the normal interfacial stiffness constant.

When the interface is completely closed, then

$$Y(t) = 0; \qquad G(Y) = F(t) \tag{4.52}$$

When the interface is completely open ($Y(t) > Y_0 + \delta_0$), $Y(t)$ can be determined in the same way as in the smooth interface case

$$Y(t) = -2A\left[\eta\omega t + \sin(\omega t)\right] + C_o \tag{4.53}$$

where the arbitrary constant C_o can be found from the "initial" conditions at $t = t_i$,

$$C_o(t_i) = Y(t_i) + 2A\left[\eta\omega t_i + \sin(\omega t_i)\right] \tag{4.54}$$

Note that $C_o(t_i)$ needs to be calculated when the gap changes from the partially-closed state to the open state. The interfacial force for the open gap is

$$G(Y) = -\kappa_0\delta_0 = -P_0 \tag{4.55}$$

For the partially-closed interface ($0 < Y(t) < Y_0 + \delta_0$), inserting Eq. (4.51) into Eq. (4.33) yields

$$\rho c\dot{Y}(t) = -\kappa_0[Y(t) - Y_0] - 2F(t) \tag{4.56}$$

Since the solution to equation $\dot{y} + P(t)y = Q(t)$ is $y(t) = e^{-\int P(t)dt}\left[\int Q(t)e^{intP(t)dt}dt + C\right]$, and considering $F(t) = \rho c\omega A\cos(\omega t)$, the solution to Eq. (4.56) can be found to be

$$Y(t) - Y_0 = \exp(-\xi t)\left\{-2\omega A\frac{\exp(\xi t)}{\xi^2 + \omega^2}[\xi\cos(\omega t) + \omega\sin(\omega t)] + C_p\right\} \tag{4.57}$$

where

$$\xi = \frac{2\kappa_0}{\rho c} \tag{4.58}$$

and C_p is determined by the initial value of $Y(t_j)$ at $t = t_j$,

$$C_p(t_j) = \exp(\xi t_j)\left\{[Y(t_j) - Y_0] + \frac{2\omega A}{\xi^2 + \omega^2}[\xi\cos(\omega t_j) + \omega\sin(\omega t_j)]\right\} \tag{4.59}$$

$C_p(t_j)$ should be calculated when the interface gap changes either from the open state to the partially-closed state or from the completely-closed state to the partially-closed state if the states are present. For the initial condition $Y(0) = Y_0$ at $t = 0$, one may have

$$C_p(0) = \frac{2\omega\xi A}{\xi^2 + \omega^2} \tag{4.60}$$

The interface opening displacement in this case becomes

$$Y(t) = \frac{-2\omega A}{\xi^2 + \omega^2}[\xi\cos(\omega t) + \omega\sin(\omega t)] + \exp(-\xi t)\frac{2\omega\xi A}{\xi^2 + \omega^2} + Y_0 \tag{4.61}$$

and the interfacial force is

$$G(Y) = -\kappa_0\left\{\frac{-2\omega A}{\xi^2 + \omega^2}[\xi\cos(\omega t) + \omega\sin(\omega t)] + \exp(-\xi t)\frac{2\omega\xi A}{\xi^2 + \omega^2}\right\} \tag{4.62}$$

For a rough interface with nonlinear interfacial stiffness as shown in Fig. 4.13, one can resort to the numerical computation. If an appropriate polynomial is applied to fit the nonlinear relation between $G(Y)$ and Y, the differential equation (Eq. (4.33)) can be comparatively easy to solve.

4.B Measurement results

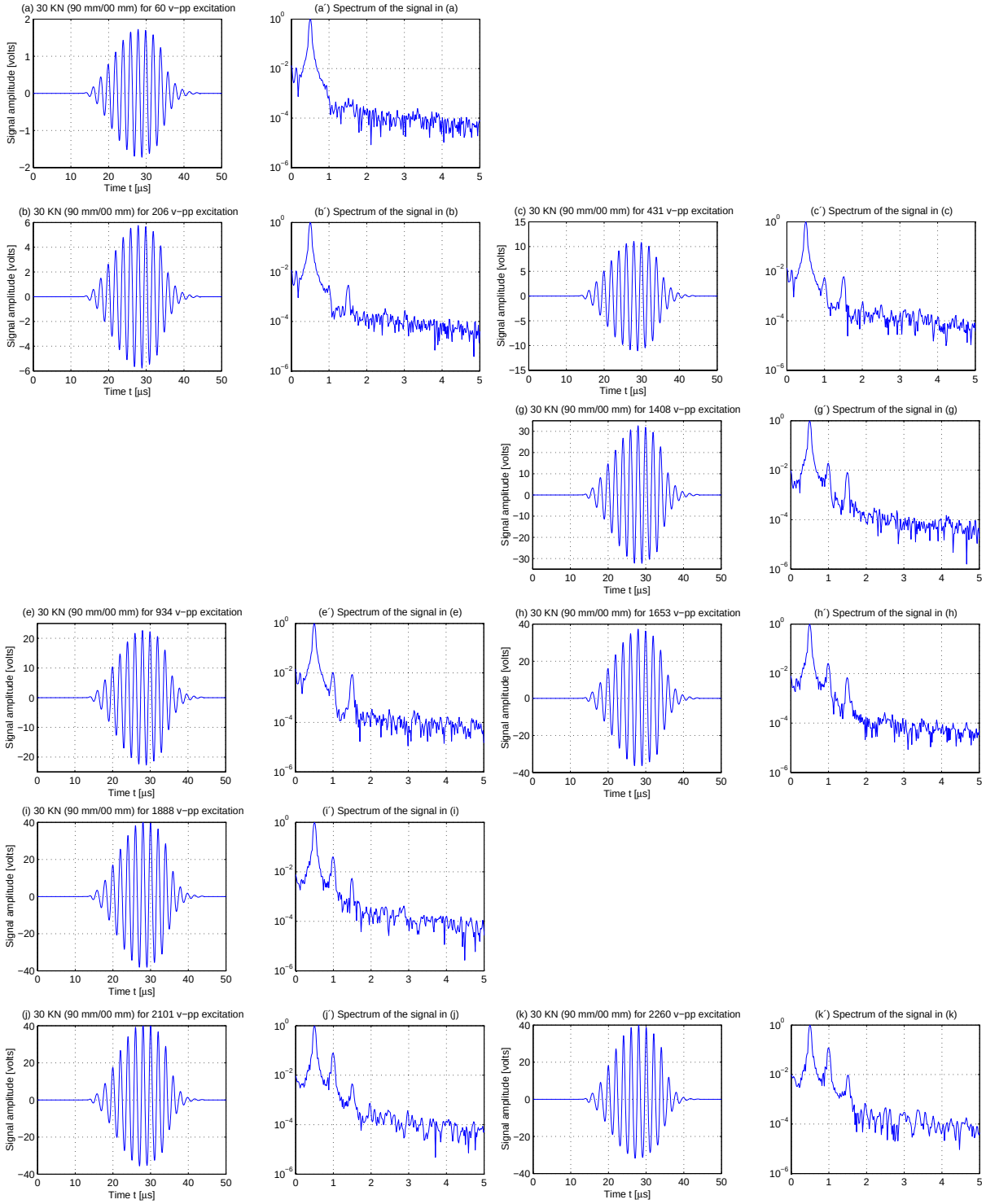

Figure 4.31: Measurements on Specimen CUCYL 0 for different tone-burst excitations E_0 and fixed external force P_0=30 KN. (a) to (k) Waveforms, and (a) to (k) their spectra.

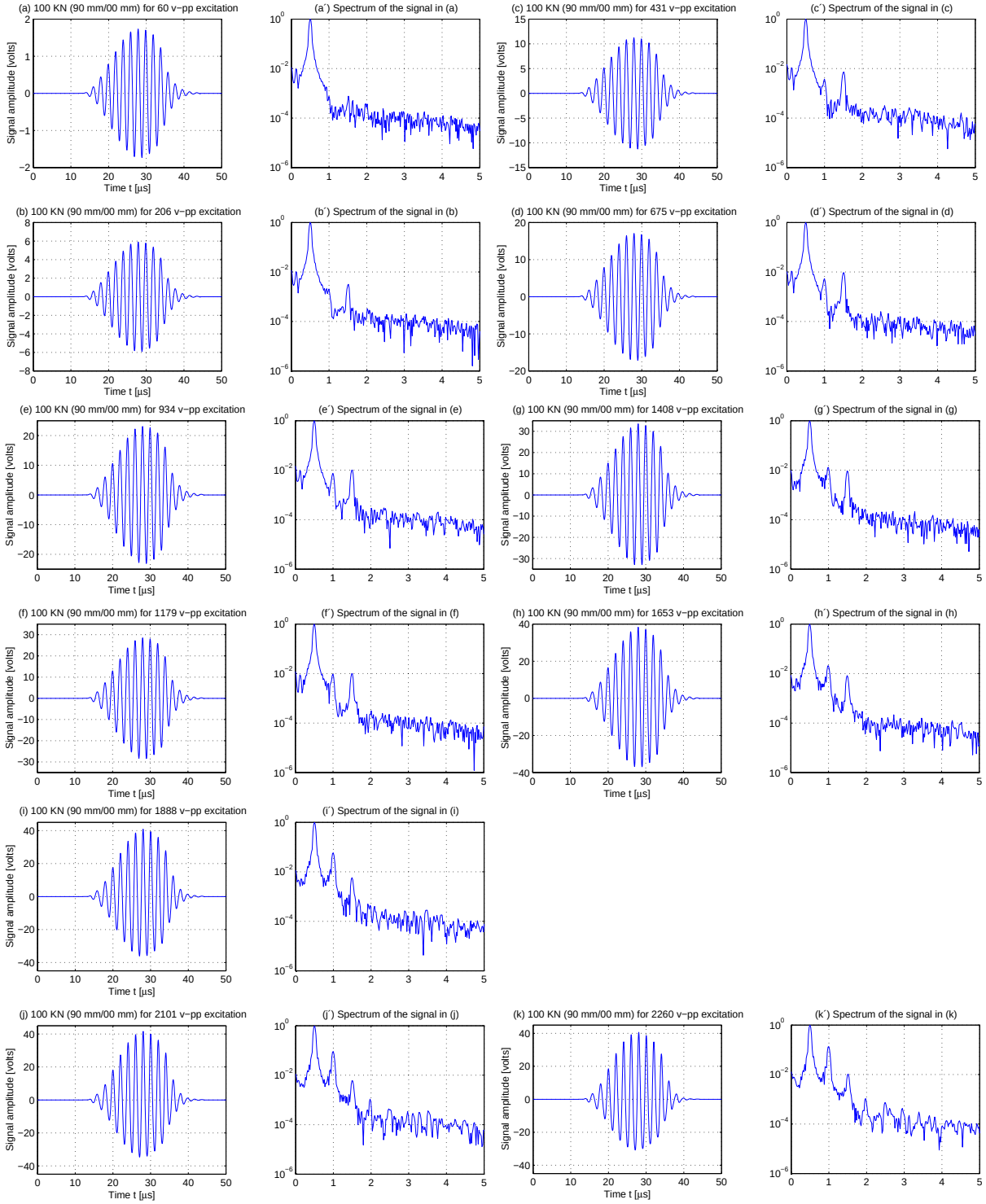

Figure 4.32: Measurements on Specimen CUCYL 0 for different tone-burst excitations E_0 and fixed external force P_0=100 KN. (a) to (k) Waveforms, and (a) to (k) their spectra.

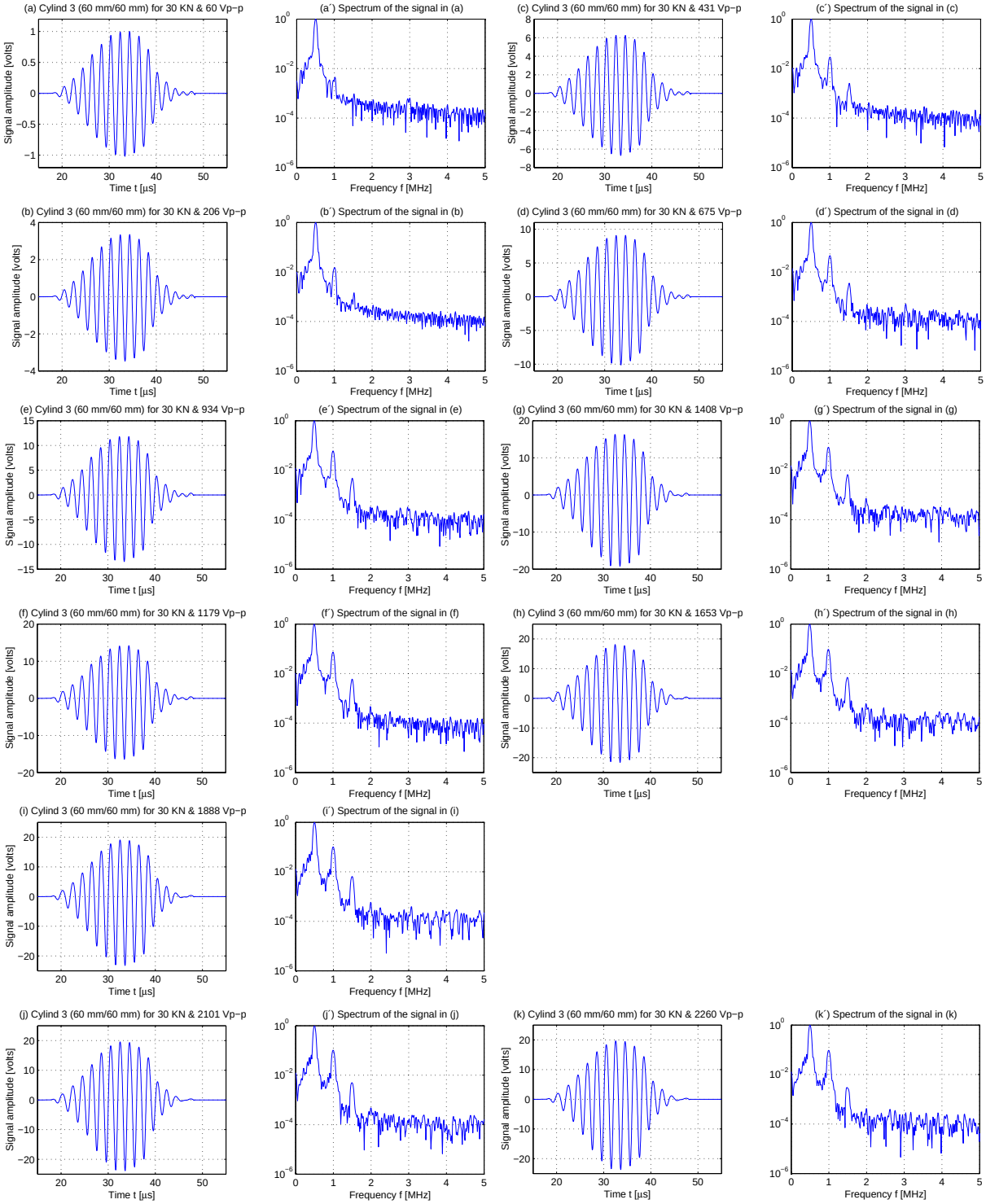

Figure 4.33: Measurements on Specimen CUCYL 3 for different tone-burst excitations E_0 and fixed external force P_0=30 KN. (a) to (k) Waveforms, and (a) to (k) their spectra.

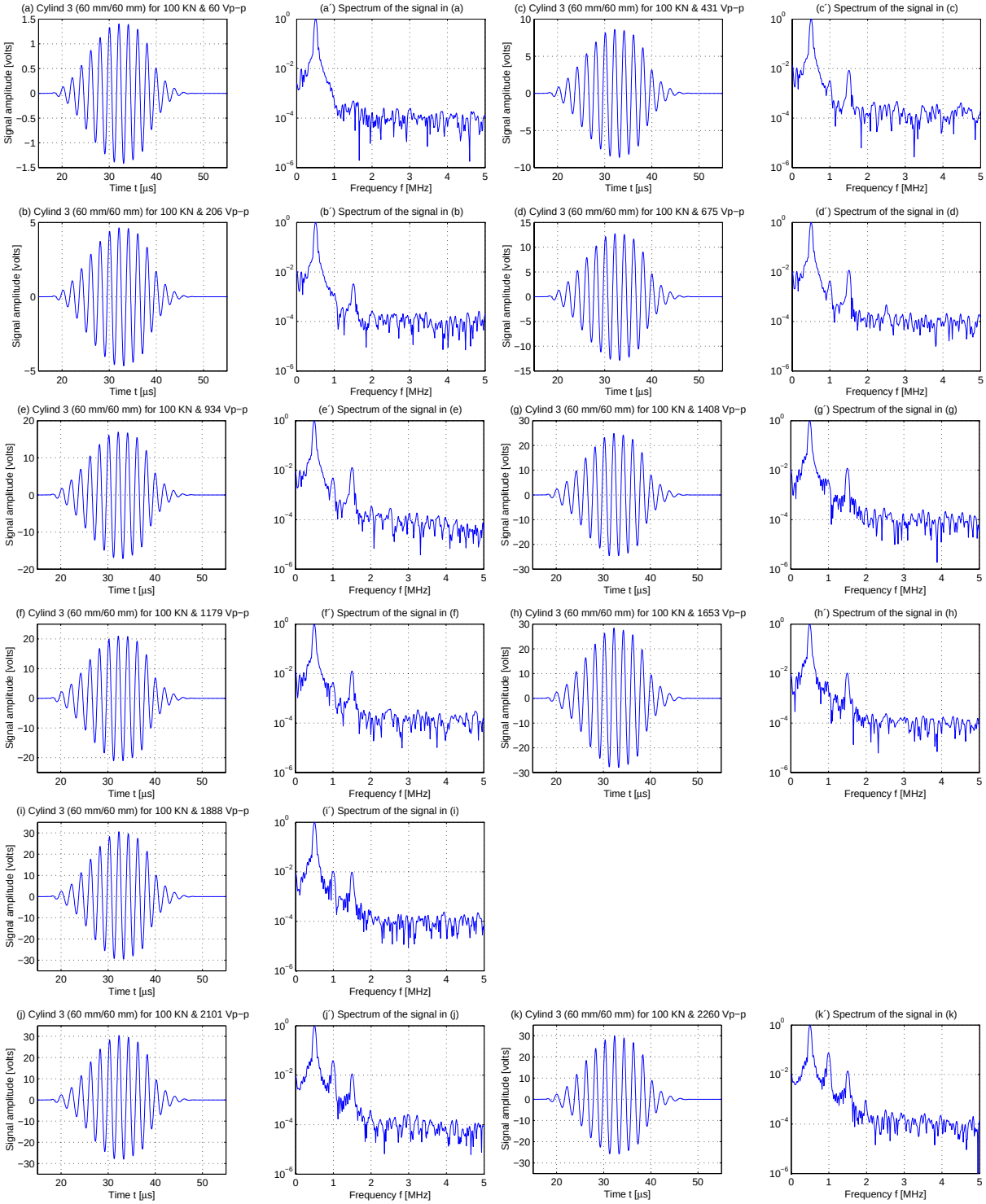

Figure 4.34: Measurements on Specimen CUCYL 3 for different tone-burst excitations E_0 and fixed external force P_0=100 KN. (a) to (k) Waveforms, and (a) to (k) their spectra.

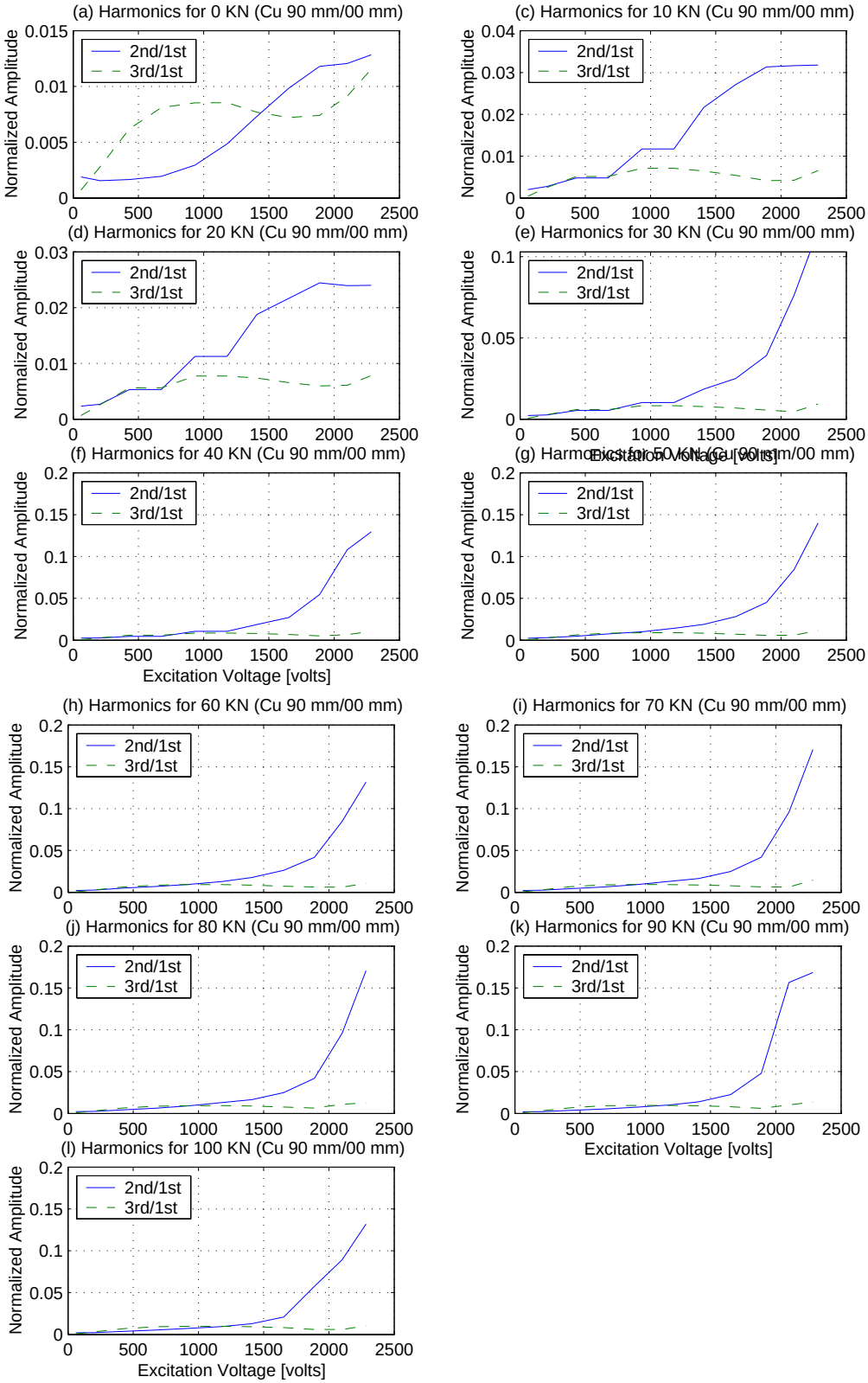

Figure 4.35: Variation of second (−) and third (- -) harmonics (normalized by the fundamental) with tone-burst excitation for external static pressures: (a) 1 KN, (c) 10 KN, (d) 20 KN, (e) 30 KN, (f) 40 KN, (g) 50 KN, (h) 60 KN, (i) 70 KN, (j) 80 KN, (k) 90 KN, (l) 100 KN.

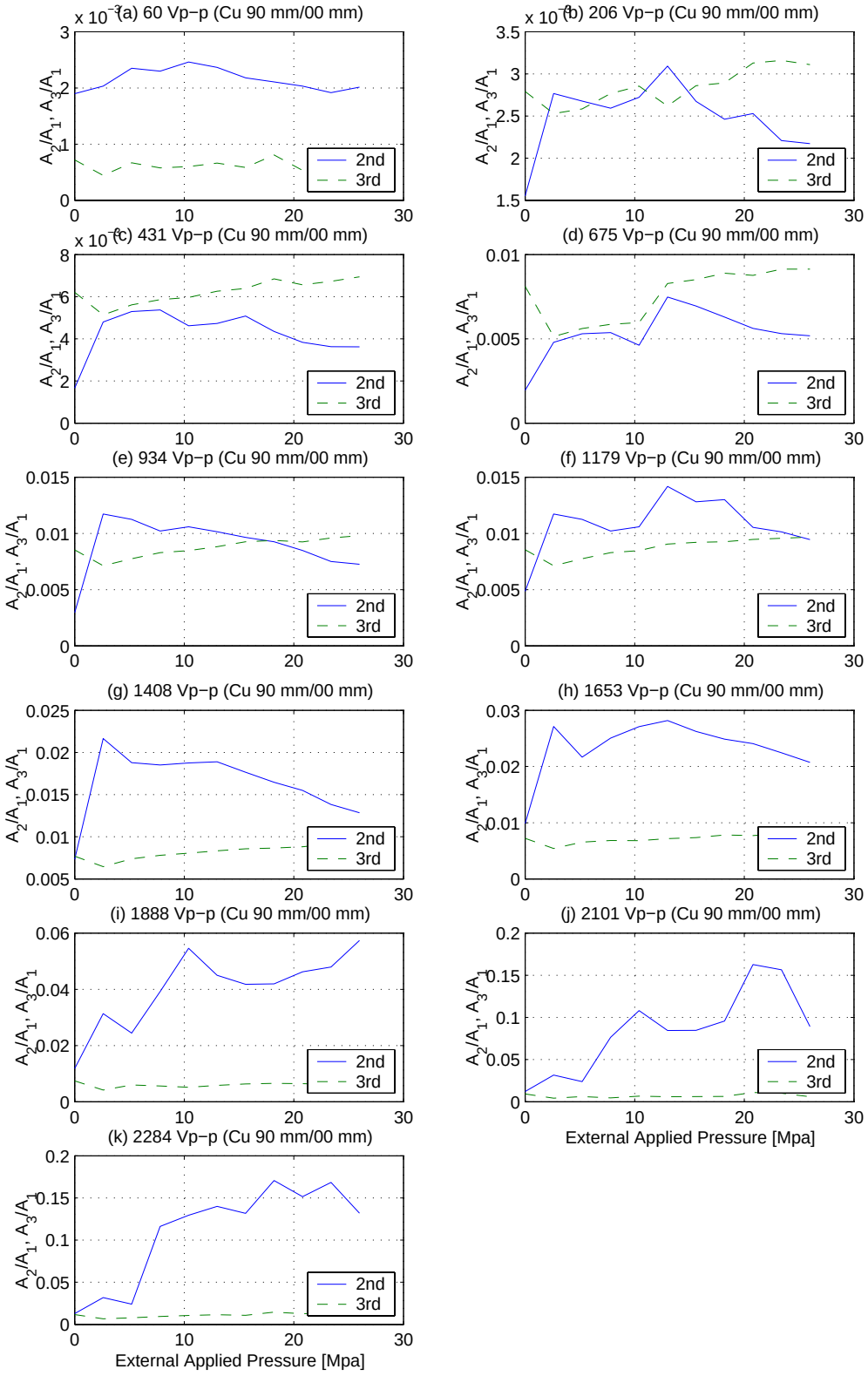

Figure 4.36: Variation of second (−) and third (- -) harmonics (normalized by the fundamental) with external static pressure for different tone-burst excitations. (a) 60 Vp-p, (b) 206 Vp-p, (c) 431 Vp-p, (d) 675 Vp-p, (e) 934 Vp-p, (f) 1179 Vp-p, (g) 1408 Vp-p, (h) 1653 Vp-p, (i) 1888 Vp-p, (j) 2101 Vp-p, and (k) 2284 Vp-p.

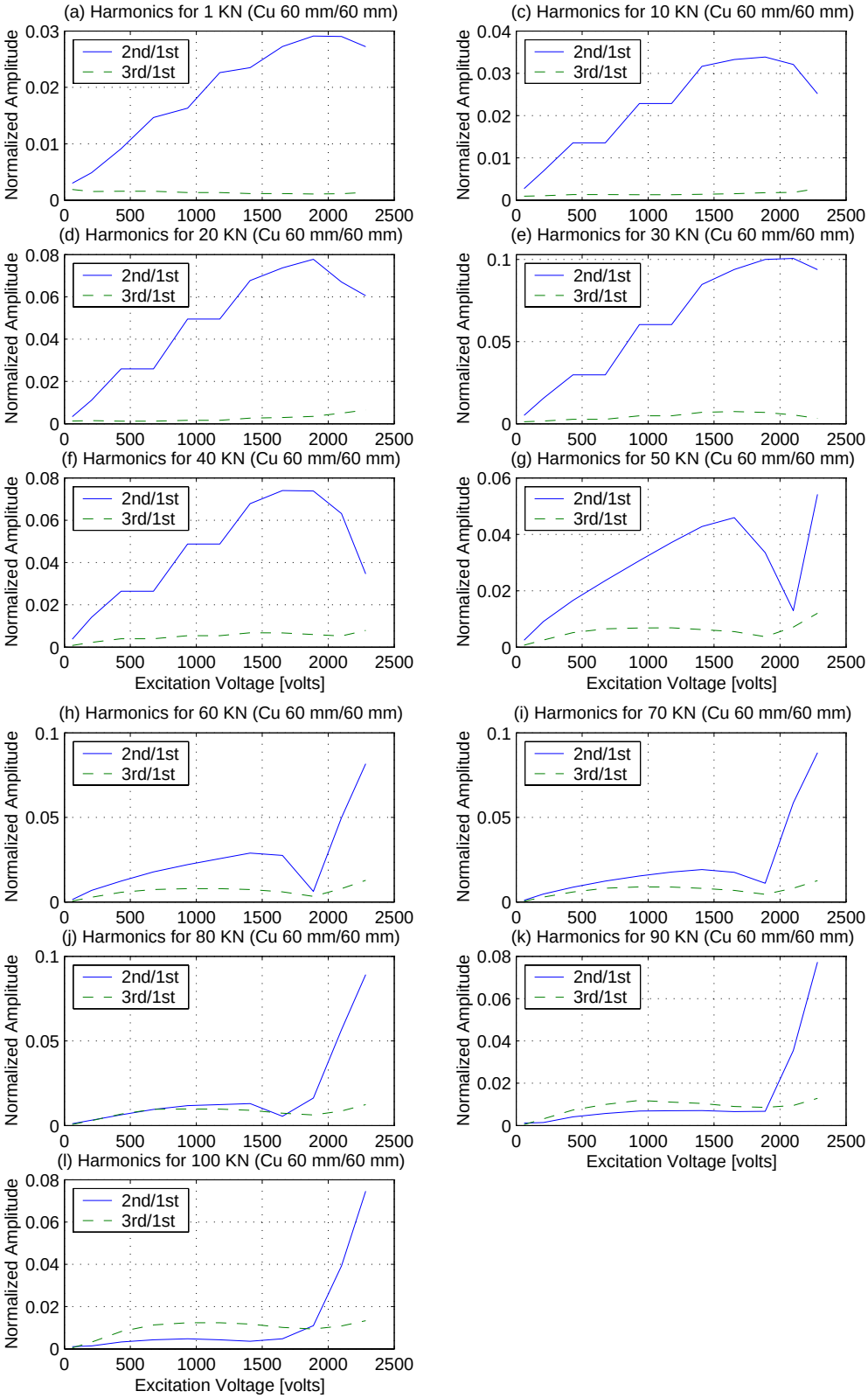

Figure 4.37: Variation of second (−) and third (- -) harmonics (normalized by the fundamental) with tone-burst excitation for external static pressures: (a) 1 KN, (c) 10 KN, (d) 20 KN, (e) 30 KN, (f) 40 KN, (g) 50 KN, (h) 60 KN, (i) 70 KN, (j) 80 KN, (k) 90 KN, (l) 100 KN.

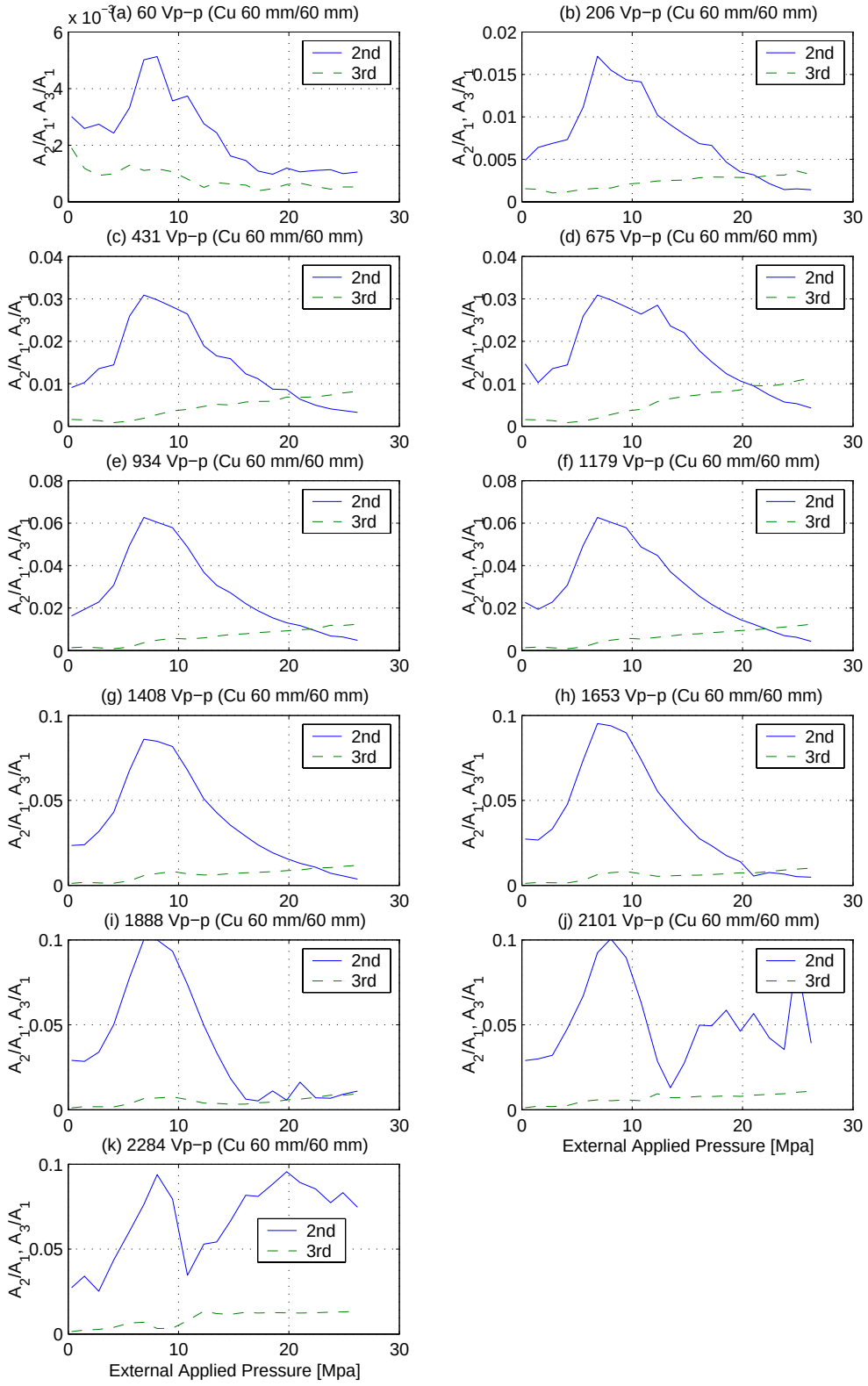

Figure 4.38: Variation of second (−) and third (- -) harmonics (normalized by the fundamental) with external static pressure for different tone-burst excitations. (a) 60 Vp-p, (b) 206 Vp-p, (c) 431 Vp-p, (d) 675 Vp-p, (e) 934 Vp-p, (f) 1179 Vp-p, (g) 1408 Vp-p, (h) 1653 Vp-p, (i) 1888 Vp-p, (j) 2101 Vp-p, and (k) 2284 Vp-p.